Diploma Thesis

On the chemical and crystalline structure of colloidal CdSe/CdS core-shell nanocrystals

Lukas Ludescher

Leoben, 02.2016

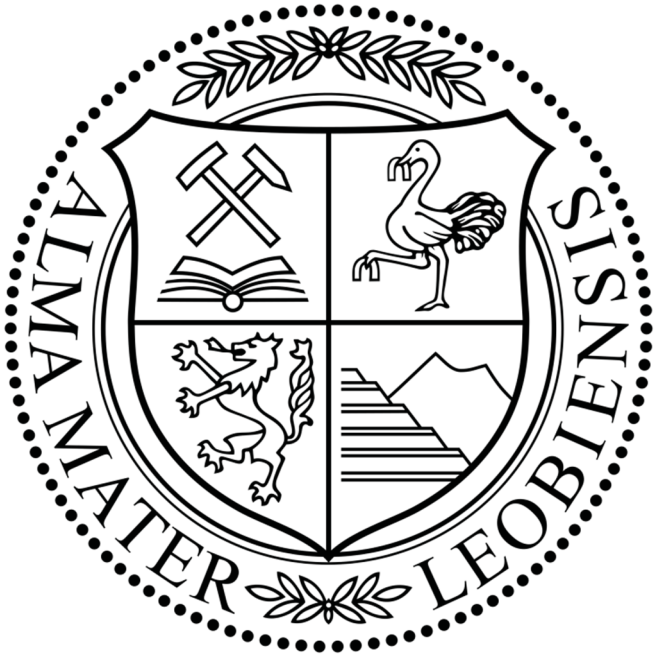

Montanuniversität Leoben

Institute of Physics

Eidesstattliche Erklärung:

Ich erkläre an Eides statt, dass ich diese Arbeit selbständig verfasst, andere als die angegebenen Quellen und Hilfsmittel nicht benutzt und mich auch sonst keiner unerlaubten Hilfsmittel bedient habe.

Affidavit:

I declare in lieu of oath, that I wrote this thesis and performed the associated research myself, using literature cited in this volume.

_____	_____
Datum	Unterschrift Kandidat

Acknowledgments

First of all, I would like to thank my family for helping and supporting me over the last half decade of my student life and beyond. A welcoming home and a full fridge are a student's dream in the hectic times of exams and/or completion of a master thesis or generally in any time of need for that matter.

I would also like to thank my supervisor Dr. Rainer Lechner for his contagious enthusiasm for science and the consequent introduction into the world of small angle and wide angle scattering as methods to probe the chemical composition and crystal structures of many exciting materials and hence further the understanding of them. Also, I need to extend a big thanks for the countless instances of discussion and bouncing of ideas to guide me through the analysis of the data collected in the very first week of my time as a master student at the ESRF in Grenoble. I can't imagine a better introduction to the nuts and bolts of the world of X-ray diffraction.

I also need to thank Dr. Oskar Paris for the guidance and patience exhibited during my time as a master student and for forgetting I fell asleep once in one of his lectures in the very front row. Luckily the reason was not the general substance of the lecture, which eventually led me to want to pursue a master thesis in the field of scattering methods, but the preceding night.

This leads me to the next round of big thanks, which I extend to my friends and girlfriend at the Montanuni Leoben. I can't recount every of the many, many times we spent having fun or the backing in times of hardship and adversary, may it have been a particularly heavy piece of furniture that we wrestled up a stairway, the loss of a loved one or simply hectic last minute cramming for an exam – Thank you.

Last but not least, I would like to thank the whole, helpful staff at the Institute of Physics and my colleagues in the bureau for the generation of a very comfortable and sometimes maybe even exhilarating environment to work in.

Abstract

CdSe/CdS core-shell nanocrystals are, at the time this thesis is being written, one of the most researched systems in the field of semiconducting nanocrystals. These kind of materials have the big advantage of highly tuneable physical properties by varying parameters such as the size of the particles or the changing the relation between radius of by core and shell-thickness.

Because these parameters are all adjusted through the synthesis of the particles, it is very important to understand the influence of the process itself on the particle resulting geometry, crystal structure and phase composition. This is why we used X-ray anomalous small angle scattering and wide angle scattering (ASAXS/WAXS) to retrieve information about these properties from samples synthesised by our partners from the ETH Zürich using a novel approach. This approach is based on the so called “hot injection” methods, in which the growth is stimulated by increased temperatures around 300°C. The particles investigated exhibit Wurtzite structure and are expected to yield higher optical performance than traditionally synthesised batches via a technique called cation exchange at lower temperatures.

The investigated samples are all taken during the “hot injection” synthesis of the shell on three different core sizes at different times, hence exhibiting different relations between core size and shell thickness. It becomes apparent that with increasing core diameter, the nanocrystals exhibit an increasingly elliptical shape. This result is retrieved from the peak width for select Bragg peaks and from the solutions via shape retrieval of the SAXS data. From the ASAXS analysis, no evidence for interdiffusion between core and shell has been extracted from the anomalous scattering data, hence a sharp interface between core and shell is implied.

In addition, we could detect an increasing amount of Zincblende crystal phase present within the core, which so far cannot be directly related to the elliptical shape. We propose a simple mechanism of martensitic phase transformation between the original Wurtzite and the Zincblende structure, which is due to condensation of planar growth faults in the particles.

All of these findings may help to explain differences in the optical performance of the particles measured by our partners at the ETH and help further design of future material systems for colloidal core-shell nanocrystals.

Kurzfassung

CdSe/CdS Kern-Schale Nanokristalle sind, zu der Zeit in der die Arbeit geschrieben wurde, eines der meistuntersuchten Materialsysteme im Bereich der Halbleiter-Nanokristalle. Diese Art von Materialien haben den großen Vorteil stark modifizierbare physikalische Eigenschaften zu besitzen, die unter anderem von der Größe der Partikel oder dem Verhältnis des Kerndurchmessers zur Schalendicke abhängen.

Da die physikalischen Eigenschaften in der Synthese eingestellt werden, ist es von besonderer Bedeutung den Einfluss des Herstellungsprozesses selbst auf die Nanokristalle bezüglich resultierender Geometrie, Kristallstruktur und Phasenzusammensetzung zu kennen. Daher haben wir anomale Klein- und Weitwinkelröntgenstreuung (ASAXS/WAXS) verwendet um Informationen über diese Eigenschaften zu erhalten. Die Proben dafür wurden an der ETH Zürich von unseren Partnern in einem neuartigen Prozess hergestellt, in dem die Nanokristalle bei erhöhter Temperatur hergestellt wurden und damit in der Wurtzitstruktur wachsen. Wegen der erhöhten Temperatur in der Synthese, fällt diese in die Klasse der „hot-injection“ – Methoden. Von den so gewonnen Kristallen wird eine bessere optische Performance erwartet, als traditionell durch Kationenaustausch bei niedrigeren Temperaturen hergestellte Teilchen.

Die untersuchten Proben wurde während unterschiedlicher Zeiten beim Schalenwachstum auf Kerne dreier unterschiedlicher Größen entnommen. Daher zeigen diese unterschiedliche Verhältnisse von Schalendicke zu Kerngröße. Aus der Analyse der Klein- und Weitwinkelstreudaten wird erkenntlich, dass mit steigender Kerngröße die Form der Nanokristalle zusehends elliptischer wird. Dieser Umstand kann auch in der Verbreiterung der Peakbreiten bestimmter Braggreflexe nachvollzogen werden. Zusätzlich kann kein Hinweis auf Interdiffusion zwischen Kern und Schale gefunden werden, was auf eine scharfe Grenzfläche zwischen Kern und Schale hindeutet.

Zusätzlich scheint mit steigender Kerngröße ein zunehmender Anteil an Zinkblendekristallstruktur in den CdSe-Kernen vorhanden zu sein, was bis jetzt noch nicht mit der größeren Elliptizität in Zusammenhang gebracht werden konnte. Zudem schlagen wir einen simplen Mechanismus für den Phasenübergang zwischen Wurtzite und Zinkblende vor, der auf der Kondensation von Stapelfehlern der Basalebene beruht.

All diese Ergebnisse können helfen die von unseren Partnern an der ETH gemessenen Unterschiede in der optischen Performance zu erklären und in Zukunft neue Materialsysteme für kolloidale Kern-Schale Nanokristalle zu designen.

Table of Content

Introduction: 1

Theory: 5

Scattering Theory: 5

General Scattering: 5

Scattering by a crystal: WAXS 7

Small Angle Scattering: 12

Anomalous Small Angle Scattering: 15

Small Angle Scattering: Modelling 18

Linear Methods: 18

Non-linear Methods 19

Experimental Section: 20

Data Analysis 24

Anomalous Small Angle X-Ray Scattering Data 24

Decomposition of the three contributions 24

Fitting of the particles 25

SAXS analysis: Dammin 33

WAXS data analysis: 34

Results and Discussion 38

Spherical evaluation: 41

Non-spherical and semi-analytical evaluation: 48

Shape retrieval by DAMMIN: 49

WAXS: 54

Summary and Outlook 67

Citations 70

Introduction:

Over the last 30 years' reliable techniques have been developed to synthesise particles with diameters of sizes of 10 nanometers and below. This happened simultaneously with the increasing use of the term "nanotechnology" in the marketing of products and subsequently in the growing scepticism of the public to this term. Aside from particles that are supposed to dampen the effects of body odour and other ailments of the modern-human condition, "nanotechnology" offers a seemingly endless array of applications in biological imaging, technology and medicine. [1]

The base of these advances are colloidal nanocrystals, which have gathered increasing interest of various scientific communities over the last decades because of their seemingly simple synthesis, ease to conduct experiments on them and the many applications which can be realised without too much investment in radically new production technologies. For instance, these kind of systems can be easily applied as a paste, a drying film etc. [1] The term "nanocrystal" (NC) itself refers to a poly- or single crystalline particle with dimensions in the range of 1 to maximum 100 nanometers. Colloidal NCs generally involve at least one outer-layer of organic molecules to guarantee solubility in a medium.

The most important reason why these kind of particles have garnered a lot of attention lately are unique properties, that can be related to the small size of the crystals. For instance, magnetic properties are heavily influenced, once one enters the nanodomain and can therefore find use in medical applications for example. [2] An example of the difference of physical properties is shown in Fig. 1 from ref. [3], where the particle size dependence of the optical properties is visible by the difference in colour.

Figure 1: The difference in emitted wavelength for the fluorescence, dependent on the size of the nanoparticles is shown for CdSe-NCs, with the diameter increasing from left to right. Ref. [3]

The particles investigated in this work are colloidal Cadmiumselenide (CdSe)/ Cadmiumsulfide (CdS) core-shell nanocrystals, meaning that these particles are constituted of a CdSe core on which a protective

CdS shell has been grown on. As shown by Ref [4] on PbS/CdS core-shell NCs, the crystal structure and thickness of the shell in relation to the core influence the optical performance and stability of these particles. This also implies the possibility of engineering these particles to fit ones needs within certain limits.

In the aforementioned reference [4] a dependence of the physical properties of the particles and the crystalline and geometric constitution of the particle has been explored. The particles investigated in this study were synthesised via cation exchange, which simply describes the growth of the shell by exchange of a certain element in the unit cell of the crystal. This process is also diffusion controlled, which leads to a shell, in which the exchange has already been performed, and an unaltered core.

As a consequence, it would be of interest to study whether a:

a) different synthesis route and
b) different system

would exhibit the same characteristics. The synthesis of choice was a so called “hot injection” method, which supposedly leads to CdSe/CdS particles in Wurtzite structure, that yield higher performance and stability than chemically identical, yet structurally different particles [5]. The “hot injection” method gets its name from the simple fact, that the synthesis is performed at relatively elevated temperatures of ca. 300°C. But the significant difference between this method and cation exchange is the epitaxial growth of the shell on the core, thus being in contrast to a shell that grows via phase change of the outer regions of an already existing core.

To gain understanding, experimental techniques such as Transmission Electron Microscopy (TEM), x-ray diffraction (XRD) and photoluminescence (PL) are usually applied [5]. These unfortunately have severe limitations, as TEM images only show a few particles and reveal a two dimensional projection of a crystal, which doesn’t allow definitive conclusions on the shape, size or polydispersity with its limited sample size. There is the possibility of TEM-tomography [6], but this technique also doesn’t allow for the determination of structure of a statistically significant number of particles in a reasonable amount of time. In addition, the experimental requirements in preparation are more laborious for TEM when compared to small angle scattering (SAS) in the case of colloidal nanocrystals. XRD in return seems to allow a more or less reliable and statistical accurate extraction of the mean crystalite size, through the Scherrers formula, but information on the shape is very hard to retrieve, even via refinement methods [7]. There have been some developments in shape retrieval methods [7], but these still heavily rely on previous information from other sources, such as the aforementioned experimentally expensive TEM. Other extensions to x-ray techniques try for the determination of the macro- and microstrain present in crystalline samples in addition to the mean size. The effect of different stacking faults and/or point defects however complicates the picture. As a consequence, detailed analysis of nanocrystals

proves to be still quite challenging, which sparked a lot of progress in this field in the last few years regarding such techniques as Rietveld analysis and Whole Powder Pattern Modelling [7].

The only experimental technique that probes the geometry of NCs with acceptable effort and required precision is small angle scattering (SAS), which reveals the mean geometric properties, such as size, shape and polydispersity, of samples. In the light of application of these particles, this is actually of much use, as only large numbers of nanocrystals will be used at once in many microelectronic and macroscopic optical devices. As the typically irradiated volume of the sample contains approximately 10^{10} particles, the data gained through this method is therefore of high statistical value. This circumstance has led to the acceptance of this technique in the determination of protein structures and sparked the development of program packages by various groups to retrieve parameters of interest such as the shape, polydispersity and possible agglomeration of colloidal NCs. Regarding compositional information, it's extraction relies heavily on assumptions on the system, as all the chemical information is inferred via the contrast. Evaluation is consequently "guesswork", where model dependent analysis is modified to fit previous knowledge with techniques like regularisation and other penalizing functionals. These approaches naturally may deliver useful data for very well-known systems, but potentially influence results of yet unexplored samples negatively.

Consequently, one can rightfully claim that to gain full understanding of the particles synthesised by a specific process, all of the techniques mentioned above only represent necessary, but not complete, pieces of a puzzle to be solved. Even x-rayflouresence based techniques, such as energy dispersive electron microscopy, don't allow atomic resolution of the chemical composition of nanometre sized particles. To retrieve such information, the variance of the scattering factor of an element with the energy of an incident x-ray beam can be used to retrieve spatial information about the species constituting the NCs under investigation. In the case of small angle scattering this technique is called anomalous small angle x-ray scattering (ASAXS) and simply varies the contrast of a designated phase with x-rays of differing, yet precisely tuned energies. Unfortunately, laboratory sources don't allow for continuously varying x-ray energies, thus only synchrotron sources can be used for this technique [8]. But even in the case of these great machines, only the technical advances of the last few decades and the resulting third generation of synchrotrons allow to reliably extract information in such a way. In the case of neutron diffraction, variation of contrast has been possible for quite some time now, as for instance the contrast can be varied to a higher degree via, for example, deuterated water or lithium. Unfortunately for us, certain elements, such as the, in our particles present, Cadmium are excellent absorbers of neutrons and consequently make successful investigation with neutrons of samples containing this element hard to conduct.

Thus, we conducted ASAXS experiments on the CdSe/CdS core-shell NCs in combination with wide angle x-ray scattering (WAXS) to retrieve not only the NCs geometry and spatial distribution of Selenium within the particles, but also the crystal structure of particles grown by the so-called "hot

injection" method. This builds on the aforementioned study performed by R.T. Lechner [4], who conducted his investigations on core-shell particles synthesised by ion exchange. Hence we hope to understand whether his results concerning optical properties in dependence of thickness and of phase fractions within the shell are replicable, or if this system behaves differently. Ultimately, recommendations on the optimal geometric configuration should be given to maximise optical performance.

Theory:

Scattering Theory:

The first few of the following paragraphs will only be concerned with the elastic scattering of x-rays, while the latter paragraphs will specifically treat anomalous scattering.

X-rays are photons or classically transverse electromagnetic waves with a wavelength in the range of 10^{-10} m, allowing for probing structures within the same size range. The basic principle of generation of these waves can be described through Maxwell's equations and basically breaks down to the emission of photons by accelerated charges. Synchotron radiation sources work by that exact principle, whereby electrons are guided to travel within a storage ring [8]. Once an x-ray beam hits matter, it can react elastically and inelastically. [9] As mentioned above we for now only care about elastic interaction of particles, known as elastic scattering. For the sake of scientific accuracy, the wave length used in the experiments conducted in this work is around 1 Angström at an energy of roughly $2 \cdot 10^{-15}$ Joule, which means that the scattering present actually falls within a grey area between the Mie regime and regular scattering. But because the results apparently don't differ much when using general scattering to describe the phenomena of small angle (x-ray) scattering in systems such as the one investigated here, we will stick to general scattering.

General Scattering:

When an electromagnetic wave interacts with matter of any kind it can be absorbed, scattered or just passed through. Elastic scattering is defined as an interaction in which the total energy of the incident and exiting beam are equal, while inelastic scattering usually is linked to loss of some part of the entering beams energy, may it be through excitation of an electron onto a different orbit or through the Compton-effect. [8]

An incident plane wave with the angular frequency w and propagation vector $\boldsymbol{k}$ is defined as

$$E_{in}(\boldsymbol{r}, t) = E_0 e^{-i(\boldsymbol{k}\cdot\boldsymbol{r} - wt)} \quad \textbf{(1)}$$

The intensity of a beam is correlated to the square of its electric field, thus to the signal measured, or "scattering cross section". Alternatively, from the detectors point of view, the measured intensity is equal to the number of recorded scattered photons is I_{sc} over a detection angle $\Delta\Omega$, with an incoming flux of ϕ_o. This gives:

$$\frac{\mathrm{d}\sigma}{\mathrm{d}\Omega} = \frac{I_{\mathrm{sc}}}{\phi_o * \Delta\Omega} = \frac{|\mathrm{E_{rad}}|^2 R^2}{|\mathrm{E_{in}}|^2} \quad \textbf{(2)}$$

If we would want to calculate the scattering by a single, free electron, the formula above would read

$$\frac{d\sigma}{d\Omega} = {r_0}^2 \cdot \cos^2(\psi) \tag{3}$$

where ψ is the angle between the direction of propagation and the observation point. This equation is important, because it shows that a free electron doesn't have a scattering length that is dependent on the energy of the incident wave. r_0, called the Thomson scattering length and purely dependent on natural constants, reads as

$$r_0 = \frac{e^2}{4\pi\epsilon_0 mc^2} \sim 2.82 \cdot 10^{-5} \text{Å} \tag{4}$$

A real beam, directed on a sample, is not a mathematically sharp line, as it probes a finite volume of material at once. It is thus advantageous to define an electron number-density $\rho(r)$, which interacts like a mass of free electrons in most models used to describe scattering. To further simplify our treatment, we neglect the interaction of the scattered waves with the electromagnetic field generated by the interaction itself, which is called the Born approximation. [10]

If we now direct a monochromatic, polarized beam on a crystal not the entirety of it will interact and some of it will pass through. In this work, we are only interested in the scattered beams, which interacted elastically with the electron gas surrounding the atoms of the probed crystal. These rays have the same energy and Euclidian magnitude of momentum as the incident beam. We now consider two points at a distance *r*, at which a scattering event occurs, in Fig. 2:

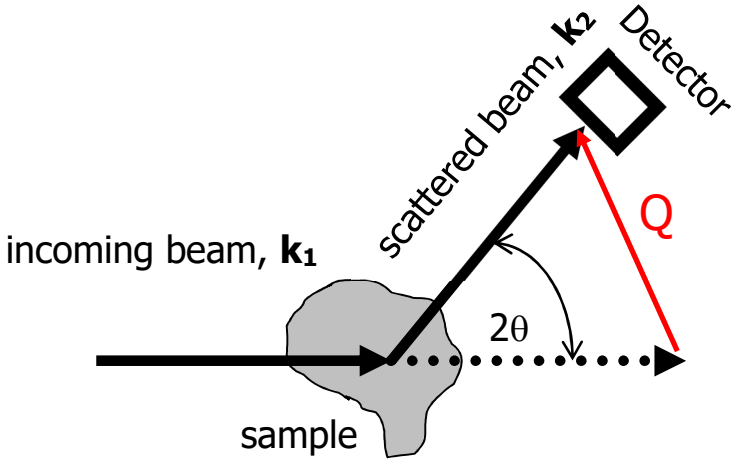

Figure 2: The incidence vector is denoted with $\mathbf{k_1}$*, the scattered vector with* $\mathbf{k_2}$*. Owing to elastic scattering, they both have the same magnitude* $2\pi/\lambda$*. (Graphic with courtesy from Oskar Paris)*

The difference in phase Δ of these two rays with the incident momentum $\boldsymbol{k_1}$ and the scattered momentum $\boldsymbol{k_2}$ now is:

$$\Delta(\mathbf{r}) = (\boldsymbol{k_2} - \boldsymbol{k_1}) \cdot \boldsymbol{r} = \boldsymbol{Q} \cdot \boldsymbol{r} \quad \textbf{(5)}$$

The vector $\boldsymbol{Q}$ is called the scattering vector or vector of momentum transfer. As a scalar quantity, with λ being the wavelength of the incident and diffracted beams and Φ representing the half of the scattering angle, it equates to:

$$\mathrm{Q} = \frac{4\pi \sin(\Phi)}{\lambda} \quad \textbf{(6)}$$

An assembly of electrons, represented by a number density $\rho(\boldsymbol{r})$, creates the following amplitude of elastic scattering

$$A(Q) = \int \mathrm{dr}\, \rho(r) \exp(-i\, \boldsymbol{Q} \cdot \boldsymbol{r}) \quad \textbf{(7)}$$

As the electron is essentially delocalized in an ideally spherical volume around the atom, a dependence of the electron number density on $\boldsymbol{r}$ is necessary for a more complete description. Of interest is the fact that we actually need to use the $\Delta\, \rho(\boldsymbol{r})$. This needs to be done as we can only identify differences in contrast. In the case of X-ray diffraction this is the electron density of the scatterer to the overall mean density, and not the total density [11].

As already noted earlier, the intensity of a wave is equal to its amplitude squared. If we assume a symmetric, homogenous distribution of electrons around a nucleus, the intensity can be expressed as

$$I(Q) = A(Q) * \overline{A(Q)} = \text{bs}(\Delta\rho \int \mathbf{dr} \exp(-i\, \boldsymbol{Q} \cdot \boldsymbol{r})) \quad \textbf{(8)}$$

Scattering by a crystal: XRD

As Photons are scattered by the electrons surrounding the atoms of a crystal, we essentially probe the electron density $\rho(\boldsymbol{r})$ of the crystal. To correctly calculate the scattering intensity, we first need to consider the scattering by a single atom $\boldsymbol{i}$ and thus write *equation 7* again as:

$$f_i = \int \mathrm{dV}\, \rho_i(\boldsymbol{r}) \exp(-\mathrm{i}\, \mathbf{Q} \cdot \boldsymbol{r}) \quad \textbf{(9)}$$

We simply integrate over the volume of the electron density of an atom under investigation. The argument of the exponential can be rewritten with a basic property of dot products between two vectors:

$$\boldsymbol{Q} \cdot \boldsymbol{r} = Qr \cos(\alpha) \quad \textbf{(10)}$$

This leads to a simplified expression called the form factor of an atom if we assume a spherical volume in which the electron is present, which is closely related to the form factors acquired for SAS. The dot product above allows us to integrate over all possible incident angles of the directional vector $\boldsymbol{r}$ and the scattered vector $\boldsymbol{Q}$, if we put part of the integrational variable to $d(\cos(\alpha))$ and integrate from -1 to 1. This evaluates to:

$$f_i = \int_0^\infty \mathrm{dr}\, 4\pi\ \rho(\boldsymbol{r})\, r^2 \frac{\sin(\boldsymbol{Q}\cdot\boldsymbol{r})}{\boldsymbol{Q}\cdot\boldsymbol{r}} \qquad \textbf{(11)}$$

This essentially represents a Fourier transform of the electron density; the square is proportional to the scattered intensity from an atom $\boldsymbol{i}$.

A perfect crystal can be represented very simply by a stacking of identical and therefore interchangeable unit cells. Each of these unit cells then can be described by the position of objects within this cell and the nature of these objects. In crystallography the position is described by a so called Bravais lattice and the objects on the positions are called the basis of a crystal. If we now imagine a crystal and put atoms as a basis on the Bravais-lattice of the crystal, we simply need to sum over the projections r of all atom positions within a cell on the scattering vector of a crystal plane of our choosing to calculate the interference of the scattering of a whole crystal cell! Written down as a formula this reads:

$$S_{Q(h,k,l)} = \sum_j f_j \exp(-i\ \boldsymbol{Q}\cdot\boldsymbol{r}) \quad \left[= \sum_j f_j \exp(-i\ \boldsymbol{G}\cdot\boldsymbol{r_{hkl}})\right] \qquad \textbf{(12)}$$

S is a quantity called the structure factor of a lattice; f represents the atomic form factor derived above in *eq. 11*. *Equation 12* is completely general, but for the case of a crystal $\boldsymbol{Q}$ coincides with the reciprocal lattice vector $\boldsymbol{G}$ and $\boldsymbol{r}$ with a lattice vector $\boldsymbol{r_{hkl}}$. Hence, plugging in the vectors $\boldsymbol{G}$ and $\boldsymbol{r_{hkl}}$ of a crystal, the structure factor basically determines which reflexes are visible [8] at which angle and represents the scattering amplitude. Therefore, it's square is proportional to the scattering intensity at a certain value of Q. Now, as the position of the atoms within the unit cell are hidden in the structure factor within the vector $\boldsymbol{r}$, a change in the lattice spacing results in a visible shift of the peaks in a recorded spectrum as the exponential still needs to be proportional to 2π to guarantee positive interference of a scattered coherent wave. This can be achieved by introducing strain to a crystal, for the sake of simplicity we assume macroscopic strain, which yields:

$$\epsilon = \frac{\Delta \mathrm{d}}{d} = \frac{d - d_0}{d_0} = \frac{d}{d_0} - 1 = \frac{q_0}{q} - 1 \qquad \textbf{(13)}$$

with $q = 2\pi/d$. Therefore, the nature of the strain, meaning compressive or tensile, can be seen by the direction of the shift with its sign being reverse to the sign of $\Delta q(= q_0 - q)$. Hence an increase in the lattice spacing implicates a tensile strain, which is given a positive sign by convention, where as in reciprocal space this leads to a shift to the left and hence to a negative sign. By evaluating multiple peaks and introducing models of the strained unit cell, which relates the spacing of the atoms to the state of stress, one can even calculate the whole stress tensor using this simple idea.

So far, we have only considered perfect crystals, with infinite dimensions, meaning we would get perfect, delta-function like peaks if we were to conduct a scattering experiment on a crystal. But if we reduce the amount of planes that contribute to the reflection by limiting the size of the crystal, the peak broadens. This fact can be calculated for example for a small parallelopipedon crystal [12]:

$$I = I_e S^2 \frac{\sin(N_1 \boldsymbol{Q} \cdot \boldsymbol{a_1})^2}{\sin(\boldsymbol{Q} \cdot \boldsymbol{a_1})^2} \frac{\sin(N_2 \boldsymbol{Q} \cdot \boldsymbol{a_2})^2}{\sin(\boldsymbol{Q} \cdot \boldsymbol{a_2})^2} \frac{\sin(N_3 \boldsymbol{Q} \cdot \boldsymbol{a_3})^2}{\sin(\boldsymbol{Q} \cdot \boldsymbol{a_3})^2} \quad \textbf{(14)}$$

This equation, with the vectors of the crystal a_i and total number of cells N_i in the indexed direction, can be used to arrive at Scherrer's equation. This equation is used to estimate the crystal diameter *d* by analysis of diffraction peaks [12]:

$$B(2\theta) = \frac{K\,\lambda}{d \cdot \cos(\theta)}; B(\boldsymbol{Q}) = \frac{2\pi\,K}{d} \quad \textbf{(15)}$$

Here we use the second version, as all of our data was already translated into *Q* and the integral breadth *B,* or alternatively FWHM, were calculated through peak fitting. If one chooses to evaluate the FWHM, the value auf the constant *K* changes, but the quality of the overall solution does not. The FWHM is more widely used, because it's evaluation was simpler in the earlier times of X-ray diffraction in contrast to the integral breadth *B.* [12] Even though this equation was derived under the assumption of cubic crystals, it has some use for the estimation of non-cubic crystals, such as one of the systems under investigation in this treatise: Wurtzite.

An increase in breadth of a peak can also be caused, for instance, by:

- macroscopic strain
- microstrain
- dislocations
- stacking faults
- instrumental broadening

To gain information on the crystal size and the type and magnitude of the strain, we must first eliminate the instrumental contribution to the peak. In general, the measured profile is a convolution of the

instrumental function $g(x)$ and the samples peak function $f(x)$, which results in the measured curve $h(x)$. [12] As this can be done both in the q and the 2θ regime, x can be substituted accordingly.

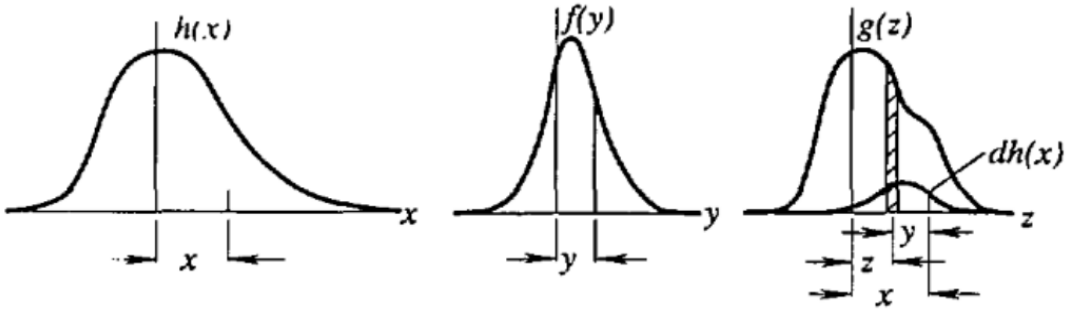

Figure 3: A fictive pattern and its composition is displayed. On the left the measured function, which represent a convolution of the middle and right functions, representing the actual profile and the instrumental peak. [12]

There are some general ways to separate the two contributions to the peak shape, such as the Stokes deconvolution, which essentially represents all the functions in their complex Fourier-series form. This results in a trivially solvable integral, in which the Fourier coefficients F_n and G_n are constant and finally yield

$$h(x) = \int g(z)f(x-z)\mathrm{dz} \rightarrow h(x) = \sum_n G_n F_n \left(\frac{-2\pi \sin(x)}{a}\right) \quad \textbf{(16)}$$

which leads to

$$F_n = \frac{H_n}{G_n} \quad \textbf{(17)}$$

Consequently, the unaltered profile can be obtained upon back transformation [12]. A different and more popular way to clean up the recorded pattern works via integral breadth methods. [13] The advantage of these methods is the ease of implementation and evaluation, its major drawback is the fact, that assumptions about the peak form heavily influence the results obtained and may give misleading results. [7] Still, these methods are a quick and qualitatively sound way for a first glance on data. To get rid of the instrumental contribution it is assumed that the broadening due to the instrument is of the same kind and represents a convolution of two Gaussians or Lorentzians or a combination of both [13], respectively, one representing the instrumental and one the crystal function. Therefore, fits of both and the widths or breadths therein are used. The breadths/widths of the measured instrumental and physical profile under the assumption of a Gaussian shape convolute to

$$\beta^2{}_{\mathrm{hG}} = \beta^2{}_{\mathrm{gG}} + \beta^2{}_{\mathrm{fG}} \quad \textbf{(18)}$$

With β_{hG} representing the measured, β_{gG} the instrumental and β_{fG} the specimens peak functions. In the case of Lorentzians this results in a simple addition of the two contributions

$$\beta_{hL} = \beta_{gL} + \beta_{fL} \tag{19}$$

To measure the instrumental contribution, it is necessary to record a standardized sample with no broadening due to the specimen used. Popular choices of such samples are zirconia and *para bromo benzoic acid* (PBBA). It is therefore possible to further analyse the pattern with the method of the Williamson-Hall-Plot [14]. This method falls within a family of methods with the same general idea behind them:

$$\Delta \mathrm{q} \propto \frac{1}{D} + f(q) \tag{20}$$

Usually one assumes that the integral breadth increases or decreases linearly and monotonous with q, in which case $\Delta \mathrm{q}$ can be fit with a simple linear regression. This simply yields a line, whose intersection at $q = 0$ represents the breadth used to calculate the crystal size and whose slope equals the isotropic strain in the crystal. If the integral breadths don't follow this monotonously growing trend, an anisotropy in shape or various other effects such as faulting, twinning or plastic deformation are implicated [14]. Warren has shown for various crystal structures that the broadening follows certain arithmetic rules concerning the hkl of the reflections [12]. For hcp crystals like our CdSe/CdS particles in Wurtzite structure the following equation applies for stacking faults of the basal plane:

$$-\left(\frac{\mathrm{d}\square}{\mathrm{dL}}\right) = \frac{1}{D} + \frac{|l|d}{c^2}(h-k)(3\alpha + \beta\, 3^{\left|1-\sin\left(\frac{\pi}{2}l\right)\right|}) \tag{21}$$

A represents the cosine Fourier Coefficient of a peak, L a virtual distance within the crystal perpendicular to the plane investigated, d the lattice spacing, c the spacing of the 00l plane, α the faulting probability of deformation faults and β the likelihood of planar stacking faults, the Miller indices correspond to the peak under investigation. If *h* equals *k* and/or *l* has a value of zero, no broadening should be seen, but if the first 2 indices of a plane differ and *l* is even, the broadening due to stacking faults increases threefold in comparison to *l* being odd. [12] There has been a lot of progress made in this field, with differentiation between intrinsic, extrinsic, condensed extrinsic stacking faults, pyramidal and non-pyramidal twinning etc. To keep a long story short, extrinsic stacking faults in hcp materials don't broaden peaks with $h \neq k$ and *l* being even [12]. Additionally, extrinsic stacking faults actually recover the Zincblende structure in Wurtzite materials via a sort of martensitic transformation and can possibly be realised through two intrinsic, or also called growth, faults with one plane in between. [15]

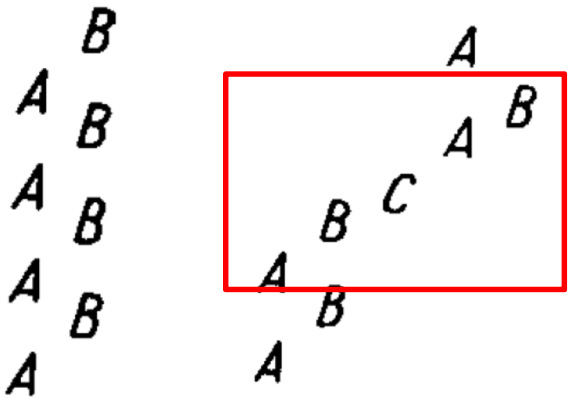

Figure 4: Stacking of the typical hcp lattice is shown on the left, an example of extrinsic faulting on the right. The highlighted region corresponds to a Zincblende cell. [12]

Small Angle Scattering:

If we consider the interference function for any object, may it be crystalline or amorphous, there exists a term, that does not depend on the internal structure of the sample itself [18]. This term only depends on the shape and size of the particle under investigation. If we define the angular width as

$$\Delta = \frac{\lambda}{d} \tag{22}$$

with d being the diameter of the particle and λ being the wavelength of the X-ray beam used to probe a sample. If we now assume a wavelength of ca. 0.1 nm and an angular width of ca 10^{-2} nm^{-1}, the diameter of the particle investigated needs to be 0.1 µm or less to record a useful scattering pattern. With our particles exhibiting a diameter of ca. 10 nm, we easily fall within the small angle scattering regime. As stated above, the derivation of the atomic scattering factor is pretty similar to the form factors in SAS in mathematical structure. We simply conduct a Fourier transform of an object with an electron density $\rho(r)$, and follow exactly the same route as before, but normalised to the volume of our particle. Translated to the picture used here:

$$F(Q) = \frac{1}{V_p}\int_0^\infty \mathrm{dr}\, 4\pi\, \Delta\rho(\boldsymbol{r})\, r^2 \frac{\sin(\boldsymbol{Q}\cdot\boldsymbol{r})}{\boldsymbol{Q}\cdot\boldsymbol{r}} \tag{23}$$

Thus, if we set the electron density constant, we arrive at the spherical form factor:

$$F_{\mathrm{Sphere}}(Q) = 3\,\Delta\rho\,\frac{\sin(Qr) - Qr\cos(Qr)}{(Qr)^3} = 3\,\Delta\rho\,\frac{j_1(Qr)}{Qr} \tag{24}$$

j_1 represents a Spherical Bessel function of the first kind, which we will later use to derive a form factor for an ellipsoid of revolution. One also could think of systems with more than one phase und consequently contrast. One example of such systems are called core-shell systems, as investigated in this work, and can for instance be generalized as a series of layered geometries [16]:

$$F_{n-1\ \text{shells}} = \frac{\rho_1\, V_1\, F_1(Q, R_1) + \sum_{i=2}^{n} (\rho_i - \rho_{i-1})\, V_i\, F_1(Q, R_i)}{\rho_1\, V_1 + \sum_{i=2}^{n} V_i\, (\rho_i - \rho_{i-1})} \tag{25}$$

The denominator above is necessary to normalize the form factor to one, as Q approaches 0. This simply represents the transmitted intensity of the sample. [16]

The total intensity is proportional to the square of the form factor, but also the number of particles *N*, the particle volume squared and a structure factor *S* [9].

$$I(Q) = \mathrm{N\ S(Q)\ \Delta\rho^2\ |F(Q)|^2\ {V_p}^2} \tag{26}$$

This factor should not be confused with the structure factor of a crystal, but it represents a quality of similar fashion, as it describes structural effects between the particles itself on the total intensity I. Glatter introduced an alternative way to calculate the intensity, the so called "Pair-Distance-Distribution-Function", such that [11]

$$I(Q) = 4\pi \int_0^{\infty} p(r) \frac{\sin(Qr)}{Qr} \mathrm{dr} \tag{27}$$

with

$$p(r) = \widetilde{\Delta\rho}(r)^2\, r^2 = \int \Delta\rho_1\, \Delta\, \rho(r_1 - r)\, \mathrm{dr}_1\, r^2 \tag{28}$$

This basically represents the autocorrelation function of the electron density of a geometric body, which means that the $p(r)$ is directly related to the structure and size of a particle.

Yet a different and more general way, as it is not only limited to SAS, is the calculation of the intensity by Debye's equation [11]:

$$\mathrm{I}(Q) = \frac{1}{{N_v}^2} \sum_{i=0}^{N_v} \sum_{i \neq j}^{N_v} F_j F_i\, \frac{\sin(Qr_{ij})}{Qr_{ij}} \tag{29}$$

Here r represents the distance between two scatterers, N_v the total amount of scattering bodies. The derivation of this formula works just as described above in *eq. 27*.For instance following the example of two atoms at a distance Abs(r_{1-2}) from each other and plugging this into said equation [8]:

$$\text{[illegible]}(Q) = f_1 + f_2 \exp(-i\, Q\, r_{1-2}) \tag{30}$$

Thus one can write

$$< I(Q) >=< \text{[illegible]}(Q)^2 >= {f_1}^2 + {f_2}^2 + 2\, f_1 f_2\ < \exp(i\, Q\, r_{1-2}) > \tag{31}$$

With the same idea as stated above with the atomic form factor, we can average over the exponential, normalize to 1 and consequently arrive at Debye's formula above.

If we choose to polynomially expand the cardinal sinus and assume equivalent form factors for any particle in *eq. 29*, one gets [17]:

$$\begin{aligned}\frac{\mathrm{I}(Q)}{F^2} = 1 - \frac{1}{3}\left(\frac{1}{2{N_v}^2}\sum_{i=0}^{N_v}\sum_{i\neq j}^{N_v} {r_{\mathrm{ij}}}^2\right)Q^2 + \frac{1}{60}\left(\frac{1}{2{N_v}^2}\sum_{i=0}^{N_v}\sum_{i\neq j}^{N_v} {r_{\mathrm{ij}}}^4\right)Q^4 \\ + \frac{1}{2520}\left(\frac{1}{2{N_v}^2}\sum_{i=0}^{N_v}\sum_{i\neq j}^{N_v} {r_{\mathrm{ij}}}^6\right)Q^6 + O(Q^8)\end{aligned} \tag{32}$$

As has been shown if ref [17], the equation above can be transformed into an integral by the definition of the Riemann integral. This yields the following three formulas:

$$\Delta \mathrm{r}_2 = \frac{1}{2{N_v}^2}\sum_{i=0}^{N_v}\sum_{i\neq j}^{N_v} {r_{\mathrm{ij}}}^2 = \frac{1}{V_p}\int_{V_p} r^2 \mathrm{dV} \tag{33}$$

$$\Delta \mathrm{r}_4 = \frac{1}{2{N_v}^2}\sum_{i=0}^{N_v}\sum_{i\neq j}^{N_v} {r_{\mathrm{ij}}}^4 = \frac{1}{{V_p}^2}(V_p \int_{V_p} r^4 \mathrm{dV} + (\int_{V_p} r^2 \mathrm{dV})^2 + 2\int_{V_p}\int_{V_p} (r_i\, r_j)^2 \mathrm{dV}_i \mathrm{dV}_j) \tag{34}$$

$$\begin{aligned}\Delta \mathrm{r}_6 = \frac{1}{2{N_v}^2}\sum_{i=0}^{N_v}\sum_{i\neq j}^{N_v} {r_{\mathrm{ij}}}^6 \\ = \frac{1}{{V_p}^2}(V_p \int_{V_p} r^6 \mathrm{dV} + 3\int_{V_p} r^4 \mathrm{dV} \int_{V_p} r^2 \mathrm{dV} + 12\int_{V_p}\int_{V_p} {r_i}^2\, (r_i\, r_j)^2 \mathrm{dV}_i \mathrm{dV}_j)\end{aligned} \tag{35}$$

These represent the second, fourth and sixth moment of our shape. *Equation 33* is commonly referred to as the squared radius of gyration and gives an indication about the particle size. Two particles with the same radius of gyration don't necessarily have the same shape. This is where the fourth and sixth moments come in to play, as these represent the aspect ratios or "peakedness". [17]

If we plug in different shapes, we can derive formulas for simple bodies like cuboids and spheroids and can fit these to the first few points of a recorded pattern. [17] This allows us to roughly estimate not only the size, but also the general dimensions and aspect ratios of a particle and use this information for further evaluations. This process is not easily implementable for core-shell particles, thus only the cores can generally be evaluated this way.

The above analysis only works well for monodisperse systems. Considering this fact, it is possible to model polydisperse samples under the assumption of a monomodal distribution of the core sizes [11]:

$$< F(Q,R)^2 >= \frac{1}{N} \int_0^\infty F(Q,r)^2 \, \omega(r,p) \, {V_{\mathrm{part}}}^2 \, \mathrm{dr} \tag{36}$$

with

$$N = \int_0^\infty \omega(r,p) \, {V_{\mathrm{part}}}^2 \, \mathrm{dr} \tag{37}$$

$w(r,p)$ represents a particle size distribution with the parameter vector p of a distribution. But the numerical integration, if an analytical solution does not exist, can be cumbersome and use up many resources when performing a fit. It is easier to simply "create" different species with radii scattered around a mean and weigh them accordingly to the distribution $w(r,p)$ to correctly calculate the intensity.

A more complete treatise of SAS can be found in [11] or [18].

Anomalous Small Angle X-Ray Scattering:

The expression of the atomic form factor in *eq. 7* doesn't deliver a complete picture of the physics behind it. Let's imagine a bound electron spinning around a nucleus, like in a classical, planetary-like description of atoms, in an alternating electrical field with a restoring force similar to a spring equation. The resulting equation of motion effectively describes a damped, forced oscillation with an amplitude of [19]:

$$a_0 = \frac{\frac{E_0 e}{m}}{({\omega_0}^2 - \omega^2 + j\frac{g^2\omega^2}{m^2})} \tag{38}$$

The amplitude of the electric field is E_0, e represents the electron charge, m the mass, g the damping due to the velocity and the spring constant k is as always hidden in ${\omega_0}^2 = k/m$. When the frequency of the acceleration, tuned by the energy of the x-rays, exhibits a certain value, the amplitude reaches its maximum. In the simplified picture of a nucleus surrounded by electrons on circular orbits, the electron switches onto a different orbit and part of the incident x-ray beams energy is diminished. The atomic form factor for an element thus varies with the energy of the beam used to probe the material and even shows absorption like features, which can ultimately be expressed as a relative factor [20]:

$$\Delta f_z = \Delta f_{oZ} + f_i' + j f_i" \tag{39}$$

The energy dependence of f_i' and $f_i"$ on close to an absorption edge for the element Selenium is depicted in Fig. 5:

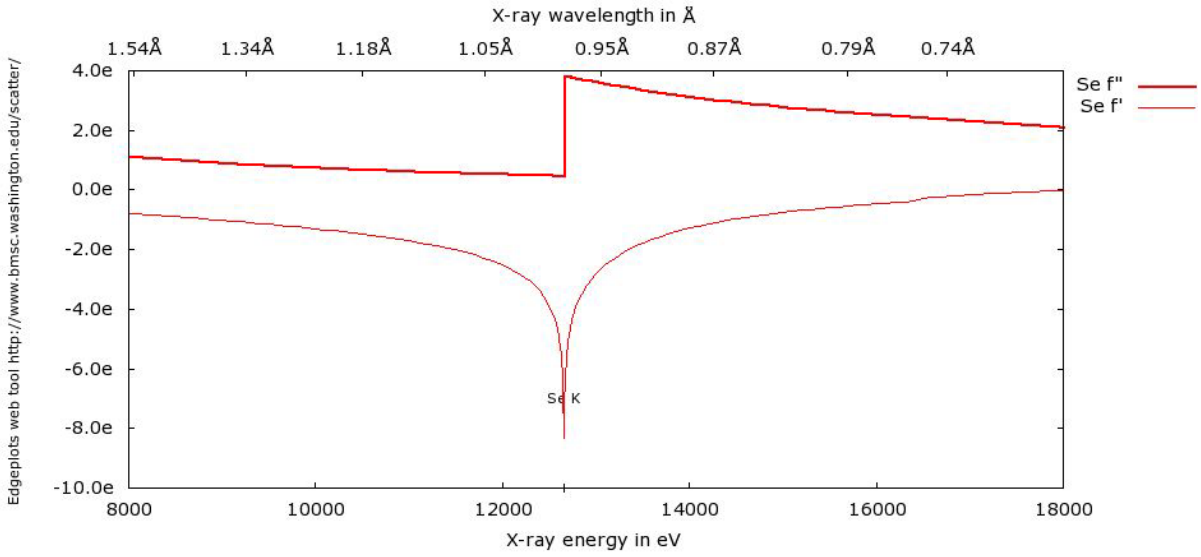

Figure 5: Both parts of the complex scattering factor of Selenium are plotted versus the x-ray energy within the region of the edge used in this thesis to vary the scattered intensity. A clear discontinuity is discernible for both parts, f' and f''.

Equation 39 can be related to the form factor of a given geometric configuration according to [21]:

$$F(Q,E) = F_o(Q) + \big(f'(E) + j\, f"(E)\big)\nu(Q) \tag{40}$$

The intensity follows with:

$$I(Q) = F_o(Q)^2 + 2f'(E)'F_o(G)\,\nu(Q) + \Big(\big(f'(E)\big)^2 + (f"(E))^2\Big)\nu(Q)^2 \tag{41}$$

The first term of the sum equals the scattering of the whole shape as we previously calculated, but the second and third term contain the spatial distribution $\nu(Q)$ of the element whose scattering factor we

vary! The second term is accordingly called the cross term, but most of the information is contained in the unfortunately relatively small third, also called resonant, term.

Through varying energies, at which a scattering pattern is recorded, one can use the resulting variations in contrast to determine the spatial distribution of an element in a multispecies crystal. Because the effect is very small, it is necessary to increase the contrast as much as possible, which means to measure energies near and also above the absorption edge. Concerning the energies above the adsorption edge, experimentally the fluorescence has to be taken into account, but the step-like increase of the f'' allows for greater contrast between spectra and consequently easier evaluation. [21] From *eq. 41* it can be readily seen, that with a minimum of three energies a matrix equation can be formulated:

$$\begin{pmatrix} I(E_1,Q) \\ I(E_2,Q) \\ I(E_3,Q) \end{pmatrix} = \begin{pmatrix} {\Delta f_0}^2 & 2\,\Delta f_0\, f(E_1)' & [(f(E_1)')^2 + (f(E_1)'')^2] \\ {\Delta f_0}^2 & 2\,\Delta f_0\, f(E_2)' & [(f(E_2)')^2 + (f(E_2)'')^2] \\ {\Delta f_0}^2 & 2\,\Delta f_0\, f(E_3)' & [(f(E_3)')^2 + (f(E_3)'')^2] \end{pmatrix} \begin{pmatrix} F_o(Q)^2 \\ F_o(Q)\,\nu(Q) \\ \nu(Q)^2 \end{pmatrix} \qquad \textbf{(42)}$$

As the solution vector is already known from the measurement and the entries in the matrix are known beforehand, *eq. 42* poses an inverse problem. This class of problems is one of the most important, as it allows to determine parameters that are not directly measurable. *Equation 42* can be solved for $\nu(Q)^2$ in several ways, ranging from Gaussian to Eigenvalue decomposition, but according to [21, 22] with increasing number of energies evaluated the absolute error in matrix inversions grows. This means, that the crucial factor is the quality of the singular measurement and not the number of curves recorded. It is therefore also possible to measure at a different edge to gain additional, meaningful equations without compromising the quality of the matrix inversion.

This is of utmost importance as all fitting algorithms, should one decide to use this method of evaluation, involve at least one matrix inversion. Thus, the reliability of the data is potentially negatively affected and the resulting data tainted with non-negligible errors. A first upper estimate of the error made with one inversion can be made using Turing's number, as can be seen in [22]. Turing's number actually represents a conditioning number of a matrix, which relates the error of the input with the error of the output. Therefore, this concept can also be used to calculate the minimum value of flux necessary for a given illumination time or vice versa, to arrive at a ratio of error of measurement to total intensity $\Delta I/_I$ that renders the resulting equation "well-conditioned". For the sake of brevity, we won't go into more detail at this point [22].

Small Angle Scattering: Modelling

When modelling data, one usually tries to achieve minimal discrepancy between the model and the measurement. This usually involves minimizing a least squares problem, although more robust measurements of deviation can be chosen. Still, most program packages use some variant of the reduced chi-squared:

$$\chi^2 = \frac{1}{n-f}\sum_{i=1}^{n}\frac{(I_{\exp}(Q_i) - I_{\mathrm{mod}}(Q_i))^2}{{\sigma_i}^2} \quad \textbf{(43)}$$

with n being the number of points measured and f being the number of fit parameters to be minimized. This has the obvious advantage, that deviations at high values are weighted somewhat the same as lower values. When the discrepancy comes out to be around the total average measured error σ, this equates to 1 and represents a "perfect" fit and represents statistical agreement between the fitted model and the measured data [16]. This is unfortunately no always the physically meaningful solution to the problem at hand, even though the system itself may be well conditioned.

Linear Methods:

If the resulting equation is purely linear in its coefficients, standard least squares methods can be employed [16]. Any function that can be written as

$$\mathrm{I}(Q)_{\mathrm{mod}} = \sum_{i=1}^{k}\alpha_k\,\mathrm{X}(Q)_k \quad \textbf{(44)}$$

is essentially a linear expression, where $X(Q)_k$ represents a set of basis-functions [11]. As a consequence, it can be easily solved by the standard methods in a timely manner.

The great achievement of the indirect Fourier transformation (IFT), which calculates the pair correlation function $p(r)$ of a SAS curve by spline interpolation using equation [11], is the linearization through the coefficients of the interpolating functions.

$$I_{\mathrm{mod}}(Q) = \sum_{k=1}^{m}\alpha_k \cdot X_k(Q) = 4\pi\int p(r)\frac{\sin(Qr)}{Qr}\mathrm{dr} \quad \textbf{(45)}$$

Where

$$p(r) = \sum_{k=1}^{m}\alpha_k\,B_k(r) \quad \textbf{(46)}$$

This also allows for a simple, linear Tikhonov regularization resulting in the functional [11,16]:

$$\mathrm{Min}(\chi^2 + \lambda[\sum_{j=1}^{m-1}(\alpha_{j+1} - \alpha_j)^2 + {\alpha_1}^2 + {\alpha_m}^2]) \quad \textbf{(47)}$$

with the additional term being a measure for smoothness, weighed by the regularization parameter λ . This is similar to the method employed by Svergun [23] in his program *GNOME*, which is part of package *ATSAS,*to which we will refer later.

Non-linear Methods

If the model function is of the nonlinear kind, different methods have to be used to solve for the parameters of the given function. In this case for instance Levenberg-Marquardt[25], Reduced Gradient[26], Nelder Mead [27] or Simulated Annealing [27] can be employed. Even the above mentioned Tikhonov regularisation can be used in this case too [28], if the function to be minimized represents an ill-conditioned problem [29]:

$$\mathrm{Min}(\chi(Q,p)^2 + \lambda^2 L(p)^2) \quad \textbf{(48)}$$

Differently than before, the optimal value for the parameter λ needs to be recalculated every single iteration, using different paths such as the discrepancy or L-curve criterion [51]. This needs to be done, because with decreasing χ^2 the regularizing, second term contributes more and more and might "oversmooth" the solution. To use this method confidently the algorithms above have to be modified, as was done with the Levenberg-Marquardt algorithm in Ref [30].

Also in the realm of non-linear methods is the shape retrieval software *DAMMIN* [31] used in this work. Here a Simulated-Annealing algorithm is being used to iterate to the final shape of the desired particle. More information on the general concept of this approach and evaluation techniques can be found in [32].

Experimental Section:

As mentioned in the introduction, knowledge about the synthesis process of colloidal NCs and the ability to tune the properties of the systems to the field of application is essential for optimal performance. To investigate the structural and physical implications of our system CdSe-CdS, the following three series of nanoparticles have been prepared at the ETH by Maksym Kovalenko's group.

On three batches of differing CdSe core sizes with diameters of 1.8 nm, 2.2nm and 2.5 nm, 4, 6 and 8 monolayers of CdS have been epitaxially grown on in a wet chemical synthesis. [5] The CdSe cores were synthesized via the following procedure: Mixing of CdO, octadecylphosphonic acid (ODPA) and trioctylphosphine oxide (TOPO) and subsequent degassing for one hour after heating up to 150°C. Afterwards the temperature was elevated up to 320°C to form a colourless solution, upon which trioctylphosphine (TOP) was injected. Again the temperature was increased until it reached 380°C, at which point Se/TOP solution was swiftly injected. This induced the growth of CdSe-cores, a temperature driven process, meaning that the growth can be stopped, after for instance reaching a desired size, by rapid cooling. The resulting CdSe particles were then precipitated by adding acetone and dispersed in hexane as a stock solustion. [5]

On these particles the CdS shell was grown by loading the hexane solution containing the naocrystals in a mixture of 1-octadecene (ODE) and oleylamine (OAm). The reaction solution was degassed afterwards at room temperature under vacuum for one hour and subsequently for 20 minutes at 120°C. The solution was again heated up to 310°C with a heating rate of ~ 20°C/min und nitrogen flow and magnetic stirring. Upon reaching 240°C while heating a desired amount of shell-forming cadmium (II) oleate and octanethiol was injected dropwise at ca. 3 ml/hr via a syringe pump. After the desired amount was injected oleic acid was quickly introduced to stop shell growth and the solution was further annealed at 310°C for an hour. [5] Aliquots were extracted at times that should ideally correspond to the above mentioned shell thicknesses of around 4, 6 and 8 monolayers of CdS under the assumption that some amount, which so far is only known to our partner, of the total of the injected precursors have formed shells. This synthesis was carried through to produce particles in Wurtzite structure, which have demonstrated superior quantum yield over similar systems of differing crystal structure. [5] The resulting particles were all diluted in toluene, since other solvents, such as hexane or chloroform, are too poisonous to handle in a in-situ set up to measure the samples.

With 3 aliquots taken at different times before annealing for all three core sizes, we are left with three series potentially giving insight on the processes through synthesis. These series consist of one core of yet undetermined size, three core-shell systems with increasing shell thickness and one annealed batch of core-shell particles for a total of 15 samples. An overview of the samples synthesised and the names used from this point is listed in table [1]:

Table [1]: Listing of all the abbreviations used for the samples measured:

	core	thinnest shell	medium shell	largest shell	annealed
smallest core	sc	st	sm	sl	sa
medium core	mc	mt	mm	ml	ma
largest core	lc	lt	lm	ll	la

The ASAXS and WAXS experiments on these samples were all carried out at the ESRF at beamline ID02 under the guidance of the local contact Michael Sztucki and Peter Boesecke. ID02 is one of few beamlines equipped to measure ASAXS and WAXS simultaneously. The element whose contrast was varied was Selenium (Se), which should theoretically only be found in the core of our particles. The absorption edge used was at 12.658 keV and seven energies at or below and three above this value were chosen to take measurements at. This results in a total of 10 energies summed up in table [2], of which the ones above the edge additionally had to be corrected for the occurring fluorescence. To reduce radiation damage to our sample, the dissolved nanocrystals were continuously pushed through a flow-cell by a piezoelectric system. [20] Also an empty and a water-filled capillary were measured for all energies.

Table 2: scattering factors and the corresponding energies used in the experiment

Energy [keV]	**f'**	**f''**
12.000	-2.5163	0.5511
12.580	-4.5789	0.5177
12.612	-5.1239	0.5263
12.644	-6.4534	0.59504
12.650	-7.1094	0.6839
12.653	-7.6897	0.8356
12.655	-8.3271	1.1864
12.657	-8.964	2.6264
12.676	-6.002	3.7693
12.732	-4.5132	3.781

The ASAXS and WAXS spectra were recorded at once by two different, stacked 2D detectors (Fig. 6) and the resulting data were integrated and corrected. These corrections included not only standard operations like correction for dark current, flat field, normalisation to absolute scattering units and Ewald sphere projections, but also accounted for various effects like fluorescence above the absorption edge,

transmission correction, background etc., and were performed on site online using a provided script by Michael Sztucki.

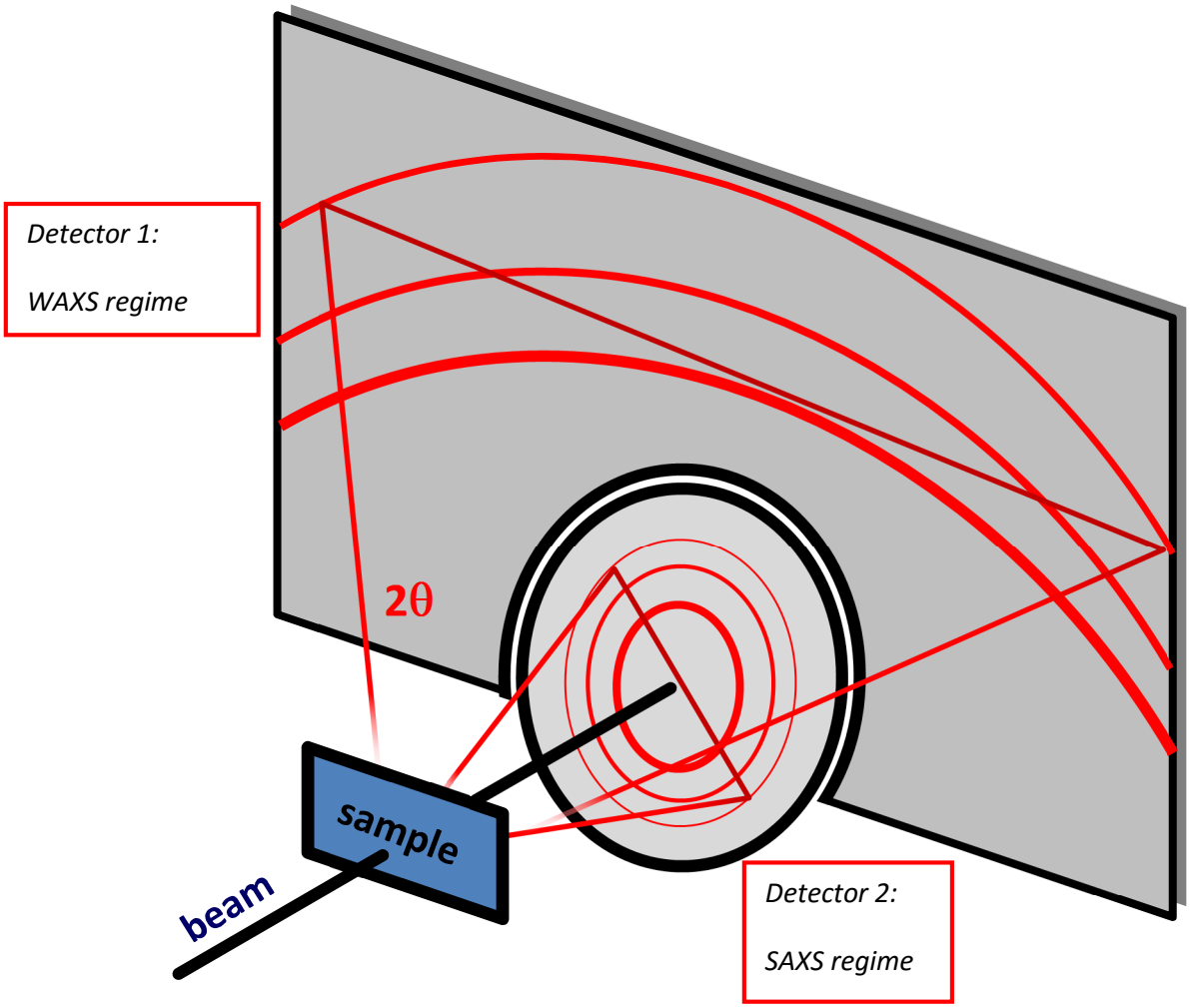

Figure 6: In this rough sketch the setup of the detectors is being shown, hence the actual arrangement. The SAXS detector is embedded into the WAXS detector to cover the entire SAXS and WAXS range with the smallest gap possible between both regimes.

The detector sample distance was also set accordingly to the energy of the beam used, to ensure a Q-range from around 0.1 nm^{-1} to about 5 nm^{-1}, the WAXS interval reached from about 8 to 43 nm^{-1}. The distance between detector and sample to achieve this at a wavelength of approximately 0.98 $\dot{A}$ was at ca. 21.35 cm. This resulted in a total of 9 measurable peaks in this regime, with a maximum of 2 orders for the {100} and {101} planes.

Unfortunately, the correct measurement of the background didn't always work properly for the first series with the biggest core, as the high brilliance of the beam seemed to alter the concentration of the solution locally and also burnt some of the sample to the walls of the capillary. Thus the background was altered for the following measurement despite the flow-through setup and the reduction of the used undulators from two to one and hence decreasing the flux onto the sample. To prevent these effects, extensive cleaning after each measurement, shortening of the time of measure to 0.05 seconds and re-recording of the background after a small number of runs were needed.

Data Analysis

This chapter will focus on the numerical analysis of the recorded SAXS and WAXS data using available commercial and freeware software packages such as *GIFT* [33] and *ATSAS* [24] and self-written routines using Mathematica and Excel.

All of the 2D images were reduced and corrected for the fluorescence, background and other effects, such as the signal of the filled and empty capillary, online by scripts written by Michael Sztucki. Unfortunately, error propagation was not included, which actually is of utmost importance as the variance of the scattering is only in the range of 6% at most at the absorption edge and considerably less away from it. As we used the reduced χ^2-method, this value is of utmost importance. Therefore, we re-binned the data using the software *PCGTools* by G. Popovski, which essentially takes the average of the amount of the points one wants to be binned and calculates the error made by the merging of the points [34]. These curves are then used to fit the *SAXS* data and evaluate the WAXS spectra.

Anomalous Small Angle X-Ray Scattering Data

The data recorded was analysed in several ways using various fit methods. The general routine involves the calculation of the intensity of the scattering by our particles by *eq. 26*.

Decomposition of the three contributions

It would have also been desirable to simply decompose the measured spectra into non-resonant, cross and resonant terms, to evaluate the resonant term with the traditional SAXS methodologies. But, as stated in the experimental section, the conditioning number of the system needs to be low enough to ensure a unique and meaningful solution to any matrix inversion. As we had to decrease the time of measure to about 0.05 sec, the counting statistics and the resulting relation between the total intensity and the error in intensity were seemingly not favourable enough to arrive at a good result using this precise method. The decomposition was first attempted via the program from Michael Sztucki and subsequently by a self-written script in Mathematica following Eigenvalue decomposition [21]

As the three parts of the solution, the non-resonant, cross and resonant term, essentially fulfil Schwartz's inequality, one can also include a sort of light, but ultimately insufficient, "quality control" of sorts. [21]

$$S_{\mathrm{OR}}(Q)^2 \leq 4\ \mathrm{S}(Q)_O\, S(Q)_R \tag{49}$$

with

$$S(Q)_O = \Delta f_0{}^2 F_o(Q)^2 \quad \textbf{(50)}$$

$$S_{OR}(Q) = 2\,\Delta f_0 \cdot f(E)'\, F_o(Q)\, \nu(Q) \quad \textbf{(51)}$$

$$S(Q)_R = [(f(E_3)')^2 + (f(E_3)'')^2]\, \nu(Q)^2 \quad \textbf{(52)}$$

as being described in [21]. Hence, as a point fails the above criterion, it can be dismissed. Unfortunately, it was not possible to arrive at a reasonable solution of the resonant scattering term for our particles.

Fitting of the particles

The form factor plugged in to this equation follows exactly *eq. 41* applied in the framework of *eq. 25*. If we now assume a core-shell configuration for both the counter ions and the resonating ions, a fit with 7 variables is achieved for a simple system consisting of only one shell.

Because it was extremely difficult to get a fit with physically meaningful parameters for the largest core series, non-spherical form factors have been used to allow for fits.

Ellipsoid of revolution:

An ellipsoid of revolution can be written as [16]:

$$F_{\text{ellrev}}(Q) = \int_0^{\frac{\pi}{2}} F_{\text{sphere}}(Q, r(R, \alpha, \epsilon))^2 \, \sin(\alpha)\, d\alpha \quad \textbf{(53)}$$

with

$$r = R(\sin(\alpha)^2 + \epsilon^2 \, \cos(\alpha)^2)^{0.5} \quad \textbf{(54)}$$

This represents the definition of an ellipsoid of revolution with the factor ϵ being defined as the eccentricity:

$$\epsilon = \sqrt{\frac{a^2 - b^2}{a^2}} \quad \textbf{(55)}$$

Values of $\epsilon < 1$ correspond to oblate, values >1 to prolate ellipsoids.

Obviously one has to integrate to arrive at the azimuthally averaged form factor for the ellipsoid of revolution, which hast to be done numerically. This can be a very time consuming step in a fitting

routine, as this has to be done for every iteration with the integral itself not always being "well behaved" in the case of core-shell particles.

For these systems additional restrictions have to be implemented to ensure a geometrically correct solution for the parameters, especially concerning the maximum and minimum values of the axis describing the core and the shell of the NC.

To speed up the fitting process itself, the following formula was retrieved [35]:

$$I(Q) \propto \sum_{n=0}^{\infty} (-1)^n \, 72 \, \frac{(2n+2)(2n+5)}{(2n+6)!} (2qa)^{2n} \sum_{r=0}^{n} \frac{n! \, \epsilon^r}{r! \, (n-r)! \, (2r+1)} \qquad \textbf{(56)}$$

This allows for a faster calculation of the spectrum of an ellipsoid of revolution and thus speeds up the fitting process significantly if one chooses the right algorithm. But there still exists a problem with the break off criterion for the infinite sum. One way to work around this fact is using the estimation of the size and aspect ratio by *eq. 32* and using these parameters as the basis for an ellipsoid. Then we fit the equation above to this fictive particle as a function of the number of terms in the sum *n* and used a slightly bigger estimate as value for the fitting routine itself. To ensure a reasonable number of terms, we used the decreasing change in the χ^2 with increasing *n* as a stopping criterion.

This however worked quite badly for our particles. The reason for this circumstance doesn't lie within the approach itself, but in the program used to fit the data. The non-linear methods to solve the resulting equation has an analytical evaluation built in. In certain cases, such as the continuous form factor, this produces a considerable acceleration of the fitting process. In the case of sum within a sum the number of terms to evaluate needed to be stored in the memory and can exceed the RAM of the PC used and consequently crash the machine. Another small issue is the assumption taken with the approach above. The expansion in *eq. 56* doesn't consider polydispersity, therefore assumes a purely monodisperse solution. This leads to particles with an aspect ratio and size quite above the actual physical dimensions of the NC, which means that the smearing of the curve is achieved through the azimuthal averaging and not the actual polydispersity present in our systems. Additionally, as the minima shift slightly to the left when compared to a monodisperse system, due to the volume squared term in *eq. 26*, a bigger mean size of the particles is implicated. Still, use can be made of the result by choosing slightly different larger numbers of n and generous restrictions on the geometric parameters in our fit.

A similar formula seems to be possible for tri-axial ellipsoids, as was calculated by Debye [35], but the mathematical complexity of such a derivation goes beyond the scope of this work and the mathematical back ground of an engineer. A simple idea to arrive at a similar formula would be to do a series-expansion of the cardinal sinus and use the approximation of Glatter, via "binning" of the inner distances of equal lengths [11], consequently reduce the double to a singular sum in our Debye equation. If an analytical expression for the pair-correlation function for a tri-axial ellipsoid would exist, one could

easily arrive at a trivial integral and thus again arrive at a similar expression. This would also be possible for any other convex shape that would allow for such treatment. We hence used the conventional form factor for tri-axial ellipsoids [16]:

$$F_{\text{triell}}(Q) = \frac{\pi}{2}\int_0^{\frac{\pi}{2}} \int_0^{\frac{\pi}{2}} F_{\text{sphere}}(Q, r(a,b,c,\alpha,\beta)) \sin(\alpha)\, \mathrm{d}\alpha \mathrm{d}\beta \tag{57}$$

With

$$r(a,b,c,\alpha,\beta) = ((\alpha^2 \sin(\beta)^2 + b^2 \cos(\beta)^2)\sin(\alpha)^2 + c^2 \cos(\alpha)^2) \tag{58}$$

This form factor slows down the fitting process quite a bit, as two separate numerical integration have to be calculated every single iteration, which adds up considerably if core-shell form factors are being used. This also drives up the amount of fit parameters, if one wishes to extract the compositional information too and renders the result highly instable and heavily constrained, due to geometric reasons.

Continuous and discontinuous Interfaces:

Because it was also predicted in Ref [36] that the strain in the CdSe/CdS core-shell particles is reduced through interdiffusion of Se with Sulfur (S), a form factor describing a diffuse interface and multiple step-like transition in electron density from core to shell was tested.

The multiple step like form factor was realised following *eq. 25* for the spherical core shell form factor, written as:

$$\begin{aligned} F_{2-\text{shell}}(Q) = 3\Bigg(& \nu s_1 \frac{4\pi {R_1}^3}{3}\left(\frac{\sin(QR_1) - QR_1\cos(QR_1)}{(QR_1)^3}\right) \\ & + (\nu s_2 - \nu s_1)\frac{4\pi {R_2}^3}{3}\frac{\sin(QR_2) - QR_2\cos(QR_2)}{(QR_2)^3} \\ & + (\nu s_3 - \nu s_2)\frac{4\pi {R_3}^3}{3}\frac{\sin(QR_3) - QR_3\cos(QR_3)}{(QR_3)^3}\Bigg) \end{aligned} \tag{59}$$

for a particle with 2 shells, with the value of the indices decreasing outwards. With an increasing number of shells this model gets more and more accurate, but also more computationally expensive even for programs that handle analytical formulas quite well. In this work a 2 shell and 3 shell model, as well an analytical, continuous form factor were employed.

The functional shape of the Fermi-Dirac statistic has a step like form at 0 K and starts to smear out with increasing temperature. This can be used as a function for the $\Delta\rho(r)$. The feature that sets it apart from other possible expressions such as the error function is the analytically solvable integral for the

polydisperse case under some simplifications [37]. The electron density as a function of the particle radius thus can be written as

$$\rho(r) = \frac{m}{1 + \exp(\frac{r - R}{d})} \tag{60}$$

Where R represents the radius of the particle, m the numeric value of the electron density at r=0. In relation to the Fermi-Dirac statistic, d has the same effect as the temperature, thus controlling the smearing of the profile with increasing value. To allow for integration, *eq. 60* needs to be represented through hyperbolic sines and cosines [37]:

$$\rho(r) = \frac{m \sinh\left(\frac{R}{d}\right)}{\cosh\left(\frac{r}{d}\right) + \cosh\left(\frac{R}{d}\right)} \tag{61}$$

This expression is only exact enough for application for values of $d/R < 0.1$ [38]. This doesn't limit its use in the case of anorganic crystals, as this would roughly translate to an extension of the core to a factor of 1.6.

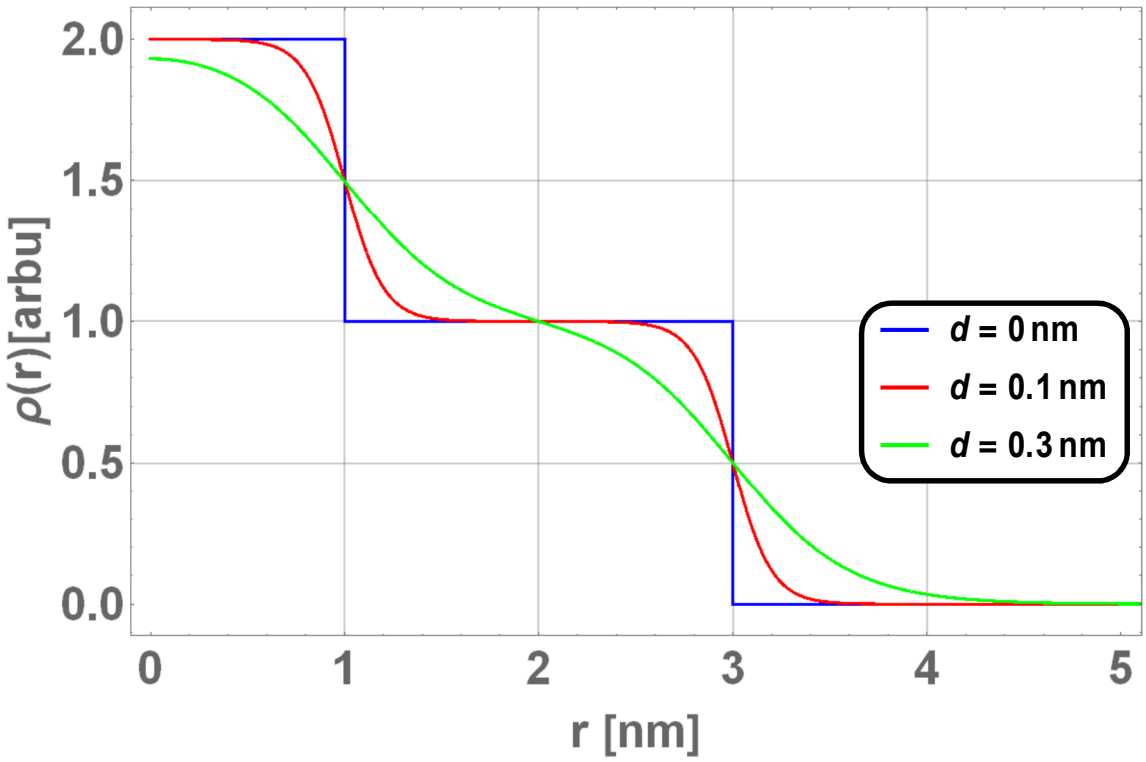

Figure 7: Several electron density distributions $\rho(r)$ of particles with the same parameters for the core radius and shell thickness, but with varying shape parameter d, are plotted against the distance to center of the particle. The electron densities are purely fictious and are selected for the presentation of the principle.

With $d = 0.3\ nm$ being one tenth of the total particle size, it is becoming evident, that an easy distinction between core and shell is increasingly difficult (Fig. 7). Thus greater care has to be taken when evaluating the electron density, as the parameters describing the electron density only resemble the actual values in extremely simple cases. For instance, *m* represents the electron density of the core in the case of a compositionally singular particle. The addition of multiple shells has been treated in ref [37] and will not be expanded on any further in this work. Still, in the case of core-shell models, additional conditions regarding the electron density of the core have to be employed to arrive at physically meaningful solutions, which will be discussed in the next paragraph. Even more, there is no guarantee that the shape parameter *d* yields the same value for every interface present in our particle. Hence we decided to use different *d*'s in our evaluation for each interface present. This has the drawback that the range of possible values has to be limited, to hinder "bleeding" of the structures into each other, and the addition of another parameter to fit in our model, which in turn increases the total time needed for a solver to find a solution.

Additionally, the definition of the core and shell is not quite as straight forward as in the classical stacked core-shell model from *eq. 59*. For the appropriate fit-intervals, one has to consider the following: The total particle radius still comes out as the sum of the nominal radius of the core *rc* and the nominal thickness *t* of the shell, but the real shell thickness comes out as twice the nominal core radius. This is illustrated in the following Fig. 8:

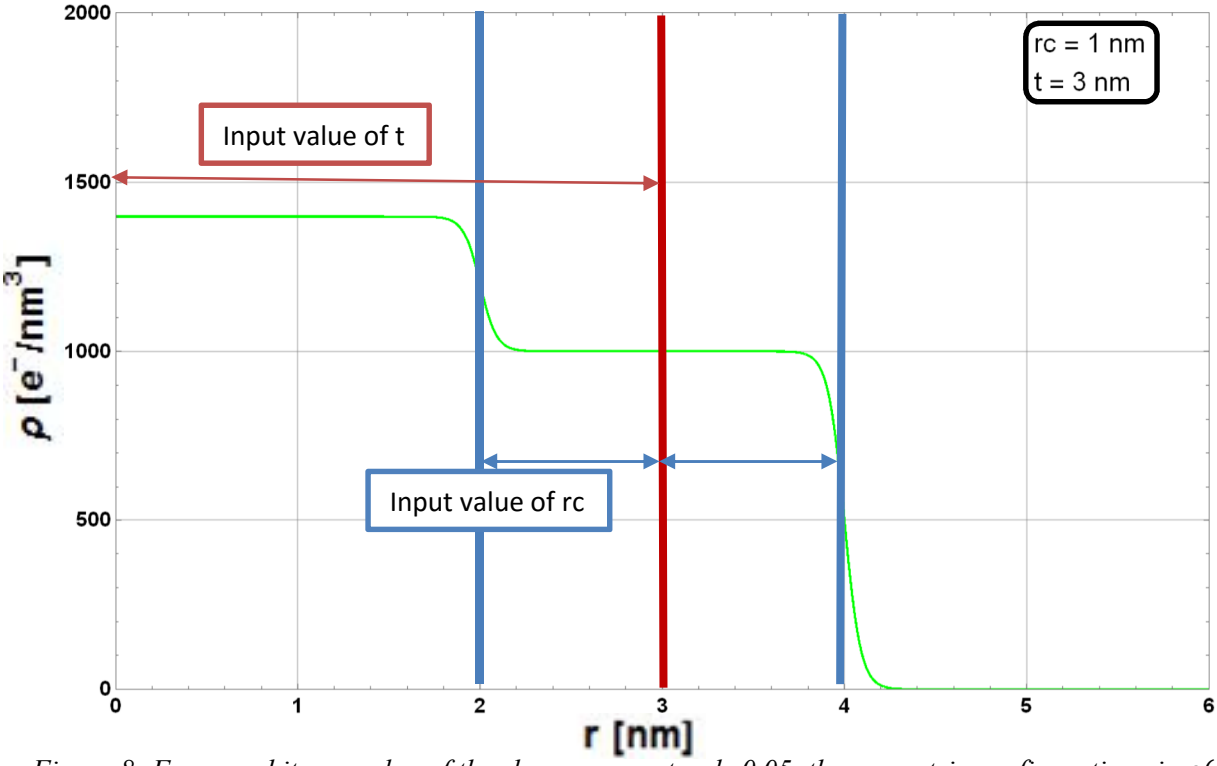

Figure 8: For an arbitrary value of the shape parameter d=0.05, the geometric configuration via $\rho(r)$ of the particle is depicted versus the distance from centre r. The thickness of the shell comes out as two times rc, the core size as t minus rc.

So finally, the analytical integration and result of *eq. 61* is quite extensive in length. We only write down result for the analytical case of the core, the general case can be read in ref [37]:

$$A(Q) = \frac{m}{N_{\text{core}}} 4d \ \frac{\pi^2}{Q^2} \cosh(\mathrm{d\pi Q}) \cdot (\mathrm{d\pi Q} \cdot \coth(\mathrm{d\pi Q}) \ \sin(QR) - QR \cos(QR)) \quad \textbf{(62)}$$

With

$$N_{\text{core}} = \frac{4\pi \mathrm{m}}{3} \cdot R \cdot (d^2\pi^2 + R^2) \quad \textbf{(63)}$$

This can now be plugged into *equation 36* and again analytically integrated for a normal distribution with the integrational boundaries set from – ∞ to ∞, which translates into a negligible error for "small" polydispersities of *<10%.* Again, the result is very long and we will refer to ref [37] for further details such as the formula for core-shell particles.

Because of its length, the implementation for anomalous analysis of the data the same way as in *eq. 25* is quite cumbersome and exhibits a high sensitivity to fit parameter values leading to long calculation times for the pc. But in cases where we are sensitive to the difference of the electron densities, it is still possible to evaluate the profiles of particles in a timely manner. To even further check if the solution found is of physical significance, one could also plug in the pair distribution of the particle, obtained from *GIFT* [33], into *DECON* [38] and compare the solutions to each other.

SAXS analysis: Expansion of Debye's formula

The data obtained from the preceding evaluation with a continuous electron density-profile did not produce useful result concerning the quality of the information retrieved or the time needed to get useful fits. Hence the necessity of the knowledge about the actual particle shape becomes obvious. To reduce the time needed to fit the data, even a rough estimation of the shape is also helpful, as the hyperplane on which we move via our non-linear solver seems to have non-favourable concave features. Therefore, we used the series expansion of the cardinal sinus, of which the second, fourth and sixth moments were used. In the case of a sphere, the terms resemble the *p(r)* as defined by Glatter [11]. To fit the first three moments one needs to consider, following [11],

$$I(q) = I(0) \ (1 + 2 \sum_{n=1}^{\infty} \int_0^{2R} \frac{1}{2} r^{2n} \left(\frac{3r^2}{R^3} - \frac{9r^3}{4R^4} + \frac{3r^5}{16R^6} \right) dr \ \frac{(-1)^n}{(2n+1)!}) \quad \textbf{(64)}$$

to normalize *I(0)* to 1 and fit the first part of the curve [12]. The first term in *eq. 64* yields the radius of gyration as the second moment, the second and third terms represent the fourth and sixth moments of a spheroid surrounding the particle investigated. This allows for a qualitatively sound estimate of the

shape of the particle. This can be seen if we plot the fourth and sixth momenta of several particles with identical volume and two identical axes against the aspect ratio of the particle. (Fig. 9)

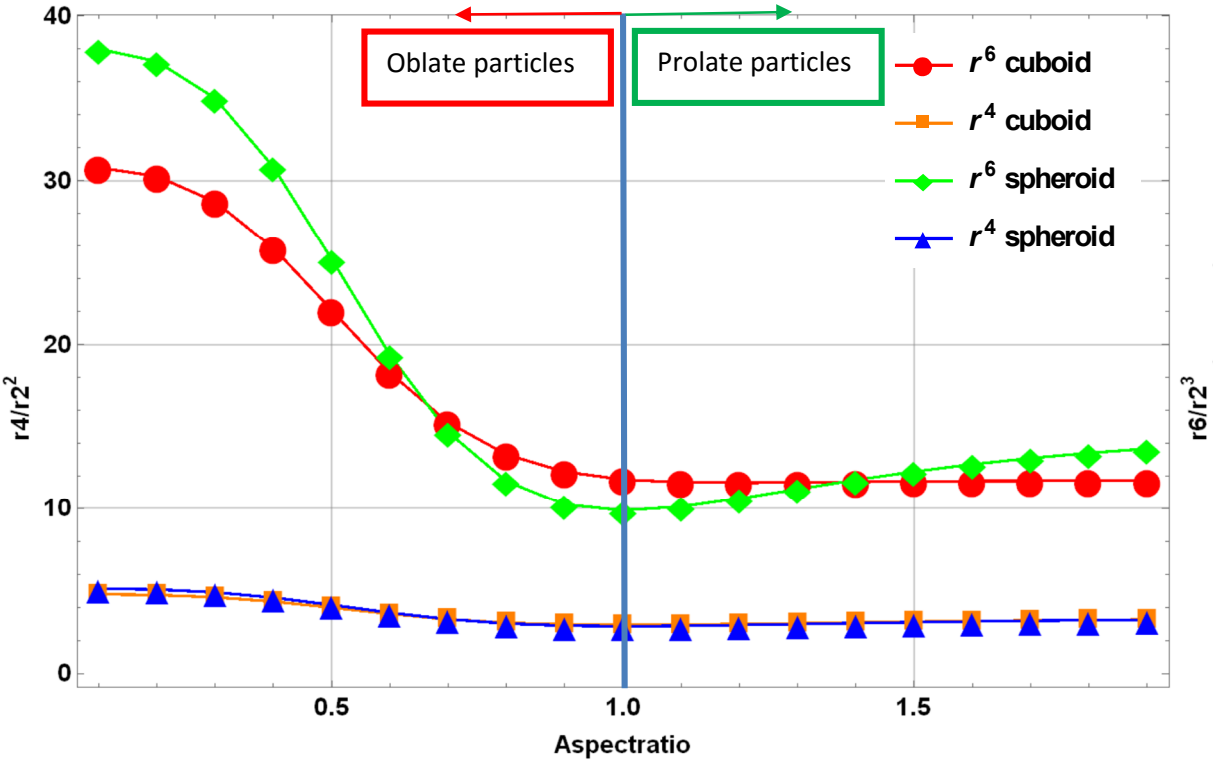

Figure 9: The moments of power 0 of spherical and cuboid particles versus different aspect ratios and two axes being equal. A clear distinction between prolate and oblate particles in term of the value of the moments is observable.

The analytical values of the moments were calculated using a plugged in form factor in *equations 34-36*, which could also be used to fit the approximate dimensions of a particle in the Guinier portion of a spectrum. If we compare these ratios of the moments, you can more or less definitively determine the shape, meaning the differentiation between prolate, spherical and oblate cases.

The case of the perfect sphere can be calculated analytically. This results in values not depending on the size of the particle, but only on the spherical geometry. These integrals turn out to:

$$\Delta r2 = \frac{3R^2}{5} \tag{65}$$

$$\Delta r4 = \frac{36R^4}{35} \tag{66}$$

$$\Delta r6 = \frac{32R^6}{15} \tag{67}$$

Now divided to achieve expressions of power 0:

$$\frac{\Delta r4}{\Delta r2^2} = 2.85714 \tag{68}$$

$$\frac{\Delta r6}{\Delta r2^3} = 9.87654 \tag{69}$$

Hence, any particle exhibiting these vales for the values defined in *eq. 68* and *69* is of spherical symmetry. Interestingly enough these values don't seem to deviate much for other geometries such as cuboids, which means that this method is more sensitive for the ratios of the axis of the body of circumference, than the actual geometry itself.

Concerning the actual evaluation process, a word of caution has to be ushered here. For analysis, the usable part of a recorded curve is being extended through the use of additional terms, but still largely coincides with the Guinier part of the data [11]. To demonstrate the effect of an ill-suited interval to fit data to, spheroidal particles were simulated. All of these particles have the same volume, yet differ in the aspect ratio of the axes, two of which have the same length. Now the simulated data was fit with a polynomial of third degree within the same interval, with the fit parameters representing the second, fourth and sixth moments. (Fig. 10)

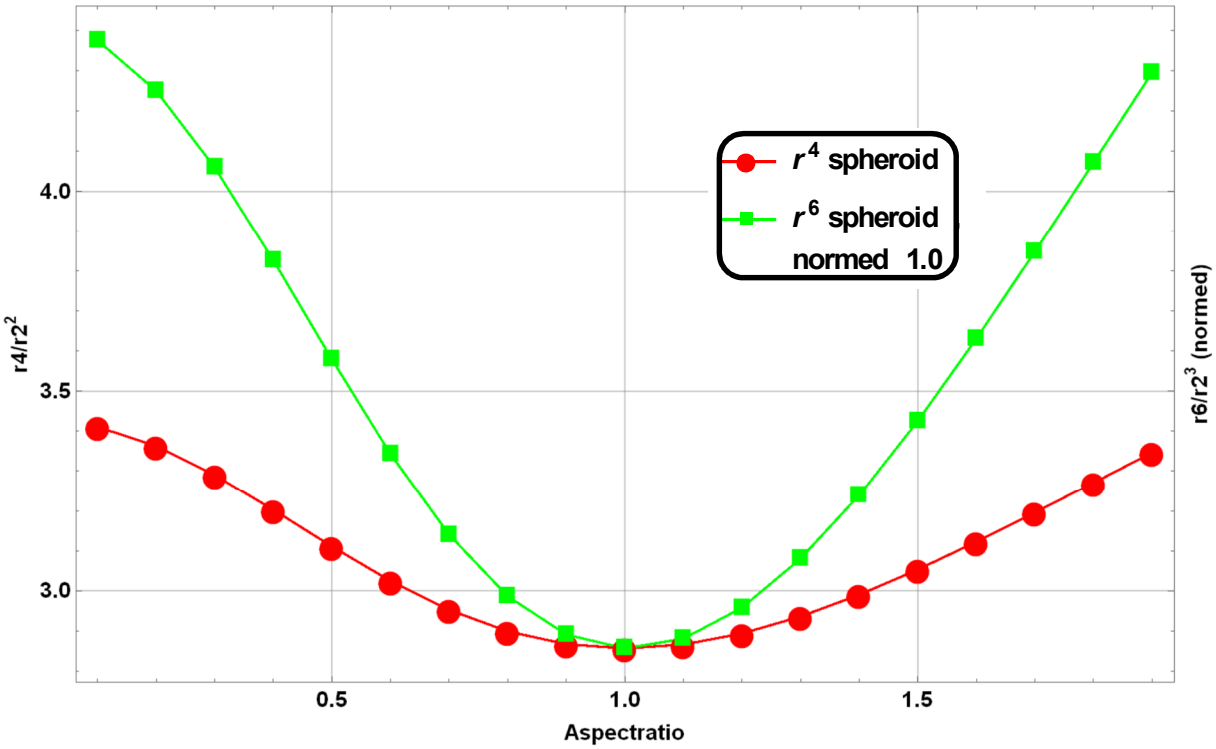

Figure 10: Fit of the moments of a simulated spheroidal particle with two axes being equal. The sixth moment is also normed to the fourth moments at an aspect ratio of 1.

A clear deviation of the moments from Fig. 10 is visible for particles with an aspect ratio > 1, as the sixth moment exhibits a clearly different behaviour. Thus with careful evaluation of the fit interval, we can clearly distinguish between prolate and oblate particles. At the very least we can determine if a particle is equi-axed or not, as we simply can determine the integral for a spherical particle with the radius *R* via *equation 60* for the first three contribution of the sum.

SAXS analysis: Dammin

As shown in ref [32], the shape retrieval software *DAMMIN* by Svergun [31] can also be employed to determine the shape of semiconductor nanocrystals, with additional information on core-shell structure. In this work we return to this program, as the compositional information was very hard to fit via ASAXS for the largest core series, as the shape seems to deviate severely from the spherical case. We hence tried to determine not only the shape of the particles in our solution, but to maybe even extract some information on the distribution of the selenium atoms via the occupancy density [32]. The occupancy density represents the average possibility of any dummy atom being at a certain position within the particle. Therefore, as the data recorded is nothing else than a Fourier-transform squared of the electron densities in the particle, the occupancy density should coincide with the electron density in the particle because the dummy atoms all have the same scattering cross-section. Hence, the occupancy value should be sensitive to the relative decrease in electron density of ~17% from the CdSe core to the CdS shell, if the theoretical electron densities of CdSe and CdS in the Wurtzite phase are met. Burian showed via his "onion"-evaluation, that at least a decrease of roughly 33% is possible to be detected, although the higher density phase was located in the shell, which greatly improved the statistical significance of the shape regarding the particle/solvent interface.[32] A different possibility is the so-called linear evaluation, in which a cylinder of a few dummy atoms diameter is randomly stuck through the structure through its center for a few thousand times in random orientations and the size in that direction is evaluated.

However, the particles analysed here are not of spherical, but of rather elliptical shape, which made the evaluation of the occupancy values and the shape quite challenging. To generate meaningful data, we ran *DAMMIN* in expert mode and averaged 5 structures of each particle, with the dummy atom size being in the range of one monolayer of CdS in Wurtzite structure (~ 0.3 *nm*), to see if any extrusions from the particle surface or smearing effects would be lost via the averaging procedure. Additionally, the number of splines to fit the curve was increased up to 50 and the number of harmonics set to a value of 25. Burian showed that a higher number of spherical harmonics doesn't significantly improve convergence after a threshold of about 20. [32]

To our disadvantage, the number of Shannon-Channels wasn't always at the lower limit of 10, which probably doesn't only limit the information gained on the core in core-shell particles, but also could lead to ambiguity concerning the shape! Shannon channels essentially determine the interval of the sampling,

in our case the interval of q at which data is measured, and consequently are a measure for the information content. [11] As DAMMIN operates under assumption of monodisperse solutions, smearing of a polydisperse curve is achieved via larger aspect ratio, particle size and/or faceting of the structure. All of these effects have to be taken into account, when performing simulations using *DAMMIN*.

SAXS analysis: DAMMIF

Because the average time to fit our particles with *DAMMIN* was in the range of 24-30 hours per sample, we decided to try out the optimized and accelerated successor, *DAMMIF* [40]. The average time to simulate a sample decreased to ca. 1-2 hours, but possibly because of the now increased and effectively "infinite" search-volume, the solutions found exhibited strange shapes and exceptionally rough surfaces, way off any physically possible structures. Thus we decided to continue using the slow, albeit reliable *DAMMIN*.

WAXS data analysis:

The analysis of WAXS data was done by a self-written routine that allowed for individual subtraction of backgrounds, aided by further subtraction by spline interpolation, robust multi-peak fitting routines for several peak shapes, ranging from Gaussian to Voigtian functions, and automated strain and size determination by peak-shift analysis and Williamson-Hall plot.

As the background estimation measurement for the series with the biggest core didn't yield useful data, we had to resort to different means. To first estimate a background, the spectrum was Fourier-transformed and then "cleaned" from any frequencies that changed the total shape only on a minute scale, similar to a singular-value decomposition. The criterion for the total change needs to be set by the user via a parameter. To arrive at a usable spectrum, one needs to "play" around a little with the parameter until a satisfactory result is achieved. Hence, all sharp features of our curve were filtered out which left us only with the rough shape of the spectrum. Against the principle of other methods, a simple low-pass filter was not sufficient, as also higher frequencies seem to determine the general structure of the curve. Upon back transformation, the second derivative was taken and any zero of the resulting curve was used as a sort of "fulcrum" for the following interpolation via b-splines of an odd order. This "quick and dirty" method is demonstrated for the ID02 standard PBBA, which was shortly described in the theoretical section of this work on *page 11*, in Fig 11.

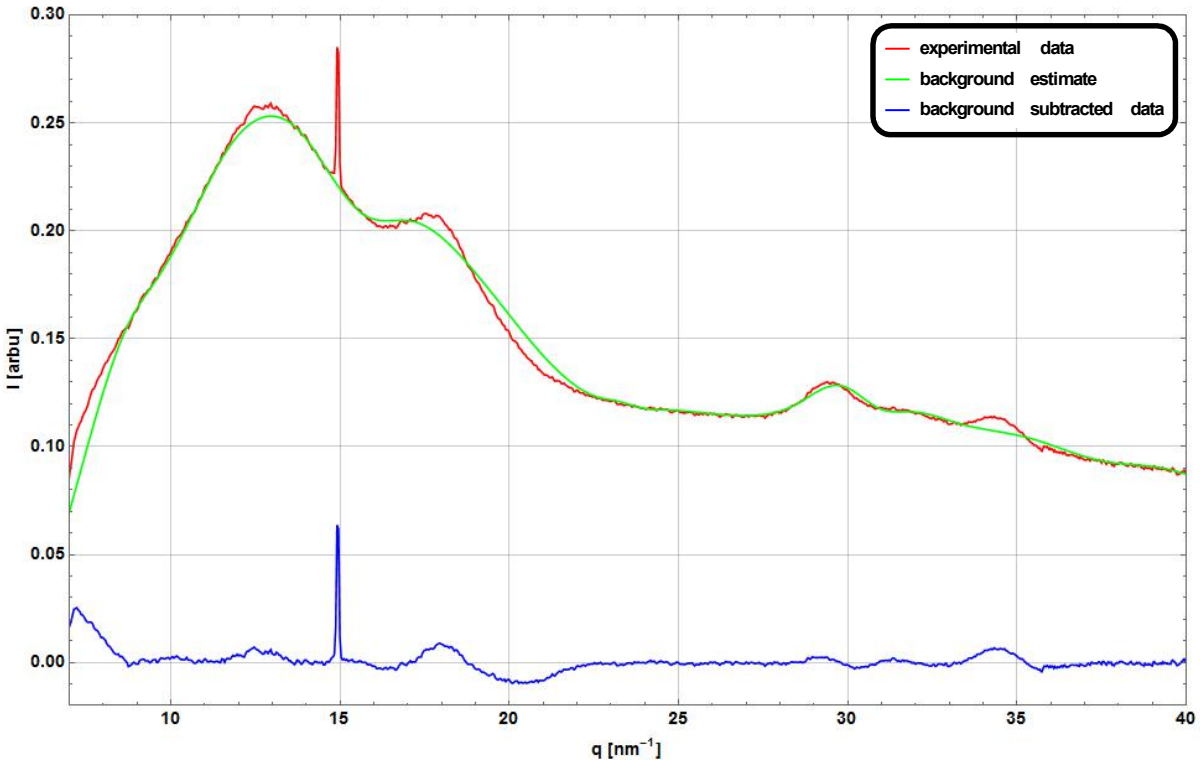

Figure 11: The red spectrum is the recorded data of the PBBA standard from ID02. The green line was calculated by the procedure described above and subsequently subtracted to arrive at the background corrected blue line. The sharp peak of the PBBA was successfully reduced, but broader features, such as the shoulder right of the peak at 15 nm^{-1}, don't get approximated well.

For sharp features, such as the PBBA reference sample, this worked quite fine. But peaks of nanocrystalline solutions usually do not exhibit the needed sharpness due to for instance size effects. Hence, this method was not able to restore a sufficient background, which could lead to distorted, virtual effects in the spectra. Thus we simply modified a later measured background to fit the recorded curve in areas with no peaks via a similar method, which yielded much more satisfactory results.

Because of the limited range of the *WAXS* – detector, the number of peaks available is limited and no higher orders other than for the reflections {100} and {101} are present. (Fig. 12)

a)

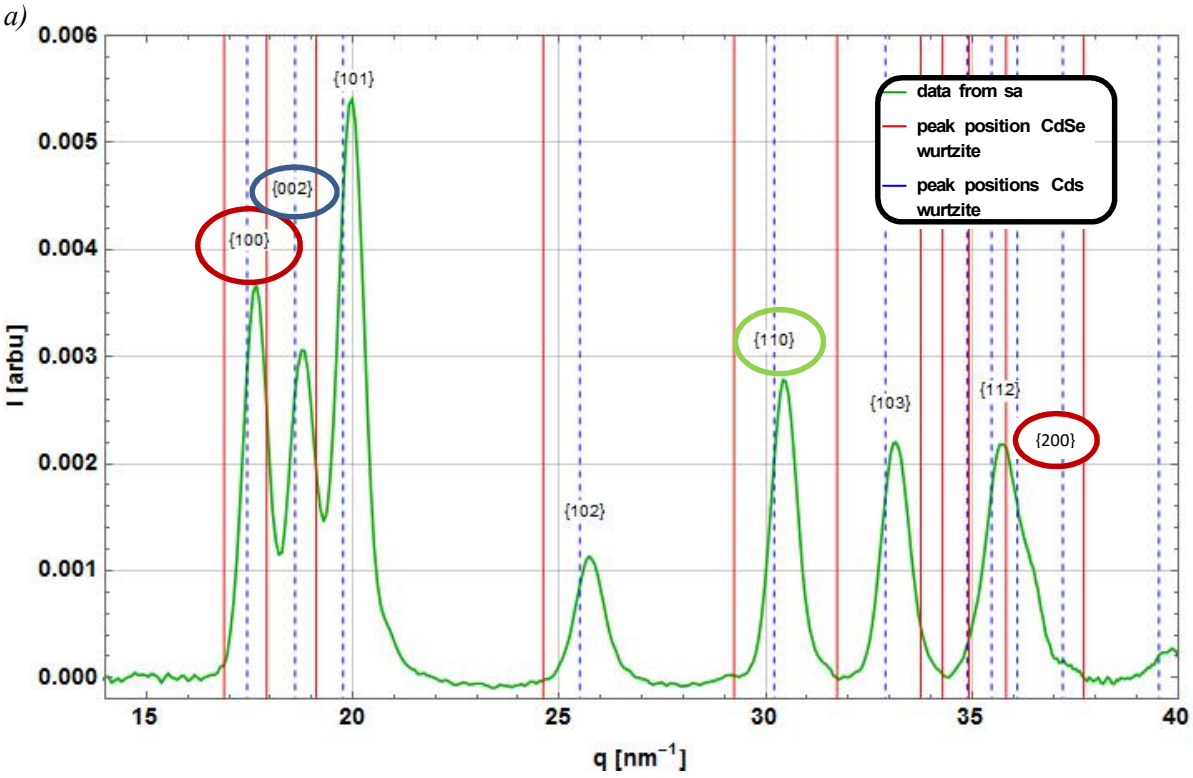

b)

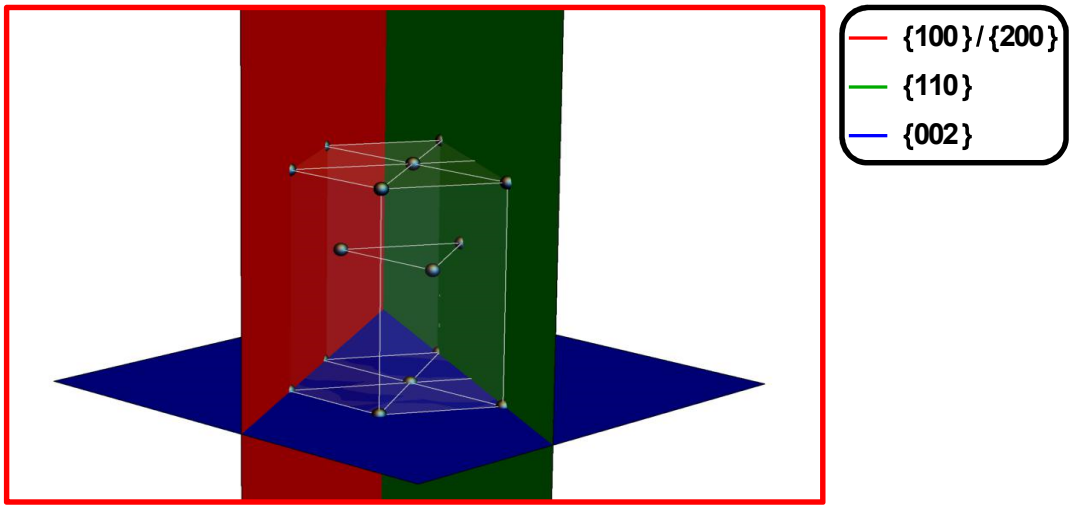

*Figure 12: a) A sample spectrum, from the particle **sa**, with the hkl-planes indicating the peaks. b) For better visualisation, the planes of interest are shown. The red and green planes represent the elastically similar planes which could be used for Warren-Averbach analysis. The blue plane is the basal plane, which can show broadening of certain peaks due to planar faulting.*

Even for those, only two orders are existent and therefore not suited for a detailed and bias free analysis such as Warren-Averbach. A workaround is still possible, under the assumption that crystal planes, that behave very similar elastically, could also be used for such an analysis. [41, 42] This still leaves us with the planes (100), (110) and (200), which are shown in Fig. 12 b). Because the (200) plane was quite hard to evaluate as it essentially sits atop the (112) plane, the evaluation was never conducted. Furthermore,

the (100) and (200) plane would not exhibit planar faulting due to growth, this analysis would have been futile, as the breadth of the peaks also scales with the *l* value of the planes observed. As these planes normal is perpendicular to the <001> direction, no broadening should occur for them. [12] In the case of the *fcc* crystal structure, an essentially equal criterion can be met, by calculation of the so called orientation factor. [41] This can be done here in a very simple fashion via

$$\Gamma = \frac{h^2k^2 + h^2l^2 + k^2l^2}{h^2 + k^2 + l^2} \quad \textbf{(70)}$$

with the h, k and l representing the indices of the plane. Thus, for similar gamma, the Warren-Averbach analysis can be used [43], but unfortunately no such planes of the possible zinc-blende structure of CdS and CdSe fall in the range of our measurement and consequently fail this criterion.

Thus we had to simply use all of the peaks available for the Williamson-Hall plot analysis, which does actually work quite well for small values of the (hkl), but diverges for large angles. Another small pitfall was the absence of a full range of a reference spectrum, which made the deconvolution after Stokes an unusable method. The breadth of the sole peak of our reference material, PBBA, yielded a width of 0.1 nm^{-1}. With the minimal peak width recorded at around 0.7 nm^{-1}, this yields a deviation of 1 % in the worst case following *eq. 17* and is practically of negligible influence for our samples. For the evaluation it was assumed, that the instrumental broadening at higher q-values in our spectra does not grow too much. Ideally, one would have to fit the instrumental broadening and subtract it from the data, as it is a function of the scattering angle. [43].

Because the peak shape could be approximated very well with a Gaussian, we did not deem it necessary to employ more sophisticated integral breadth models, such as in ref [43] or in [44].

For further evaluation the *PCG SWAXS* software [4] was used to simulate the theoretical patterns for the NCs investigated in this thesis. This is a very useful tool to gain further understanding of the crystalline structure of the particles, as shapes and compositions of the users choosing can be simulated and compared to the actual experimental results. The software essentially calculated *eq. 29* as described above and gives possibilities for refinement, such as rotation of core and shell relative to each other.

Results and Discussion

In the following chapter we take a closer look at the analysis of the data measured at ID02 in the ASAXS and WAXS regime and the relation between the results of both methods.

ASAXS

The results of the experimental work at ID02 at the ESRF are presented here in Fig. 13. For the smallest core series, the curves exhibit many minima except for the the core sample. This would imply, that the shape of the core is unfortunately not definitively retrievable, but a spherical estimate is still possible.

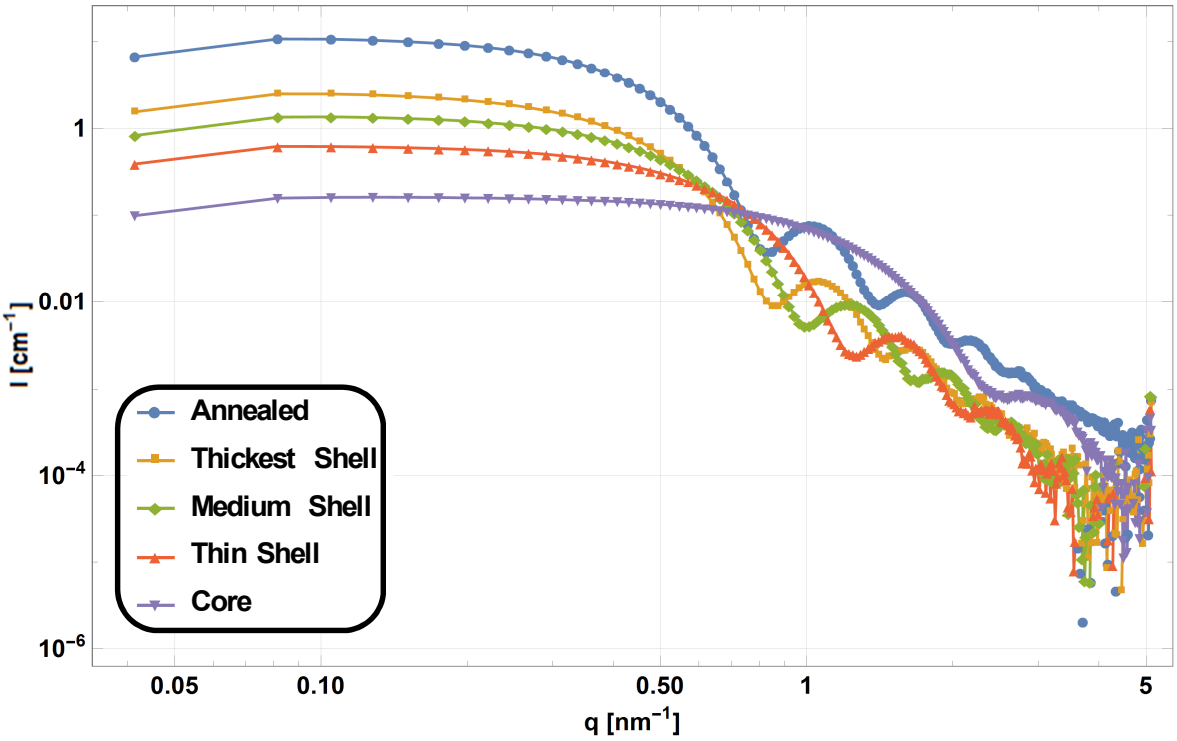

Figure 13: The recorded intensity I versus the scattering vector q is displayed in an overview plot of all the different sizes of the ***sc*** *series, measured at an energy of 12580 eV. The symbols represent the measured points; the coloured lines serve as guides to the eyes.*

From the position of the first few minima, a rough estimation of the size of the NCs is possible. This is because the minima must coincide with the zeros of the spherical Bessel function, if the geometry of the particle is indeed spherical. As the core particle of the **sc** series does not exhibit more than one minimum, this estimate loses its accuracy because at least 2 minimums are needed to derive spherical geometry via this method. Hence, a deviation of the positions of the subsequent minima also hints at a deviation from this shape.

The anomalous effect is depicted for this series' thickest shell particle in greater detail in Fig. 14, where the crossing of the energies is visible. The "crossing" of the data is due to the variation in scattering contrast of the Selenium atoms in the core, therefore changing the form factor of the core shell particle. The core itself shouldn't show this effect, which means that in this case all the energies lie strictly parallel, because the change in energy simply results in a change in total scattered intensity.

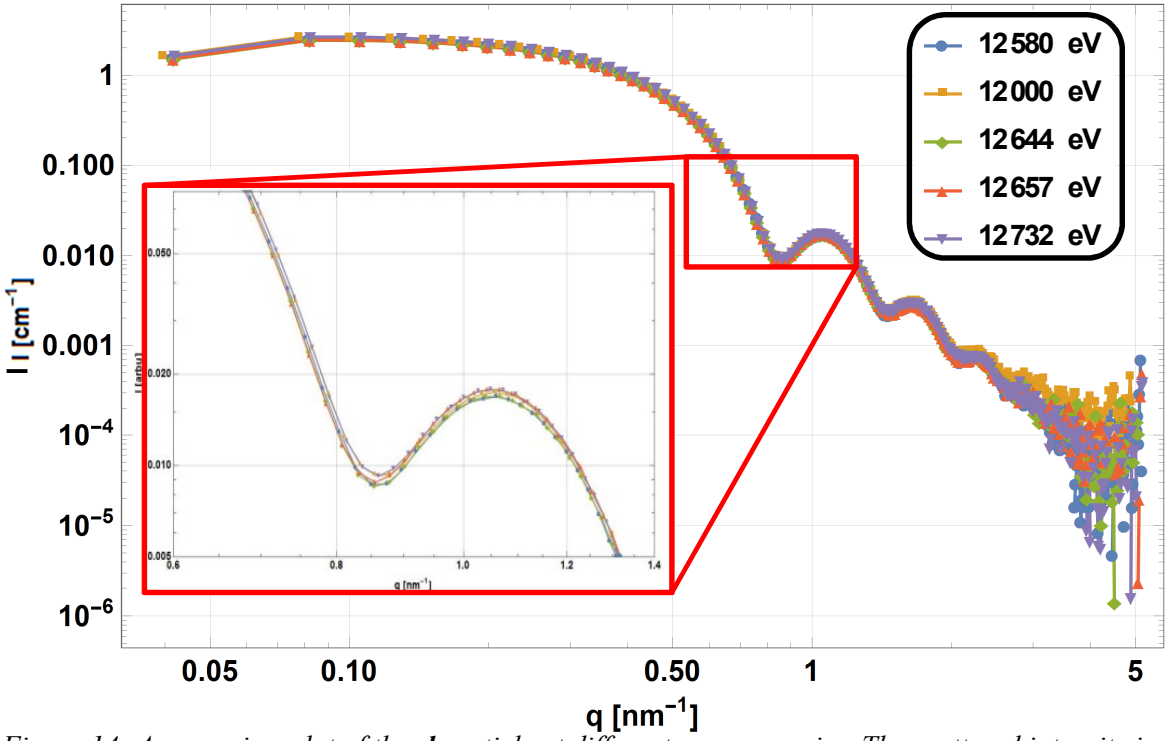

*Figure 14: An overview plot of the **sl** particle at different x-ray energies. The scattered intensity is plotted in absolute units [cm^{-1}] versus the scattering vector q. In the red box, the crossing of the energies can be seen, which illustrates the anomalous effect to be evaluated. Again, the symbols represent the measured data points, whereas the line serves solely as a guide to the eyes.*

The sample of the medium core Fig. 15 and largest core series Fig. 16 are shown below. Both series also exhibit the crossing with energies, thus implying a difference in concentration for the Selenium atoms for the core and the shell of the samples.

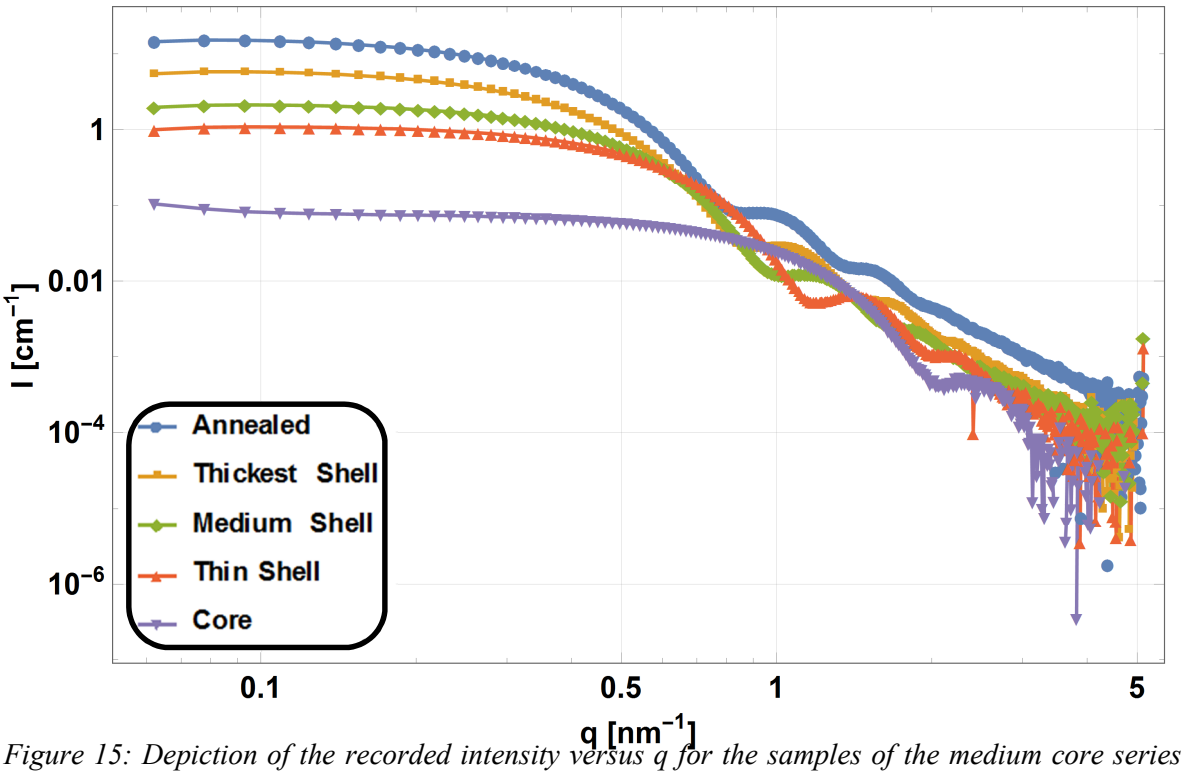

Figure 15: Depiction of the recorded intensity versus q for the samples of the medium core series at 12580 eV. Again, only one minimum is unfortunately useable for the core sample.

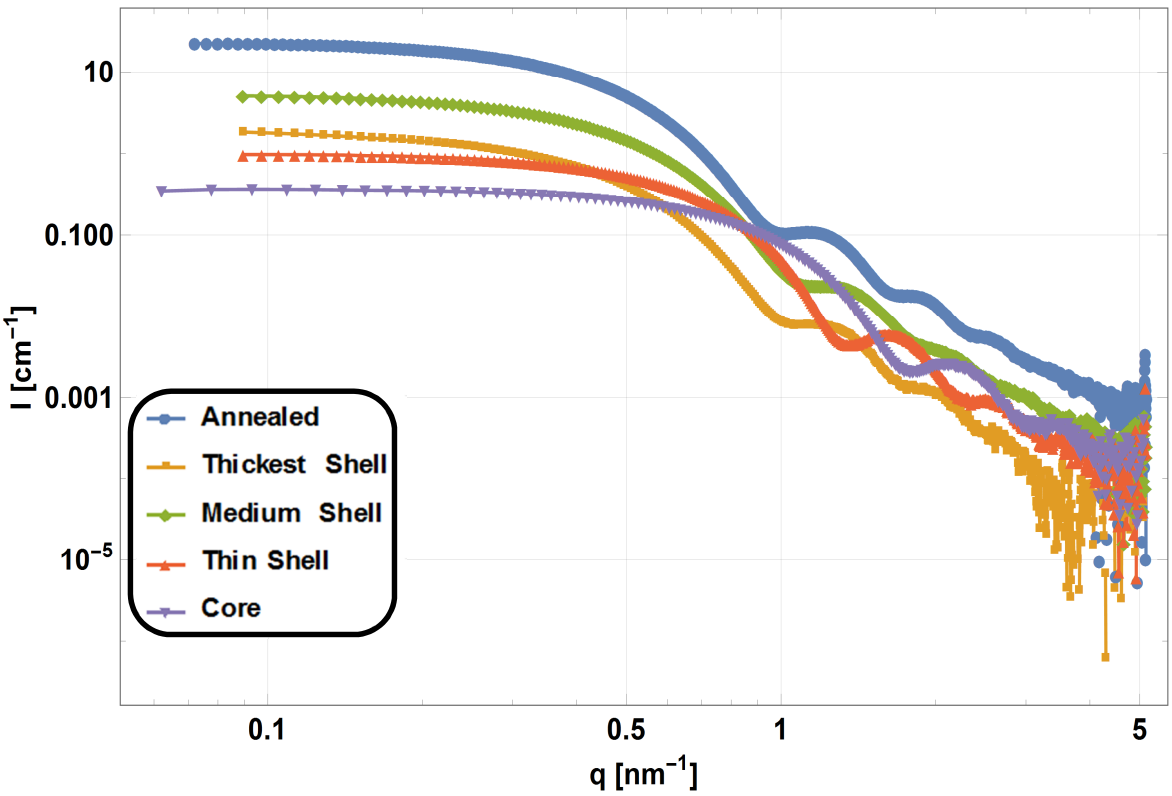

Figure 16: Depiction of the recorded intensity against q for the largest core series at 12580 eV. Even though the background could not be subtracted correctly, the deviation from the Porod Law [11] is not big.

Evaluation with spherical models:

As described above, we were able to fit the smallest and medium core series with the spherical core shell model as introduced on page 13 in *eq. 25*. But to arrive at meaningful results and to reduce the bias through the highly limiting model selection, we allowed first for 2 and later for 3 possible shells and assumed that no selenium ions were lost in growth and subsequent annealing of the samples. This means that we put an upper and lower limit of the total Se atoms in our particles, with the ideal number of selenium obtained from the fit of the core. Interestingly, both, the constraint on the total number of Se atoms and the extra number of accessible shells, didn't result in any graded like solution with several shells with decreasing amount of the resonant element, nor did the iterations get stuck on one of the boundaries set by the constraints. A representative result is depicted in Fig. 17.

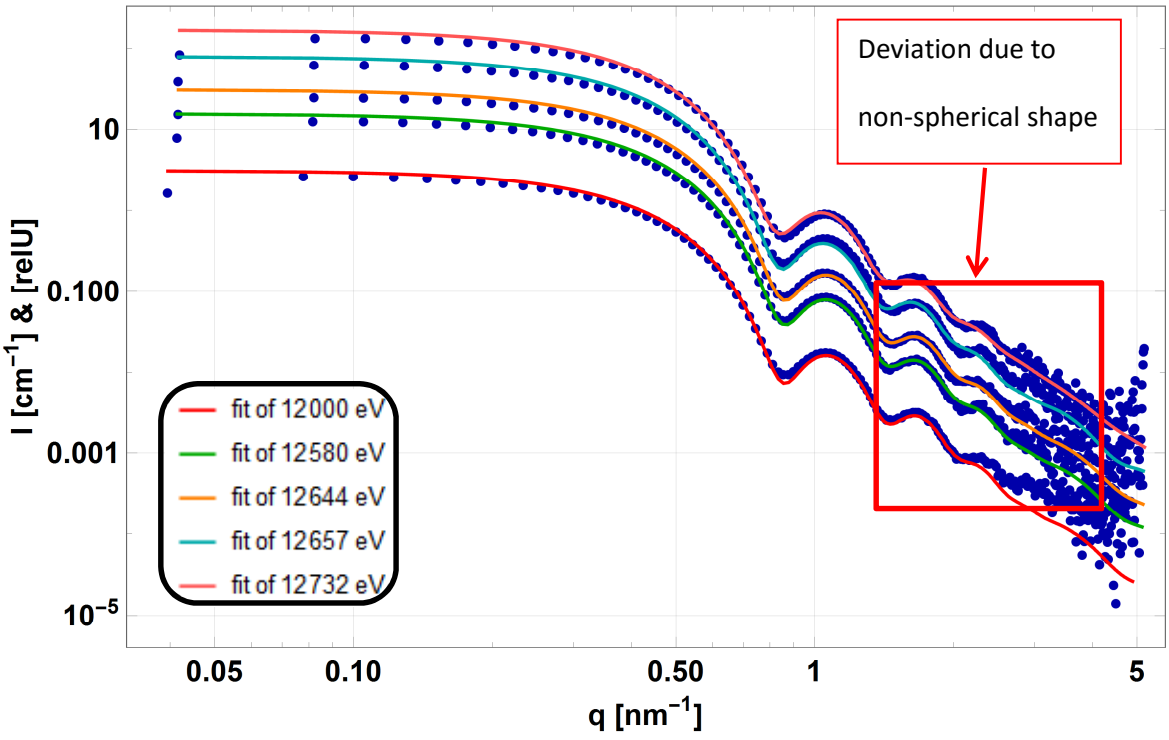

Figure 17: Fitted (lines) of the recorded intensity I versus the scattering vector q of the thickest shell particle of the smallest core series. The corresponding data to the fit of a certain energy is painted in blue dots. The data at different energies are shifted relative to each other by a constant factor except the 12000 eV line. The smearing of the third minimum is highlighted by the red box.

The fits for the **sc** series were of good quality, approximating several minima until the breakdown of the form factor, as shown in Fig. 17 for the **sc** sample. In this figure it becomes evident that even though the spherical core shell form factor is an excellent initial approximation, the third minimum gets smeared out due to the overestimated polydispersity.

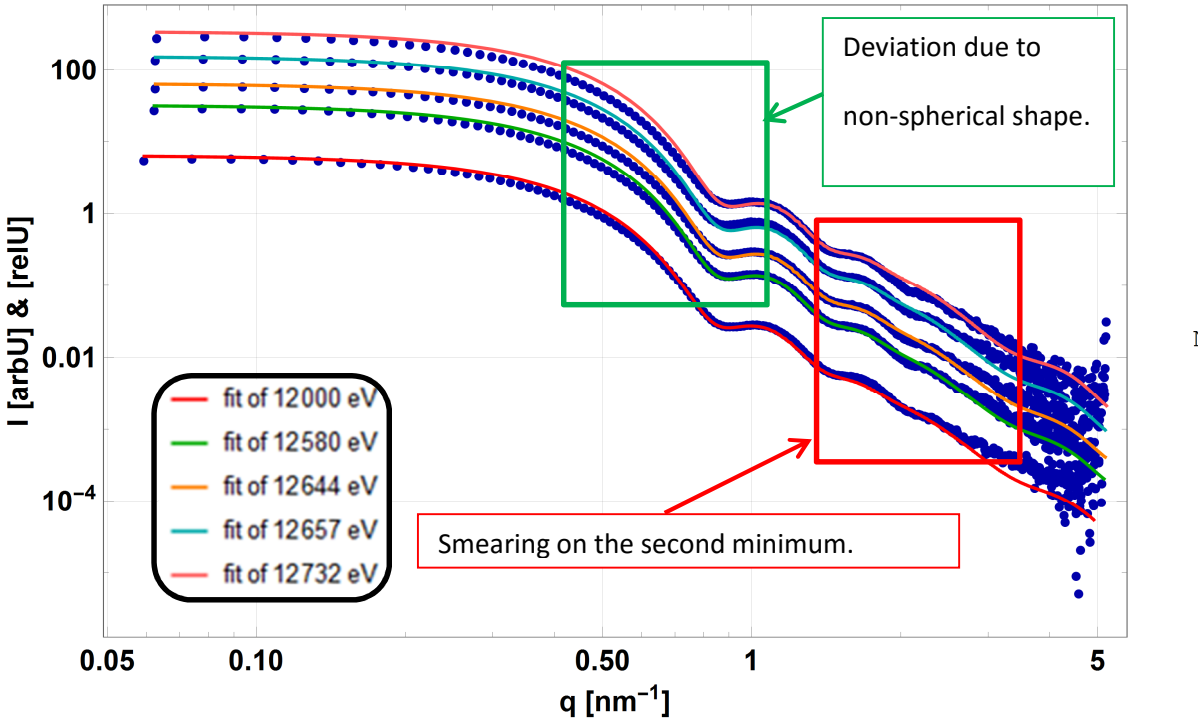

Figure 17: Fitted (lines) of the recorded spectra of the ml particle. The blue dots represent the experimental data and corresponds to the fit at the respective energies. The different scattering curves are shifted relatively to the red line by a constant factor. Smearing is already present on the second minimum, which highlighted by the red box. The deviation from the spherical form factor is highlighted by the green box.

For the **mc** series, the form factor does not seem to approximate the actual geometry as well as it was the case for the **sc** series. For instance, as depicted in Fig. 18 for the **ml** sample, the breakdown of the form factor happens more severely for lower q values, which unfortunately is true for any sample within this series. The first shoulder does not get approximated well either, which is highlighted by the green box in Fig. 18. In contrast to Fig. 17 the third minimum gets approximated worse, with the excessive smearing of the fit due to its high polydispersity. This indicates additional smearing, which could be, from a purely mathematical point of view, caused by the azimuthal averaging of a non-spherical particle. This is a quite general statement and includes many possibilities. In our case, the approximation is still quite good, which leads us to believe that the actual geometry does not deviate too far from the assumption of a sphere. This statement is further solidified by TEM images of the particles by our partners from the ETH Zurich, which will not be shown in this work. Therefore, it is justified to assume smearing due to faceting of the surface of our particles and/or a slight deviation from a spherical to an ellipsoidal shape. This seems to be also present to a lesser degree in the **sc** series, as the fit starts to deviate for the third minimum, although to a smaller degree (Fig. 17).

Nevertheless, for both, the **sc** and **mc** series, the resulting electron and Selenium density profiles are of similar quality and show the same features. A representative density profile is shown in Fig, 19 which

exhibits sharp interfaces of both densities at any of the interfaces present. Furthermore, it seems as if all the Selenium atoms remain in the core, with no interdiffusion between core and shell. The higher electron density in the core coincides with the density of Selenium atoms in the core, which corresponds to the theoretical values for CdSe. These results are in agreement with the high resolution TEM-studies performed in ref [45], in which no graded transition between core and shell has been reported. To test whether a smeared interface profile would describe the data better, the continuous form factors, described on *page 26* and onwards, were employed. A representative result of these trials will be discussed later in this chapter of this thesis in Fig. 23 on *page 48*.

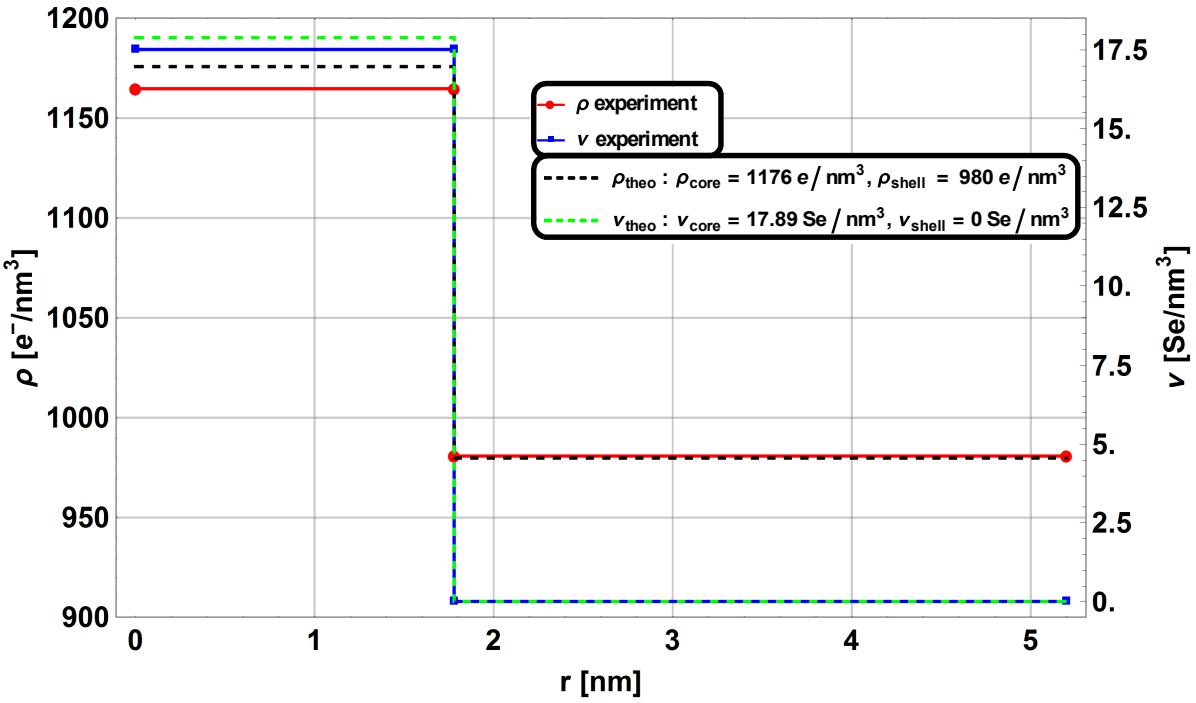

*Figure 19: The resulting values for the atomic densities of Selenium and the electron densities of the CdSe core and CdS shell versus the distance to centre of the **sl** particle. The theoretical values of the Selenium and electron density in the core and shell for a perfect step-like profile are also displayed.*

The evaluation of the **lc** series with a spherical core-shell form factor was unsuccessful. As already stated in the paragraphs above, the solutions of the preceding series' fits lie very well within the constraints on the fit parameters. This isn't the case for the **lc** series, for which even the sole usable minimum (Fig. 16) of the core could not be approximated without unreasonable large constraints in the range 20% on the polydispersity. If we regard the representative fits of the **sc** and **mc** series in Fig. 17 and 18, a slight trend in the shape regarding the size of the core is implicated. The larger the core, the more the shape seems to deviate from the simple spherical case. It is therefore plausible, that the shape of the **lc** series simply isn't approximable with a spherical form factor under the assumption of a monomodal distribution of the core radii. But one also shouldn't dismiss the less then optimal subtraction of the background due to the effects on the sample discussed in the experimental section. There still exists the

possibility, that more than one minimum would have been evaluable and therefore more information would have been extracted. The resulting fit is shown in Fig. 20.

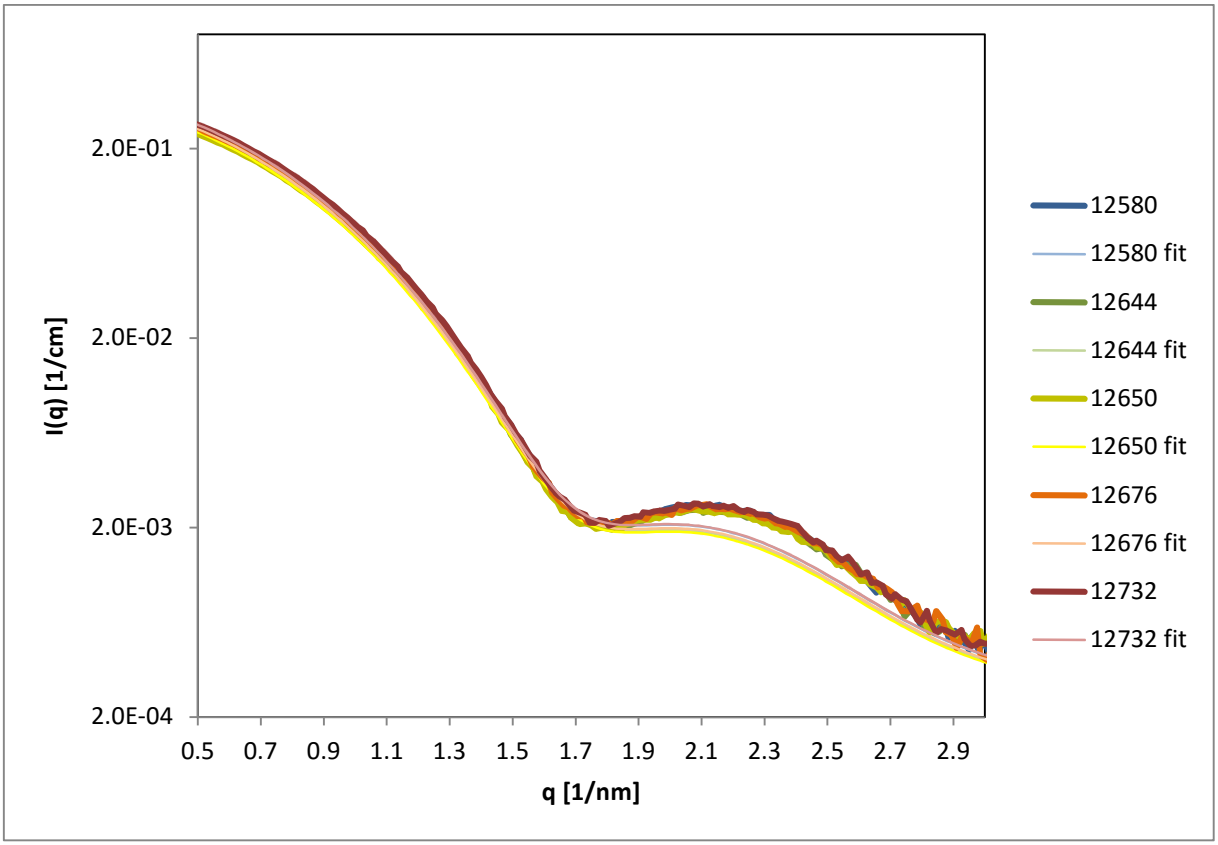

Figure 20: The fit of the recorded intensity of the sole usable minimum for the ***lc*** *particle is shown, where the significant deviation from the spectrum is observable for q-values > 1.7 nm^{-1}.*

If we now continue this analysis for all the particles of the smallest and medium core series, while keeping in mind that the largest core series did not give correct results, we didn't find any interdiffusion of notable degree. Hence, we can conclude that even at relatively elevated temperatures of ca. 310 °C no interdiffusion occurs. The resulting profiles for the Selenium concentration and the electron density are shown in Fig. 21 and Fig. 22. The theoretical values of the CdSe core and the CdS shell are retained quite well for the whole synthesis process respectively, even though the electron density seems to very for the thinnest and medium shell samples of both sereis. It was not possible to fit the annealed sample of the smallest core series, as it was presumably mixed with an unknown sample of any of the three series'. Still, there was an attempt made at separating the two different particles in the mixture via a simple spherical core-shell fit with two different particle species with the result indicating that the annealed particles of the smallest and medium core series have been mixed. This could also coincide with the synthesis process and actually seems like a reasonable result, but further evaluation, also concerning the chemical structure of the samples, was not unambiguously possible.

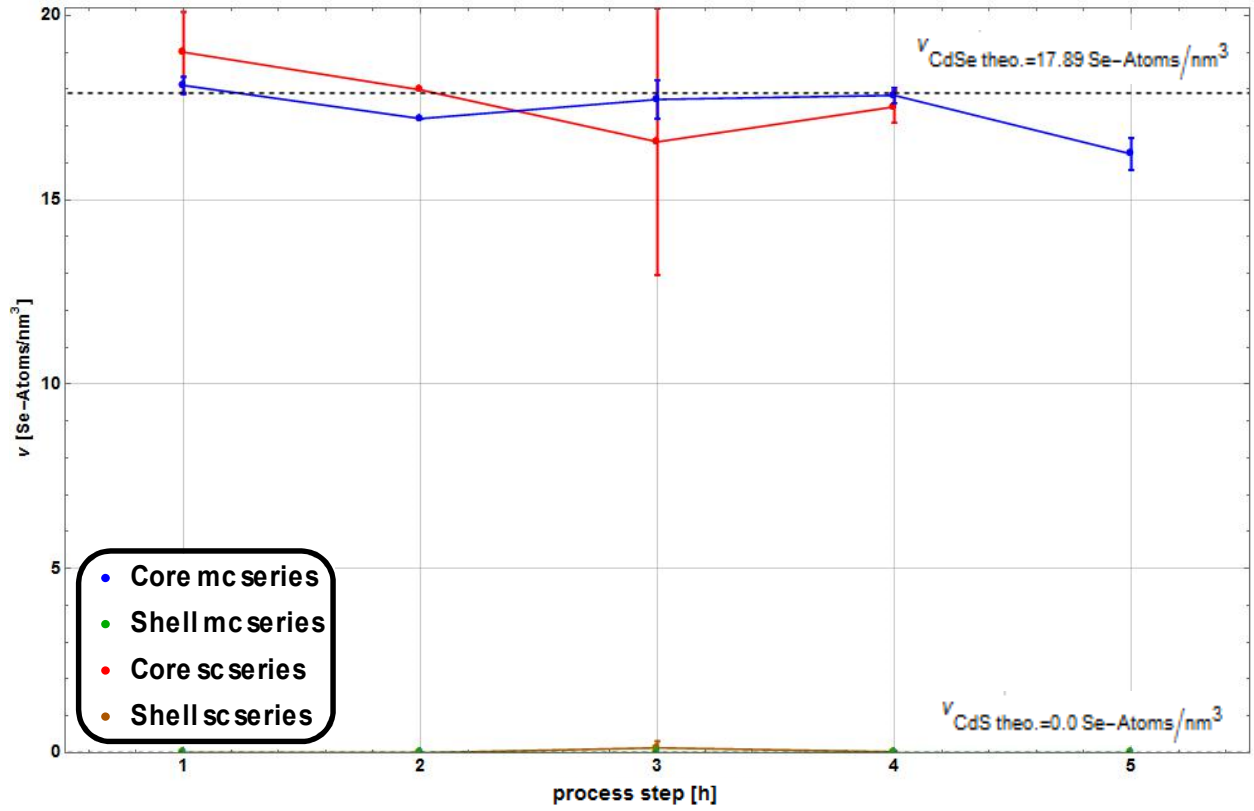

*Figure 21: The atomic density of Selenium ν is plotted for both core and shell of the **mc** and **sc** series versus the synthesis step in hours. The theoretical densities are also shown.*

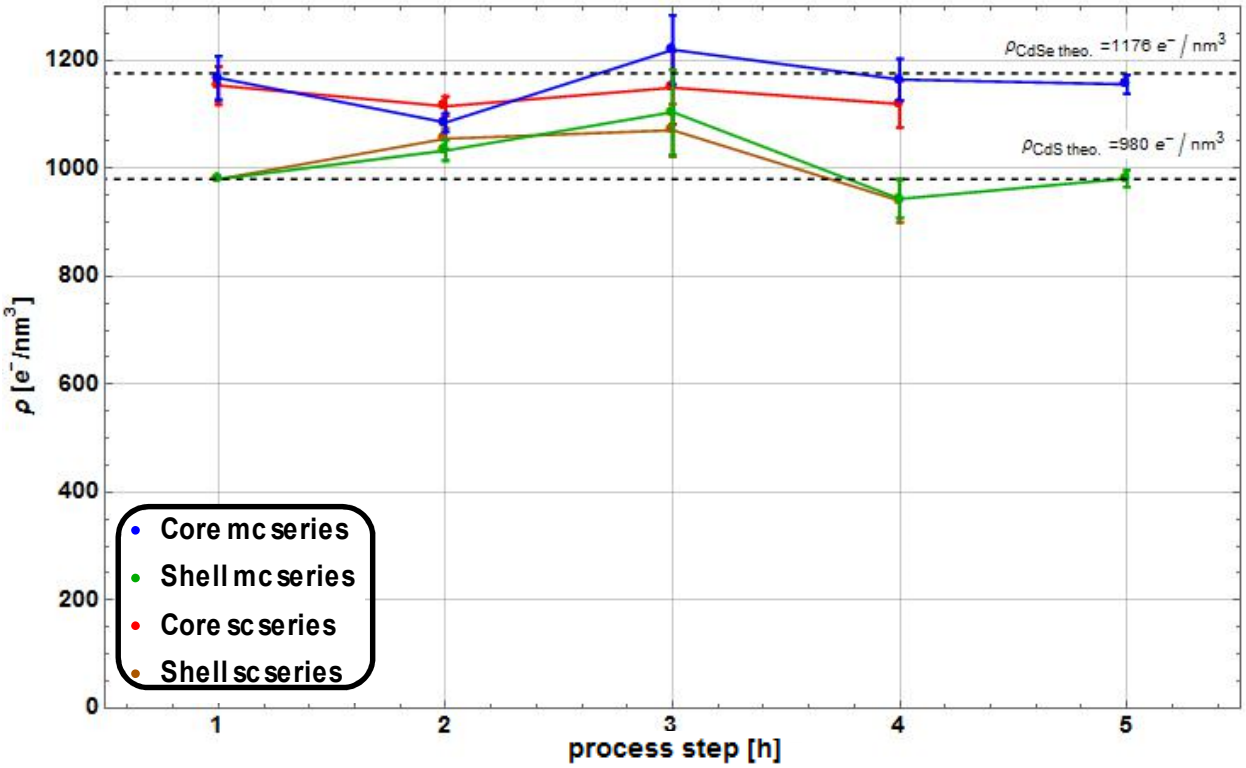

Figure 22: The calculated electron densities ρ of the core and shell for the sc and mc series versus the step in the synthesis process in hours. The theoretical electron densities of the bulk materials are also depicted.

Interestingly enough there is more variance in the fitted electron densities and a certain trend seems to be visible. The electron densities for the core are right on point with the theoretical values, whereas with increasing time in the synthesis the difference between core and shell seem to shrink, until the very largest shell right before annealing. At this step, the theoretical values are again within margin of the error bars. This would actually point to some kind of diffusion between both core and shell, which we previously have ruled out. From a mathematical point of view, these results could also be interpreted such that the Selenium concentration is not very sensitive to the initial values of the fit parameters, whereas the electron density can vary to a bigger degree. If we think back to the data analysis chapter where we stated that the total variance of the scattered intensity due to anomalous scattering was in the low percent range, this makes perfect sense. Still, to gain further understanding, we should also take the resulting sizes from the fits into account. (Fig. 23)

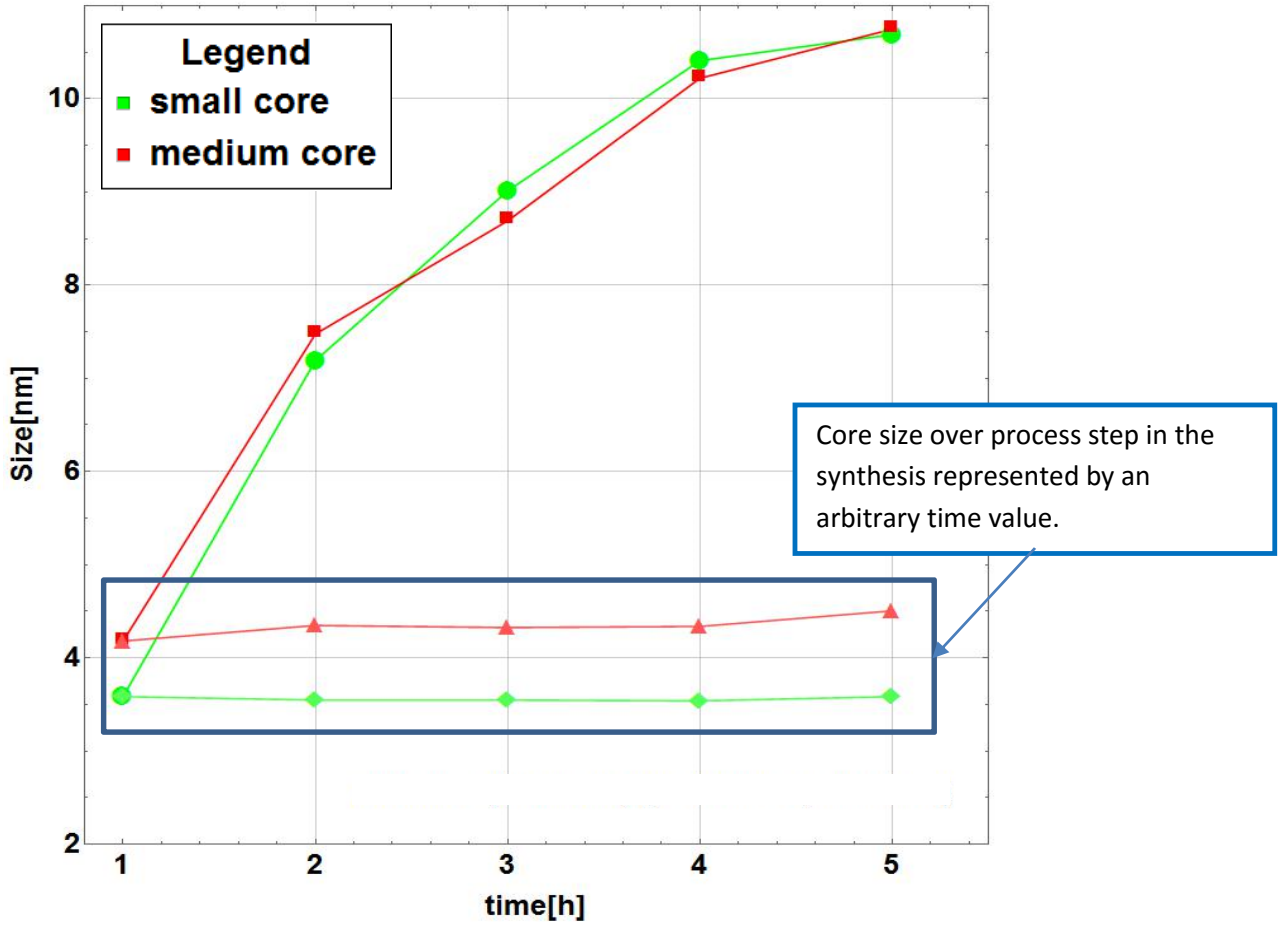

Figure 23: The total size and the core size versus the process step in the synthesis. The core sizes are highlighted by the blue box.

From Fig. 23 we learn that the smallest core particles seem to grow faster than anticipated by our chemist, yet still both series reach almost exactly the same final size. The fitted core size also seems to be largely consistent over all of the steps in synthesis, although a very minute increase in size seems to

be present after annealing. When we assume the same amount of precursors present for any core size, smaller interfaces grow faster than larger ones if the process is only limited by the speed by which new precursors are reaching the surface, but not the total amount present in the solution, or the diffusion process on the surface of the particle. To study whether or not any interdiffusion between core and shell is present, we show a representative evaluation of the annealed particle of the smallest core series. (Fig. 24) The continuous form factor used has been described on *pages 28 to 31*.

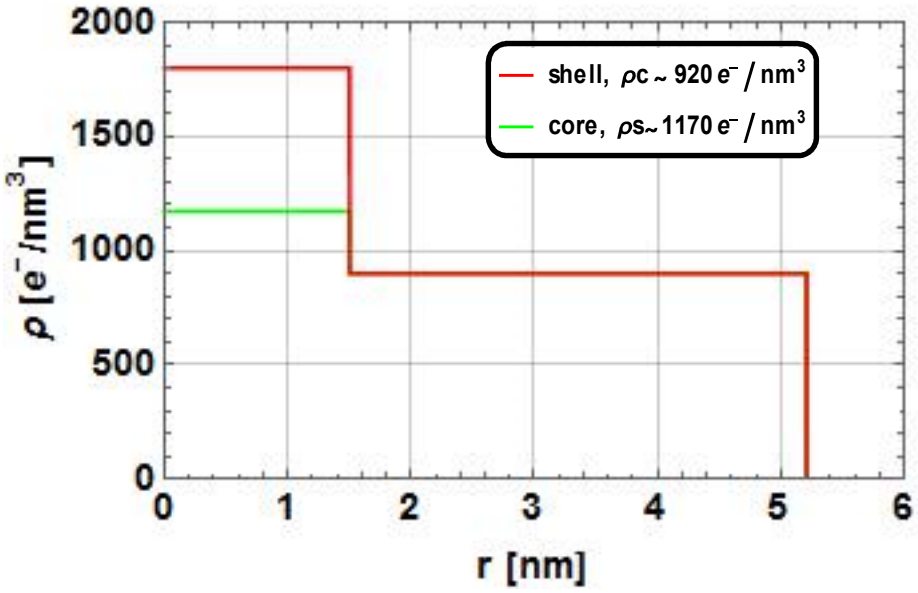

Figure 24: Here the resulting electron density versus the distance to centre from the fit with the continuous form factor from the data analysis chapter is depicted. The indicated values for core and shell hold following the colour code, meaning that until the step like transition, the green line represents the electron density within the core.

Fig. 24 shows a clear step-like transition between core and shell, with slightly lowered electron densities. The core radius comes out a bit smaller at *1.65 nm,* whereas the total particle diameter still reaches *10.4 nm.* The same step-like behaviour can be shown for any particle of the smallest and medium core series. Because of the non-spherical shape of the largest core series no fit can be achieved. Even if one would assume that the continuous nature of the electron density could smear out the fit just enough to fit a select spectrum, spherical symmetry is still implicated in *eq. 61.* Hence, even though it might be possible to fit the first minimum further minima won't show good agreement because the weight of these still does not comply with the spherical case. Therefore, this would lead to enhanced smearing via high polydispersity or nonsensically big values of the shape parameter *d* north of the limit discussed on *page 28*.

The final results of the analysis of the **sc** and **mc** via the spherical core-shell form factor are summarised in table [3].

*Table [3]: The final sizes and respective selenium and electron densities are listed for the **sc** and **mc** series.:*

	Medium Core Series					Smallest Core Series			
Series	1865	1887-1	1887-2	1887-3	1887-f	1895	1897-1	1897-2	1897-3
r core [nm]	2.09	2.174	2.16	2.169	2.25	1.79	1.77	1.77	1.769
t shell [nm]	-	1.56	2.18	2.94	3.12	-	1.82	2.73	3.43
Se core [at/nm^3]	18.10	17.00	17.80	17.82	16.24	18.99	17.99	16.57	17.52
ρcore [e/nm^3]	1167.71	1085.44	1219.73	1164.55	1155.73	1163.53	1111.49	1149.48	1119.12
ρshell [e/nm^3]	-	1033.95	1056.43	943.48	981.202	-	1049.15	1070.63	939.93

Non-spherical and semi-analytical evaluation:

For the non-spherical analysis several approaches were applied, as the fit via a simple EXCEL-program employing the spherical core-shell form factor didn't deliver useful results, as discussed in the previous section on *pages 43* and *44*. Therefore a different form factor was applied to try and fit the spectrum of the largest core series, namely an ellipsoid of revolution. Because no extreme aspect ratios were expected and the first trial run only fitted the core, the polydispersity was assumed to be the same for both the long and short axes of the particle. Furthermore, the possibility for both prolate and oblate cases were covered by the constraints put on the variables of the fit. The result was more or less satisfying, but still didn't deliver a good enough approximation as shown in Fig. 25. Even though the data was better approximated when compared to the fit shown in Fig. 20, the deviation on the second minimum is significant.

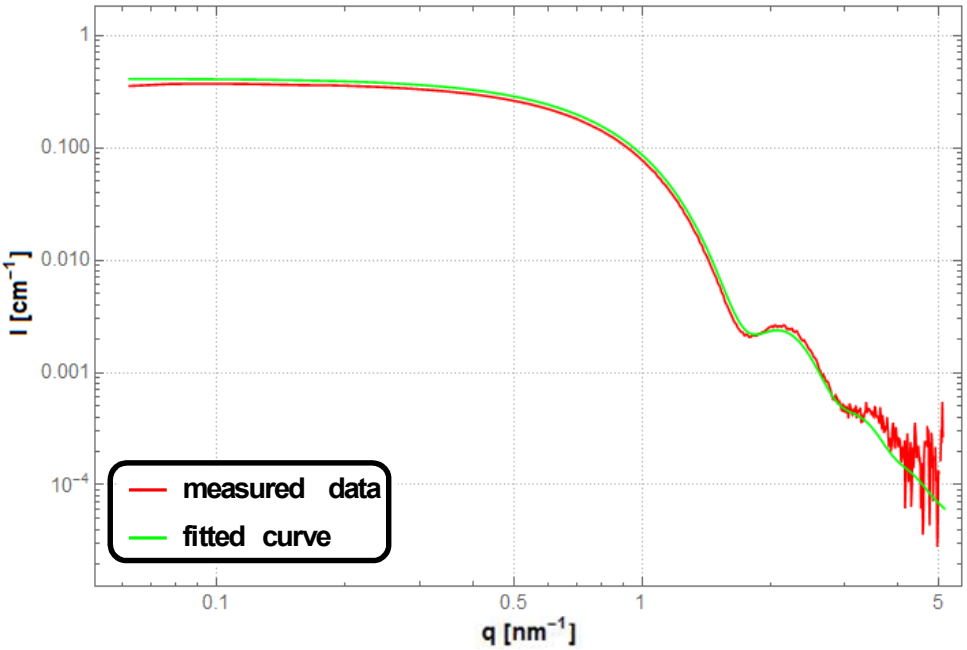

*Figure 25: The resulting fit of the recorded intensity versus q of the **lc** particle is displayed.*

Trial runs with a tri-axial ellipsoid simply took too long to be computed for core shell system, which can be related to the large number of parameters that had to be fitted. For instance, if we consider a core shell particle we need

- six parameters for the axes
- one for the density of the sample in solution
- four parameters for the electron densities and the number densities of the Selenium atoms
- one for the polydispersity under the assumption that all the axes, regardless if situated in the core or the shell, show the same behaviour

which comes out at 12 parameters for a single, simple core-shell particle. Furthermore, the repeated integration for the polar and azimuthal averaging as shown in reference [16] renders this approach hard to execute in a timely fashion. Hence, we decided to follow the route taken by Burian [32] and use ab-initio shape retrieval to determine the shape of our samples of the largest core series.

Shape retrieval by DAMMIN:

The shape retrieval of the largest core series was then subsequently carried through just as described in the data analysis section, the analysis of the data was carried through with self-written scripts in *Mathematica* based on the evaluation methods developed by Burian [32]. An example of the shape retrieved for the core is shown in Fig. 26. For better evaluation of the facets obtained from the fit we chose a convex hull mesh.

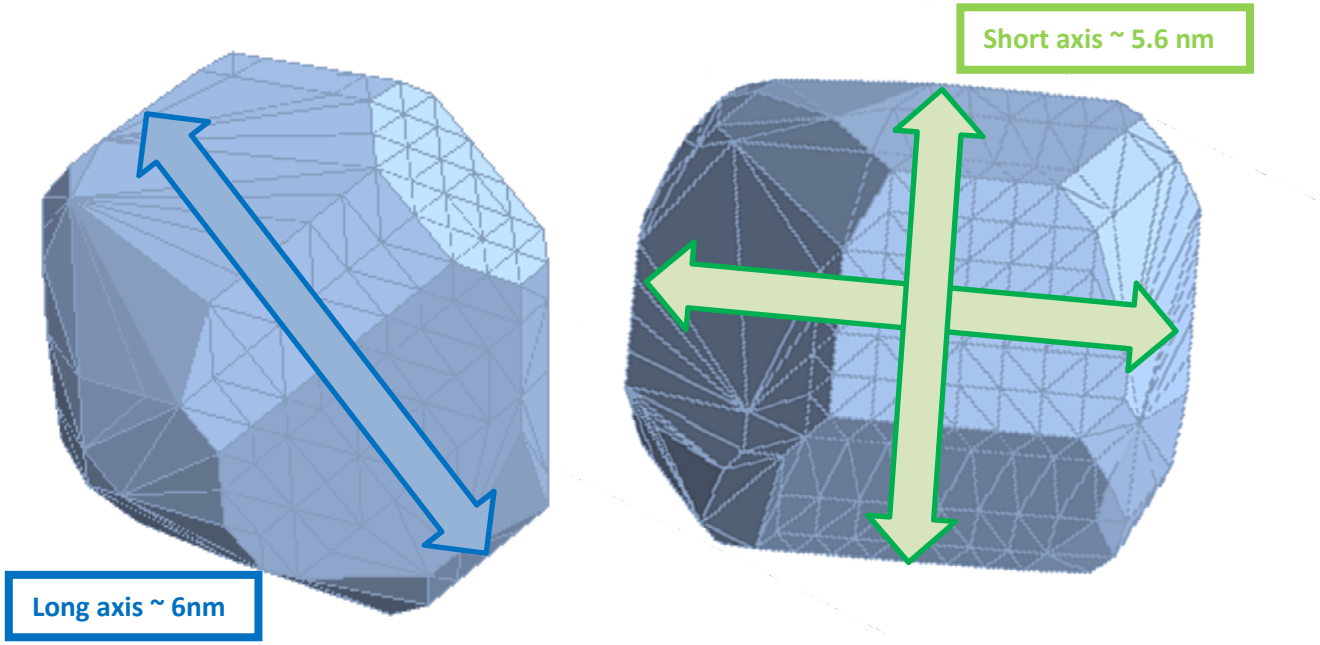

Figure 26: Various views of the convex hull mesh of the DAMMIN fit of the largest core. Even after averaging 5 distinct fits, facets are still well formed. The long and the two short axis are also highlighted.

As is clearly evident from the picture above, the particles exhibit a non-spherical shape with strong faceting and can only be approximated by an ellipsoid of revolution. As a testament to the added smearing of the curve due to the facets present, the fit with the ellpitical form factor didn't result in a dramatically decreased polydispersity below 10%, whereas DAMMIN works under the assumption of a monodisperse solution and usually cannot reproduce the crystal shape well for polydispersities above single digit values [32]. On the upside, the facets of the crystals are well defined, which in turn means that the smearing is very possibly due to the faceting and not to high polydispersity. Still, a description of such heavily facetted particles is not always easy, especially if we look at the results obtained from the linear evaluation method by Burian for the **lc** particle. (Fig. 27)

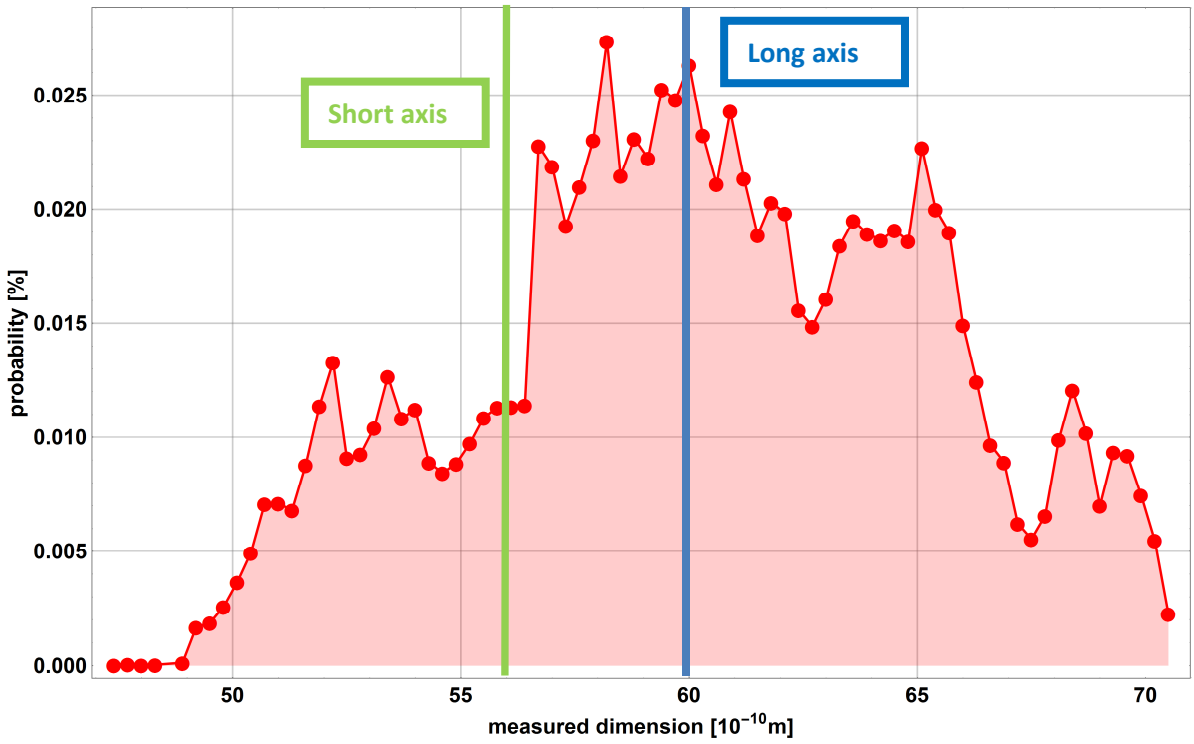

Figure 27: The value plotted on the x-axis is the distance between two dummy atoms on the particle surface, with the measure taking through the centre of the particle, versus the probability of this value occurring for two dummy atoms on the particle surface. As can easily be seen, a simple distinction of the half-axis is not easy and not as simple as is the case in Ref [32]. The green bar marks the shorter axis, the blue bar the longer axis.

The shape of the curve in Fig. 27 is roughly divided into two plateaus with many small minima within them, which may represent single facets for which the probability to measure the distance dead centre is smaller than for area elements outside. This highly simplified picture is not fully applicable, as the facets' normal vector at its centre doesn't necessarily run through the middle of the particle, but the general idea seems reasonable enough to be expanded on.

Following Burian, the half axis of an ellipsoid of revolution can be determined by taking the largest and smallest distances found. The particles here represent an extension to the tri-axial case, away from the ellipsoid of revolution, which complicates the picture. Additionally, the results obtained should be checked by visual evaluation, which was also implemented and allows a first look at the structure. The maximum half-axis came out at around 6 *nm*, which is far off the maximum values present in the histogram. This is a testament to the strong faceting and deviation from the ideal elliptic shape with the three main axis perpendicular to each other. But this results in the possibility to coincide the measurements with the facets via the visual evaluation and reconstruct the crystal in that way.

While fitting the data, we ran into an additional problem concerning the shapes, as the results obtained from DAMMIN weren't fully consistent especially for the medium shell sample of the largest core series. In this case two shapes were retrieved that didn't even yield similar aspect ratios, as one could be approximated by a prolate ellipsoid, while the other covered the oblate case. This could be related to the small amount of Shannon channels of ca. 7.2, which is far below the value recommended by Burian, of at least 10, and by Svergun (see [32] and the reference therein) for core-shell systems. This could potentially not only influence the shape retrieved, but also the occupancy values in regard to the differentiation between core and shell, as this parameter should essentially represent the electron density [32]. The resulting two competing shapes are depicted in Fig. 28.

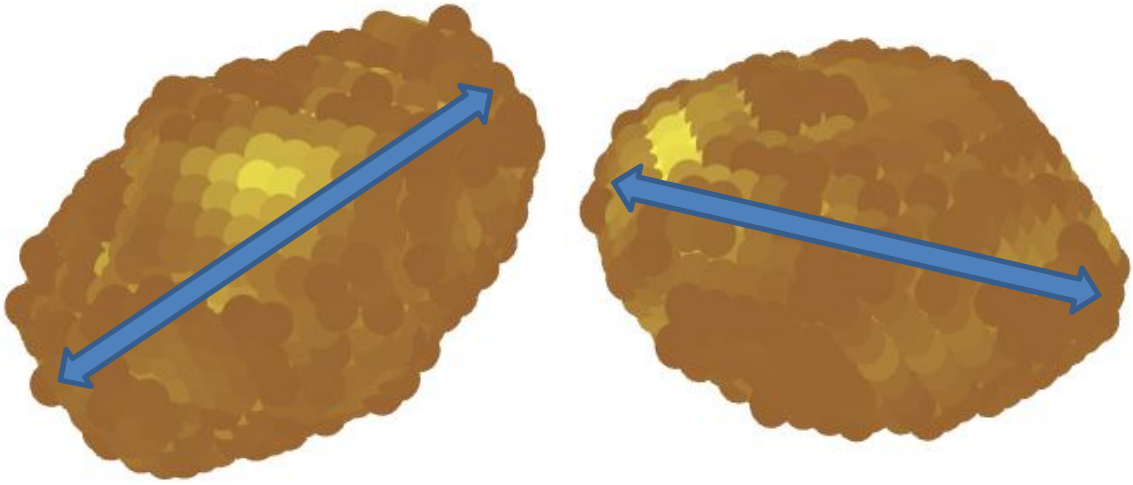

Figure 28: On the left the prolate case of the results is pictured, on the right the other solution. Both particles result in the same SAXS spectrum.

Although both solutions in Fig. 28 represent a prolate particle, the resulting size and aspect ratio renders the left solution unphysical with a long axis of about 16 nm. The resulting sizes, obtained from the fit, were calculated to represent the radius of a sphere with equivalent volume. Table [4] shows the sizes, the resulting aspect ratio and the radius of the sphere with equivalent volume obtained from the DAMMIN fits.

Table [4]: Size and aspect ratio of the largest core series' DAMMIN fits.

Particle	short axis [nm]	long axis [nm]	aspect ratio	equ. radius [nm]
lc	5.6	6	1.07	5.54
ls	6.9	8.5	1.23	7.39
lm	9.5	11.2	1.2	10.05
lt	7.7	13.4	1.74	9.31
la	9.12	14.3	1.56	10.54

The **lt** particle exhibits a very large aspect ratio and a rather small equivalent radius. This is most probably due to the fit not delivering the correct result. This reasoning is undermined by the fact, that the volume of the particle seems to get smaller with increasing growing time when compared to the **lm** particle. Additional reasons, why this result cannot represent the actual physical mean particle of this sample will be discussed in the *WAXS* part of this chapter. The sizes are now all depicted with the sizes of the smallest and medium core series in Fig. 29.

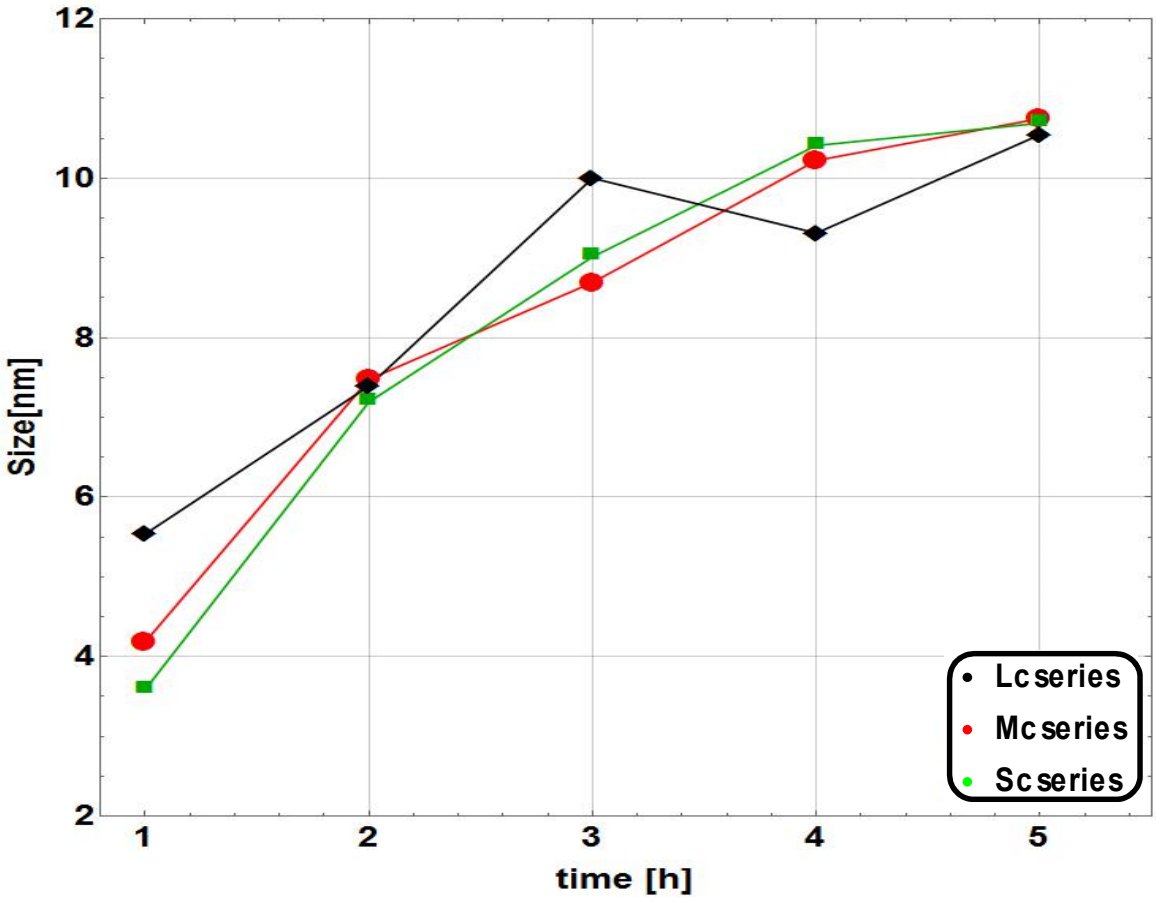

Figure 29: The sizes of all three series are plotted against the time of extraction from the synthesis.

Interestingly enough, even though the three series start from a different core size they all ultimately reach the same final size, with the thickest shell of the largest core particle looking to be an outlier. Generally, the overall quality of the fits and the unambiguity of the structures obtained increases with the amount of Shannon channel.

WAXS:

After subtraction of the recorded backgrounds, the resulting curves used for analysis are shown in the following Fig. 30-32:

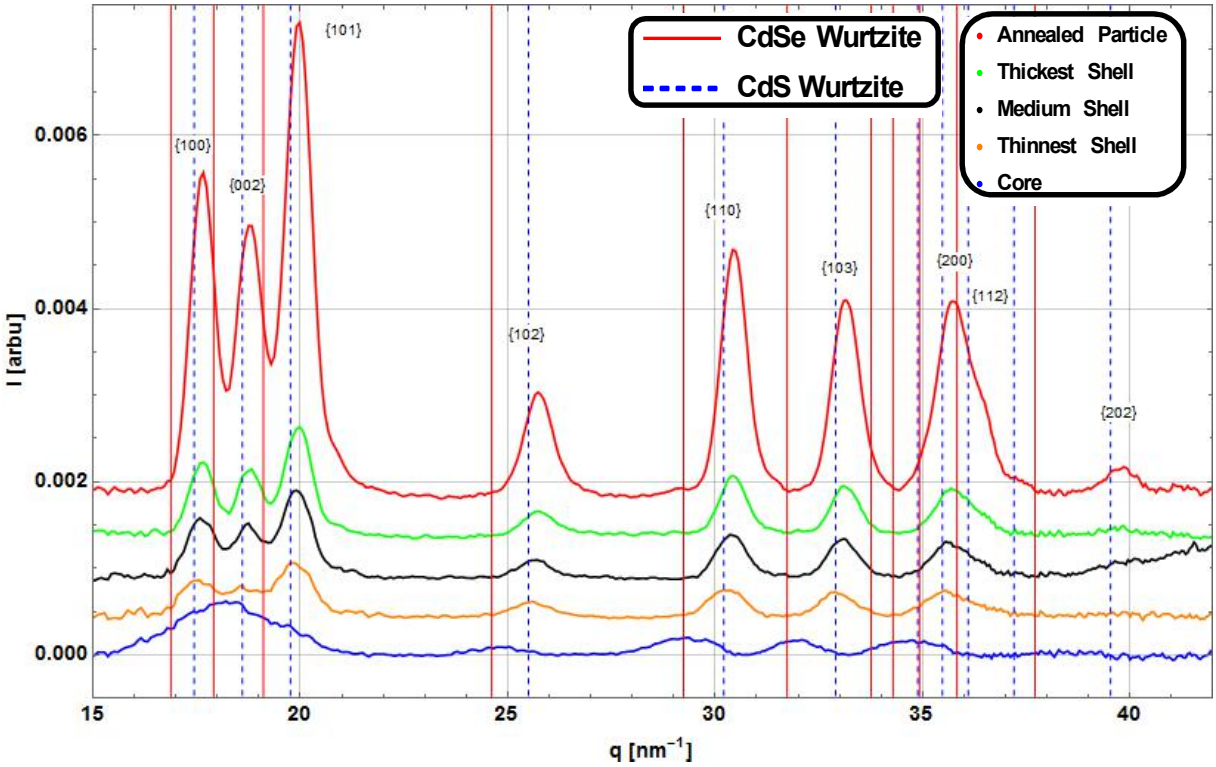

Figure 30: The diffracted intensity I is plotted versus the scattering vector. The WAXS spectra of the ***sc*** *series shifted relative to each other by a constant factor. The Wurtzite Bragg positions for bulk CdSe and CdS are also shown.*

From the **st** sample on it is clearly visible that the Bragg peak positions coincide with the CdS-Wurtzite positions even for the thinnest shell particle. The scattering of the core is therefore probably negligible for the **sc** series. The Bragg position of the NCs with a thick shell shift to larger q-values with increasing shell thickness. This implicates uniform compressive strain in the particles, with details concerning shifts of singular peaks left to more detailed analysis beyond the scope of this work.

But also the **mc** series exhibits CdS Wurtzite structure from the thinnest shell sample on (Fig. 31), whereas the **lc** series' Bragg positions only align with the CdS Wurtzite positions from the medium shell sample and onwards (Fig. 32).

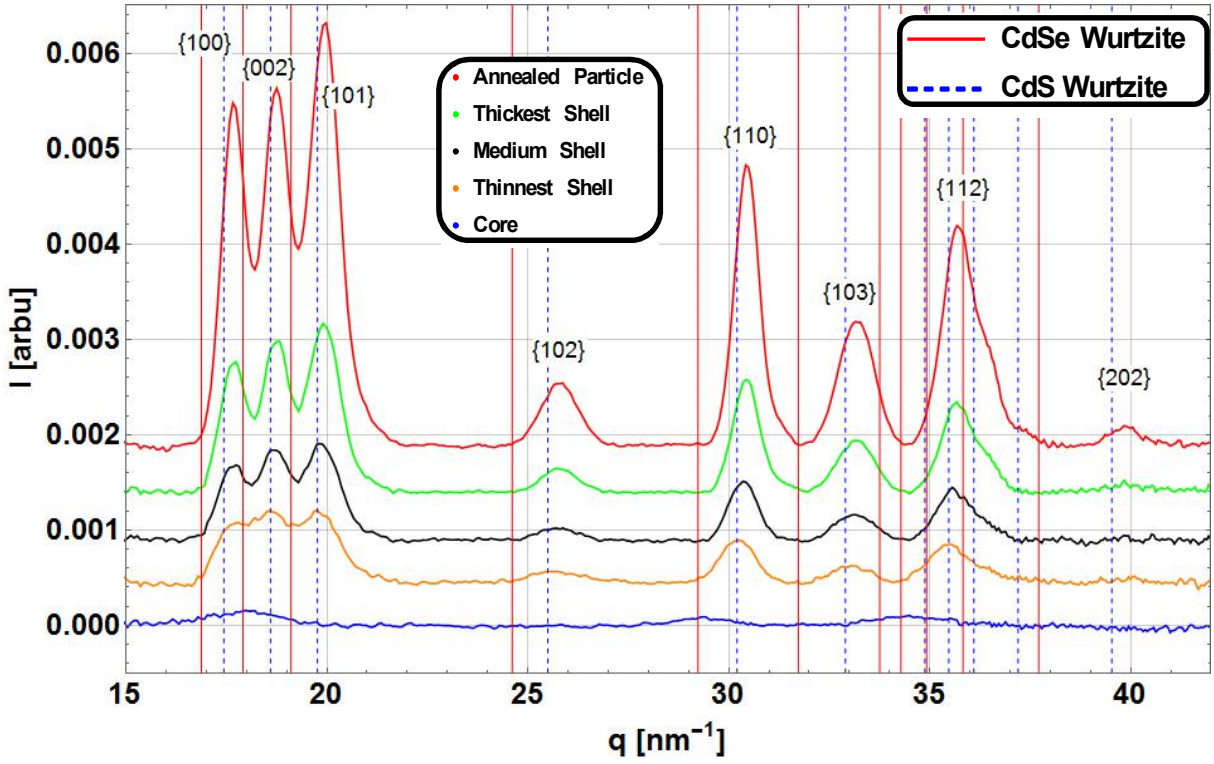

*Figure 31: The recorded intensity of the **mc** series is plotted versus the angular value in q. The Wurtzite Bragg positions for bulk CdSe and CdS are also shown. The data was again shifted relative to each other.*

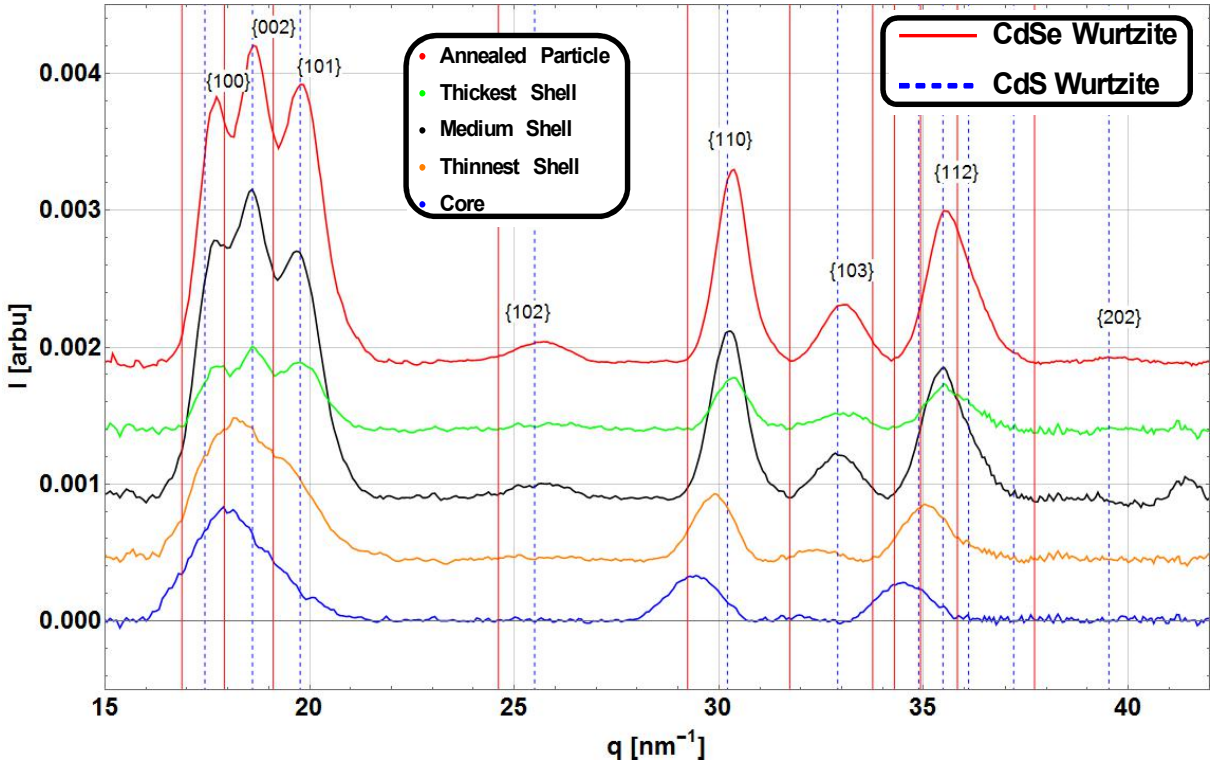

*Figure 32: The recorded intensity of the **lc** series is plotted versus q an shifted relatively to each other by a constant value. The Wurtzite Bragg positions both for bulk CdSe and CdS are also shown.*

The resulting curves implicate some very interesting features and some obvious variance in the crystal structure of the 3 different series. The change in peak heights in the larger core series implicates a change on the crystalline level. To shed some light on the changes being observed here, we simulated the particles of the three series, using *PCG SWAXS*, with the structural data obtained from the ASAXS data. For the smallest core series, everything seems quite well behaved as depicted in Fig. 33.

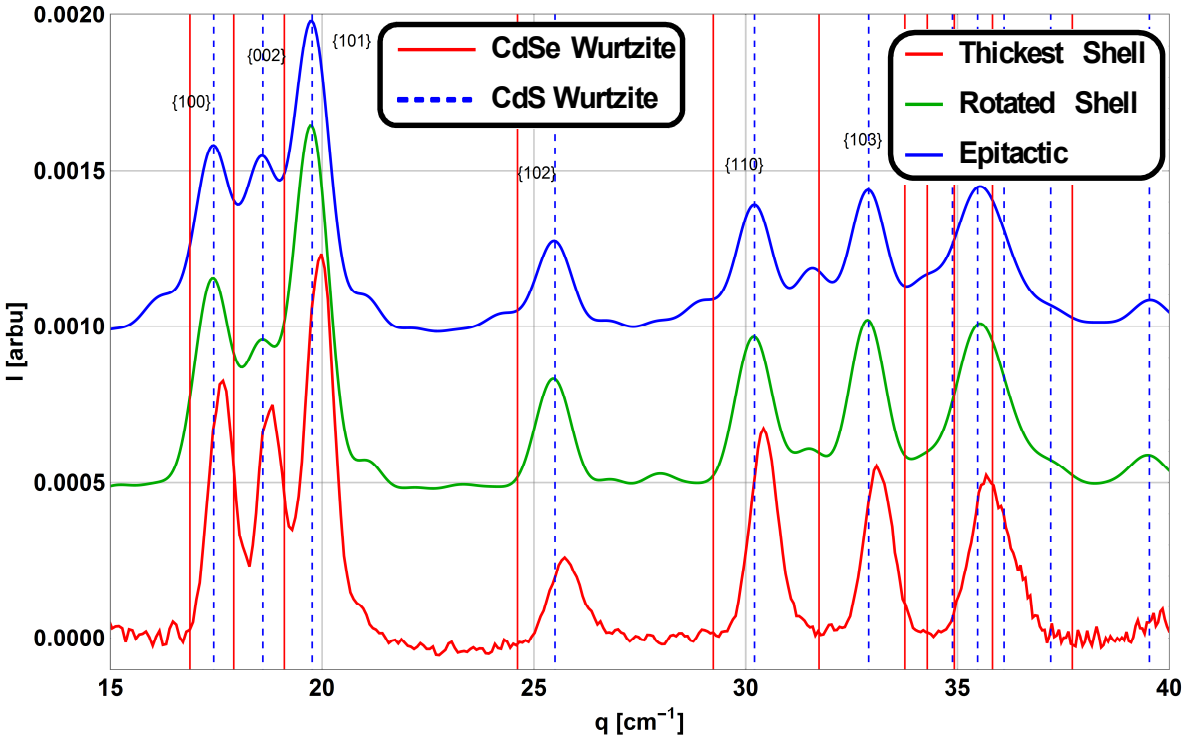

Figure 33: The actual WAXS pattern of the ***st*** *particle is depicted with two simulated patterns. The recorded pattern is drawn red, green and blue depict simulated data by PCG SWAXS. To guide the eye, also the Bragg positions of both, CdSe and CdS in Wurtzite structure, are plotted.*

From Fig. 33 we can learn several important facts about the particles, as these effects seem to be visible for every single sample from our experiments. First, the NCs seem to be homogeneously compressively strained, as the peaks are all shifted to the right regardless of the Bragg peak observed. Second, as the simulated patterns, which represent epitactic and topotactic realisations of the same core shell system, in fig. 33 show, it is not possible to differentiate both. The green curve, which shows qualitatively similar peaks, is obtained via the simulation of a particle with a, in respect to the core, relatively tilted shell. The blue curve was calculated with an epitactic relationship between core and shell. There is no simple indication of a strict epitaxial or topotactical relationship between core and shell, which further necessitates the application of HRTEM techniques to determine structural features as such mentioned before. Interestingly enough, it does not seem to matter which way the shell is being turned in relation to the core, as the difference between configurations are very minor. Third, as being seen by the position of the simulated peaks with respect to the depicted positions of the ideal bulk CdSe and CdS Wurtzite structure, the total size of the simulated system doesn't cause any shift in the peak and falls directly on

the CdS bulk positions. Additionally, it can be seen that the scattering of the core seems to be negligible, which is explained later in this work via the phase percentage of the core and shell. Unfortunately, if we take a closer look, the heights of the peaks relative to each other still don't quite match the simulation, a fact that might implicate a partial phase change from Wurtzite to Zincblende in the crystals. To explain this further, we take a look at simulated data from Zincblende and Wurtzite crystals in Fig. 34:

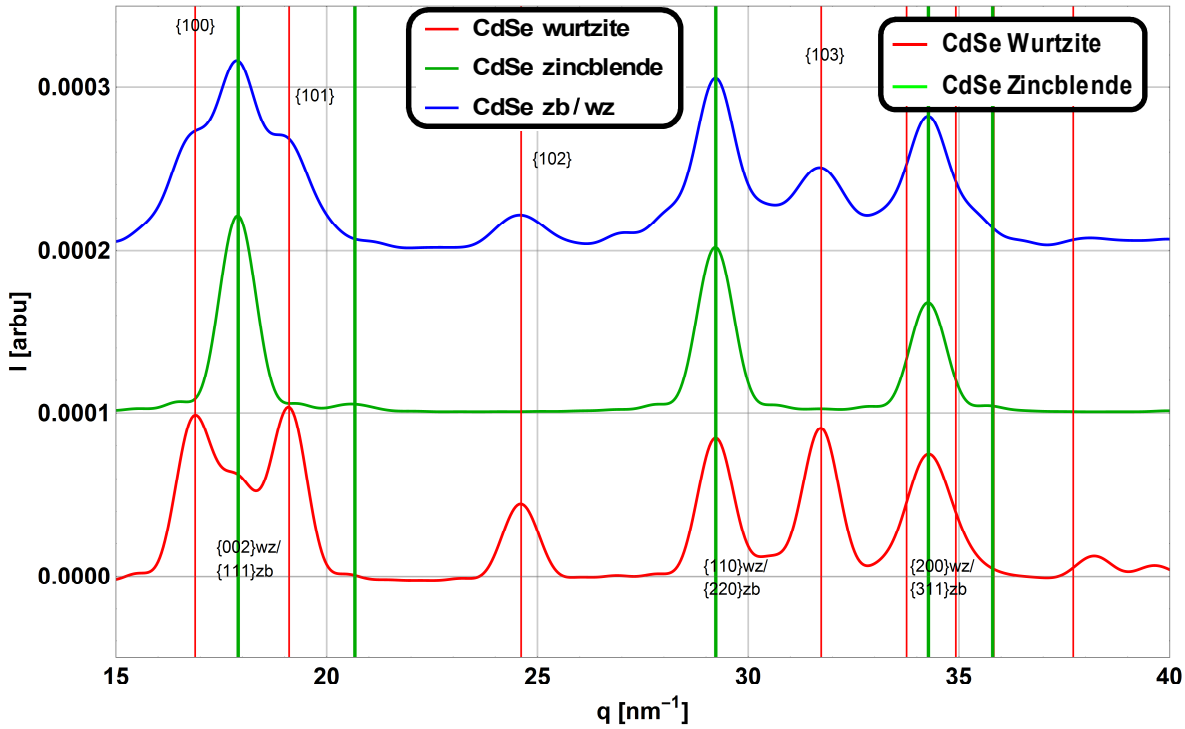

Figure 34: The intensity I is plotted against the scattering vector q, with the curves shifted relative to each other by a constant factor. The particles simulated are purely CdSe, the sizes used for these simulations are corresponding to the ***mc*** *series, except for the pure Wurtzite phase, to exaggerate the effects of phase-mixture. The general trends match the data shown here.*

Fig. 34 shows some important evidence when evaluating the peaks from all three series. The {111} peak of the Zincblende structure coincides with the {002} peak from the Wurtzite structure, which make sense if we remember that these are the most densely packed layers in these materials. The same argument holds for all the other coinciding peaks and delivers important input for the following analysis, regardless of the chemical structure in our case.

As the peaks growing relative to their neighbours are the {002}, {110} and the {112} Wurtzite planes, who coincide positionally with the {111}, {220} and {311} Zincblende planes respectively, it seems as if a growing amount of Zincblende is present in the particles with growing core size. Concerning this transformation, it has been reported that uncapped CdS nanocrystals switch from the Wurtzite to the Zincblende structure without external influence [46], albeit faster under pressures conditions far away from the standard conditions defined by the International Union of Pure and Applied Chemistry

(IUPAC) [47]. A somewhat different and speculative way for this transformation to occur could also be due to the presence of stacking faults. If two intrinsic faults are next to each other within the distance of a plane, this essentially forms an extrinsic stacking fault, which in turn corresponds to a {111} plane of a Zincblende structure. The presence of a small fraction of Zincblende could potentially lower the energy barrier that needs to be overcome for the transition between these two structures to occur in the whole particle via martensitic transition [9]. This model seems also probable from a materials science point of view, as the stacking fault energy of CdSe and CdS in their Wurtzite configuration is very low (~10 mJ/m² [48]), lower than silver with ca. 20 mJ/m² [59], which already is stated as a low-stacking fault energy material. As with lower stacking fault energy the ease of generation of such growth fault increases, one can easily imagine that the energy expenditure for two faults could be "repaid", even if the difference in energy between Zincblende and Wurtzite is only 0.3 meV per atom [46].

The evaluation of the predicted phase fractions concerning the core and the shell are shown in Fig. 35, of which essentially only the large core series shows any interesting contribution to the total scattering of the particles.

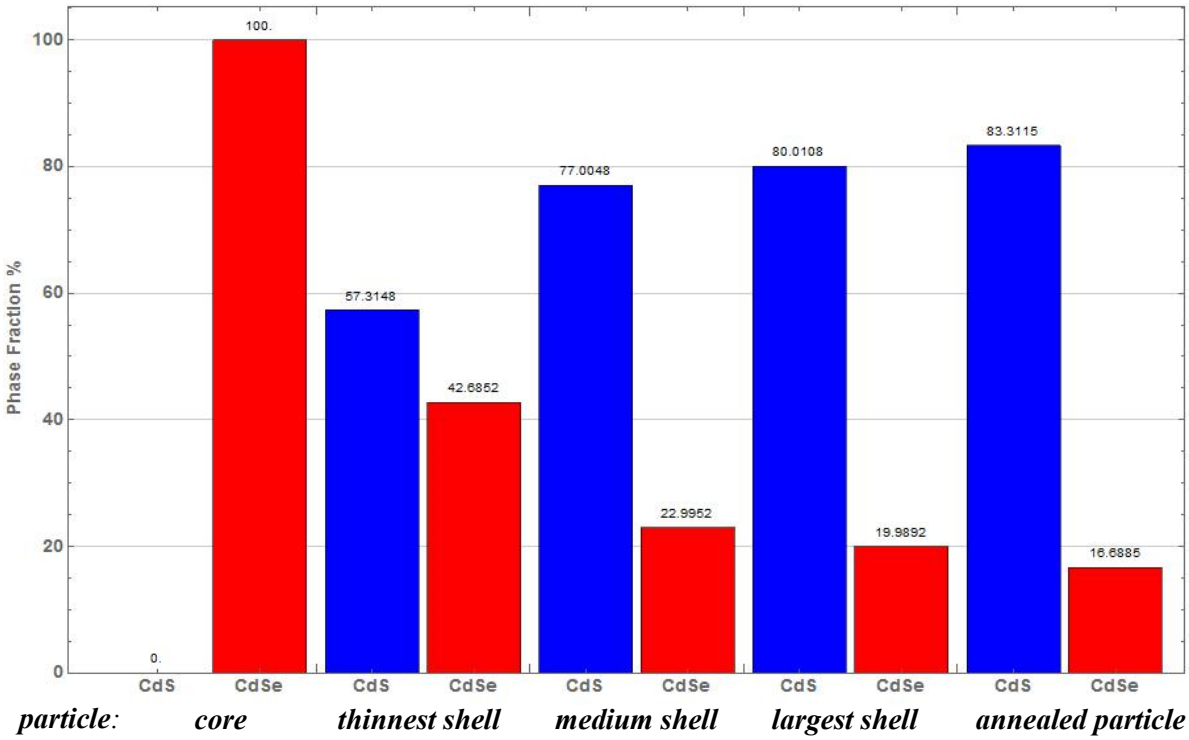

Figure 35: The relative scattering contributions for the ***lc*** *series are shown versus the step in the synthesis process. The volume fraction of the CdS and CdSe phase calculated by the radii and shell thicknesses is obtained by the fits from the SAXS data.*

Because the scattering contribution of the core is quite high for the **lc** series, the peaks are relatively shifted to the CdSe Wurtzite positions as observed earlier in Fig. 32. In turn, this means that the WAXS spectra of the **sc** and **mc** series are dominated by the CdS Wurtzite shell. This explains the position of

the thinnest shell on the largest core particles, as the predicted phase fraction of CdSe, under the naïve assumption of spherical symmetry, lies somewhere between the bulk positions of the pure material. But again, the Zincblende peak seems to dominate, thus a higher phase fraction of said structure is expected.

The evaluation of the full widths at half maximum (FWHM) was done via fitting of a Gaussian and under an assumed instrumental profile of the same shape. Following the integral breadth methods discussed on *page 9* and *10*, this allows for an easy decomposition of the peak into an instrumental contribution and the pure scattering of the crystal plane. This was achieved by applying *equation 17*, although the influence was, as described in data analysis section, negligibly small. If we now plot the FWHMs over the actual peak position, we can gain the following "map" and conduct a Williamson-Hall analysis. The following Fig. 36 show the analysis done for the thickest shell particle of the smallest core series. The FWHMs of the Bragg peaks were used to calculate the size for the corresponding set of {hkl} planes via *eq. 15* with the value of K set at 0.94. This leads to a systematic error, which's extent should be small enough for such a "quick and dirty" analysis with the limited set of peaks available.

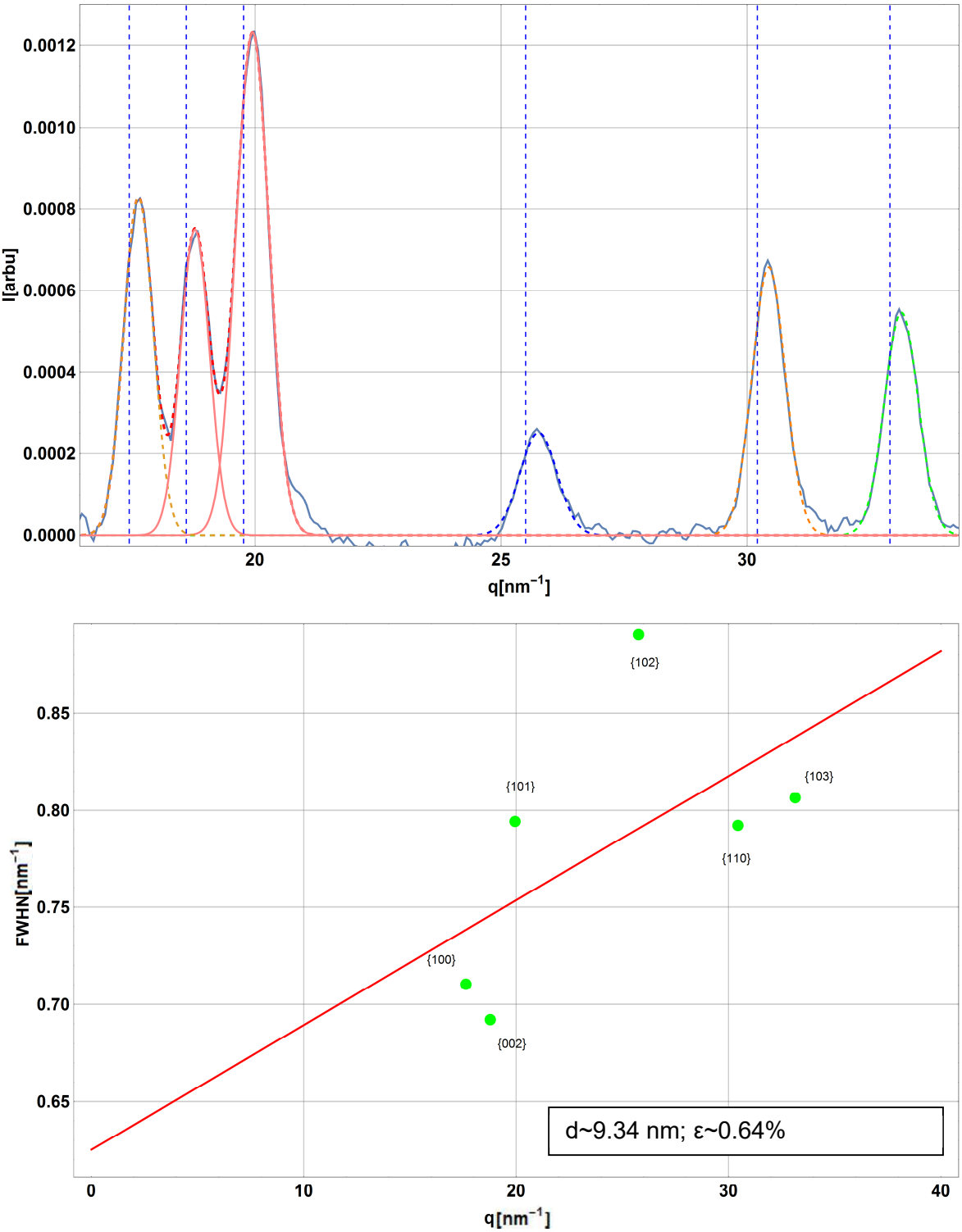

Figure 36: In the plot above, a fit of the Bragg peaks of the thickest shell sample of the ***sc*** *series with Gaussians is shown. The fitted FWHM's are then used to determine the strain and mean size of the sample in the lower plot by the Williamson-Hall method via plotting the FWHMs versus the q-values of the Bragg reflections.*

As can be seen above, the resulting widths don't lie on a straight line. Because especially the planes {101} and {102} seem to be substantially broader than the neighbouring peaks {002} and {110}, the fitted regression line yields a steeper slope. This results in a decreased estimated size of the particle at 9.34 nm, which is about one nm smaller when compared to the SAXS size of ca. 10.4 nm. Generally,

one can assume that this relates to a smaller crystalline size, with amorphous areas that reduce the measured scattered length. If we conduct this kind of evaluation for every sample and compare these sizes to the SAXS diameters, we obtain Fig. 37:

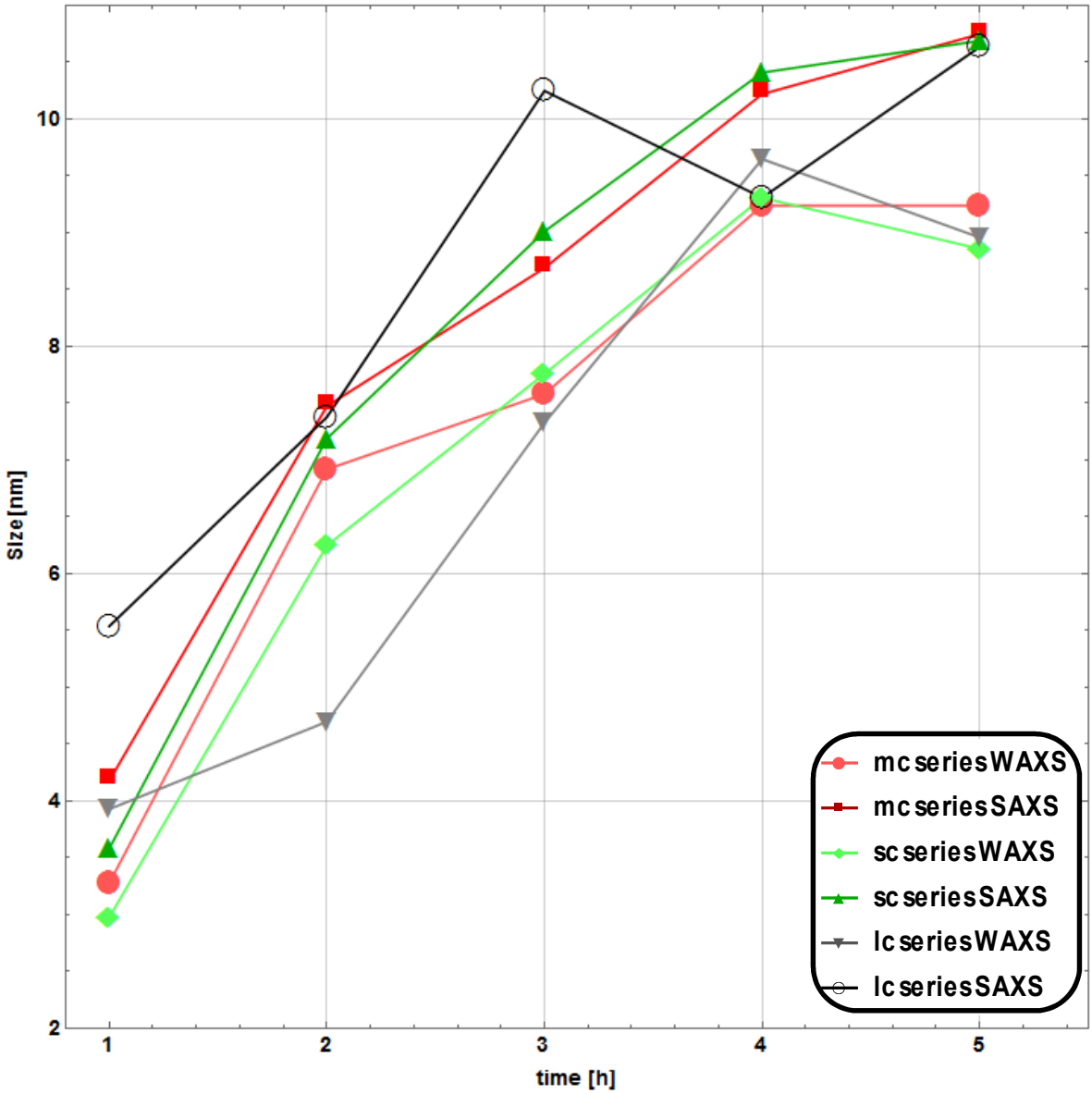

Figure 37: The sizes obtained from the SAXS and WAXS data are shown, versus the synthesis step reduced in an arbitrary point in time in hours. These correspond to the samples in the series, as outlined in table on page.

Obviously the sizes in Fig. 37 from both scattering regimes seem to follow the same trend, with the sizes of WAXS being considerably but consistently smaller. It is also evident, that the DAMMIN fit for the **ll** sample is of low quality, with the domain size for WAXS being bigger than the radius of equivalent volume (as discussed on page 53). Aside this exception, the only true difference can be observed for the annealed particles of all three series. If we compare the size from the WAXS data to the diameter obtained from the SAXS data of the **lc** and **sc** series, for which the diameter increases

slightly upon annealing, the crystallites seem to shrink. This can be interpreted as a roughening or restructuring of the particles surface, hence a decrease in the crystaline scattering volume in the particle. The **mc** series WAXS data doesn't seem to follow this trend as explicitly, but the increase in size from the **ml** to the **ma** sample is evidently not as pronounced as for the diameter from the SAXS data. For a more complete picture, we look at the FWHMs of all the series respectively plotted together. (Fig. 38 - 40)

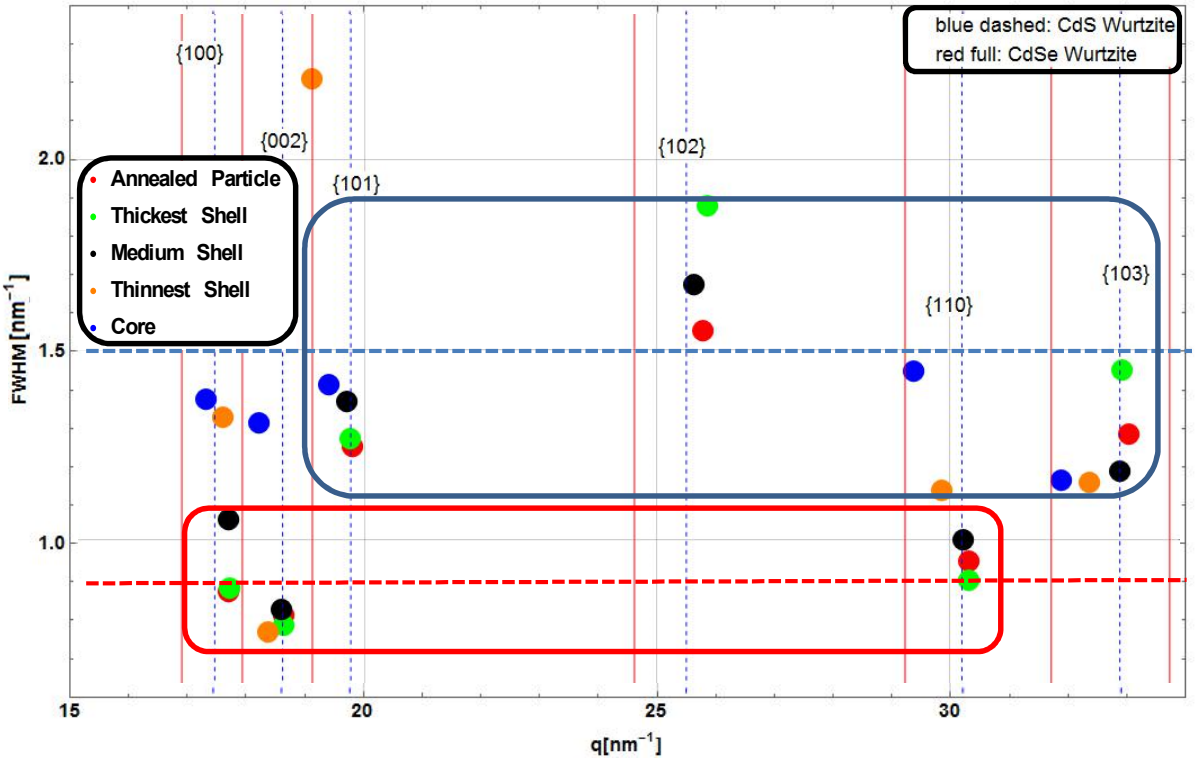

*Figure 38: The FWHMs of all the samples Bragg peaks of the **lc** series are plotted against their position in q-space. The red and blue lines indicate the mean width of the boxed values, which can be used to calculate the aspect ratio from the values in the respectively coloured boxes.*

At this point, we should shortly discuss the effect of the volume fraction on the positions of the peaks observed. Fig. 38 shows some apparently strange behaviour of the peak positions for the Bragg reflexes especially of the {103} peak. But if we think back to the results in Fig. 32, it is obvious that the Wurtzite peaks coinciding with the Zincblende structure on {002} and {110}, as earlier discussed on *page 57*, are clearly more pronounced. The "pure" Wurtzite structure peaks {102} and {103} are very small, which can be explained by a dominant phase fraction of Zincblende structure in the cores. But upon formation and subsequent growth of the CdS shell, these positions increase in recorded intensity, implying a growing amount of Wurtzite phase in our particles. Still, in the end, the {102} and {103} peaks exhibit significantly higher values for the FWHMs, meaning a smaller scattering domain size, which aligns nicely with the lower recorded intensity of these peaks when compared to their direct neighbours.

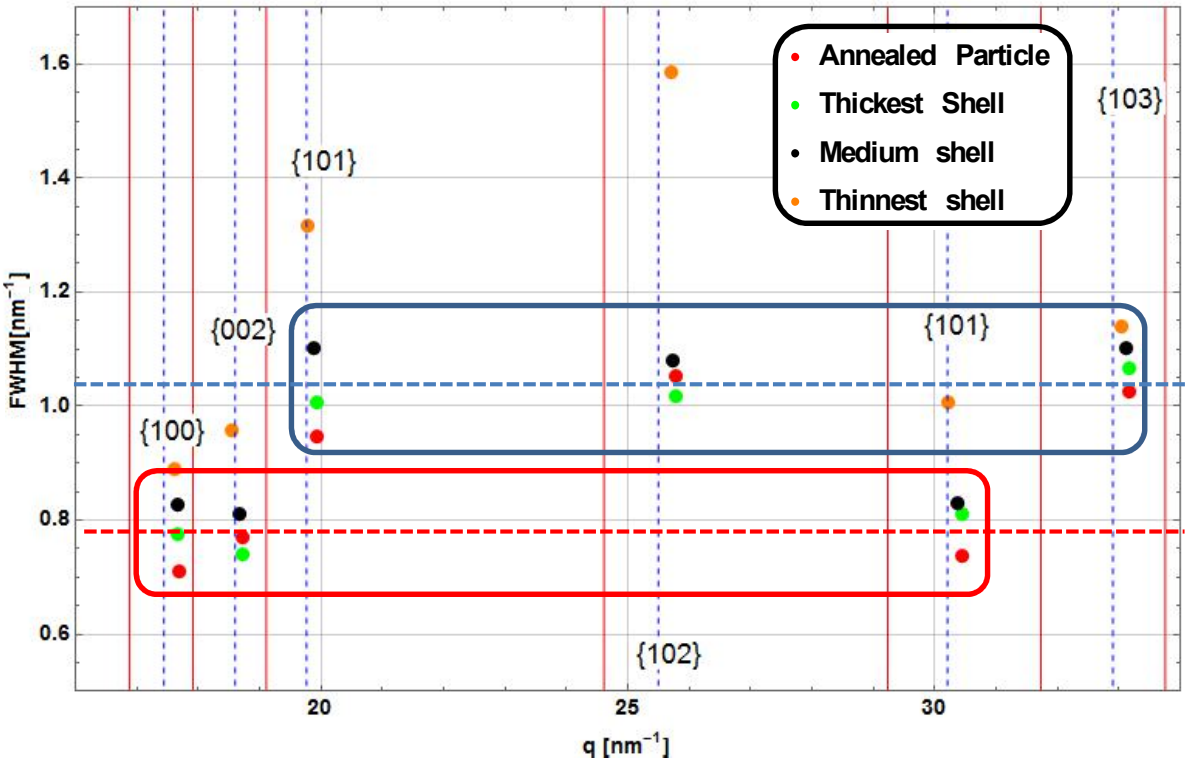

*Figure 39: This figure shows a map of the FWHMs of all Bragg peaks versus their position in q-space of the **mc** series. As in the **lc** series, the medium core series also shows small anisotropy in shape, hence indicated by the blue and red dashed lines. The core is not shown, because the signal to noise ratio was*

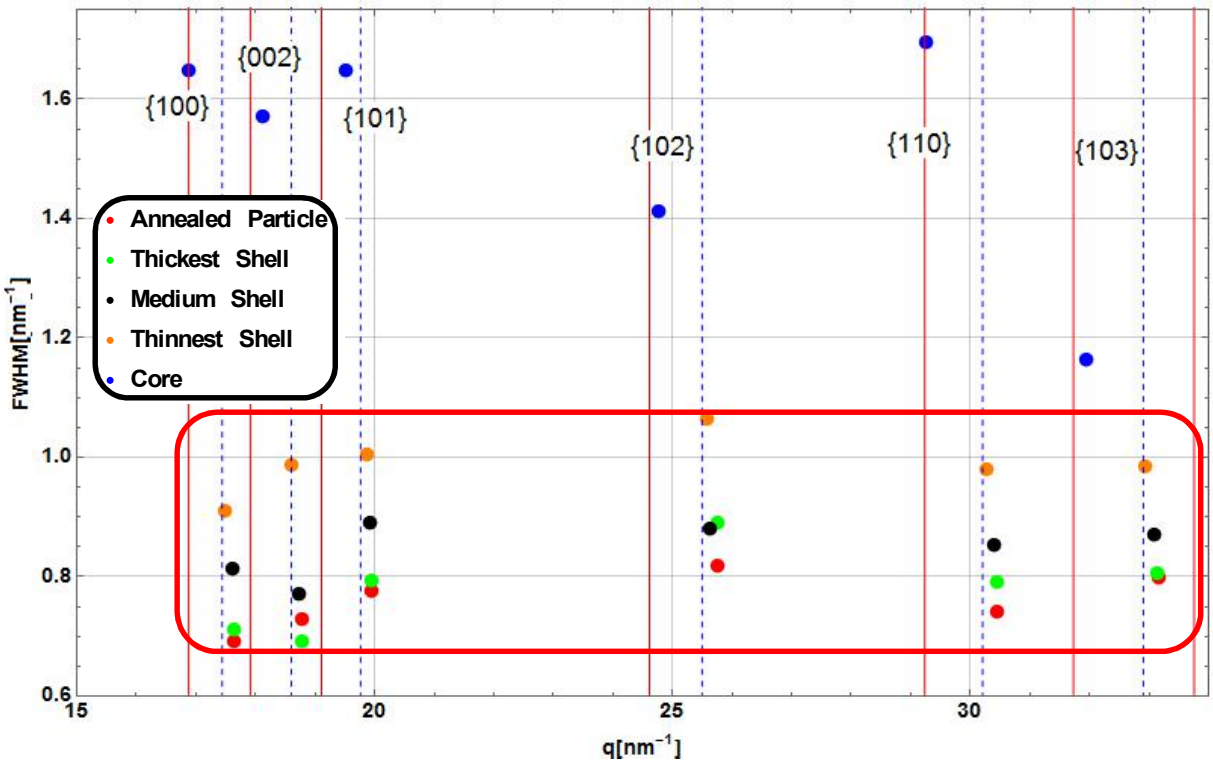

*Figure 40: The FWHMs of the Bragg positions from the **sc** series are plotted against their positions in Q-space. The red box highlights very similar FWHM values.*

From these maps several things can be extracted, aside the discussion on Fig. 38 above. It can be clearly seen especially from the {110} and {103} positions of the peaks that, according with the predicted scattering contribution of the core, the peaks shift from the CdSe Wurtzite to the CdS Wurtzite position. Therefore, in contrast to the medium and smallest core series, the dots of the largest core series seem to be jumbled, but a general trend in the FWHMs is still visible. The growing difference in peak widths with increasing time between "angled" planes with a non-zero value for the l-value in the Miller indices, and "perpendicular" planes with the l-value being zero. Namely, the angled planes are the {101}, {102} and the {103} planes, the perpendicular planes are denoted by {100}, {002} and {110}. These are grouped by a blue and red box respectively to further exaggerate the difference. Now we use the mean FWHM values of the perpendicular and the angled planes, indicated by the red and blue line respectively, to calculate at an aspect ratio between these two with *eq. 15*. This comes out as

$$\frac{1.5}{0.95} \sim 1.6$$

This value corresponds very well with the value obtained for the **la** particle by SAXS. If we do the same for the medium core series, we have

$$\frac{1.05}{0.8} \sim 1.3$$

For the sc series, no such analysis is necessary, as the particles are of high spherical symmetry. This fact can be again seen in the total breadth of interval of the FWHMs in Fig. 40. For the respective step in synthesis, the values are very close to each other, hence again implying a spherical shape.

As stated in the SAXS part of the analysis, we assumed that with increasing core size the shape will deteriorate from the spherical case, as the largest core series seems to exhibit a more elliptical shape. An aspect ratio of 1.3125 seems too big of a contrast between the smallest core series and the medium core series with only 2-3 monolayers size difference between the cores, which will be discussed further on. If we remember *eq. 20* from the introduction, the broadening seems to target angled planes which incidentally seem to fit the formula more or less well. As can be seen in Fig. 40, the FWHMs, in this case belonging to the **sl** sample, are split into the aforementioned angled and perpendicular planes. These two sets of values are now being fit separately under the light of the traditional Williamson-Hall method to calculate the particle size. The results are depicted in the following Fig. 41.

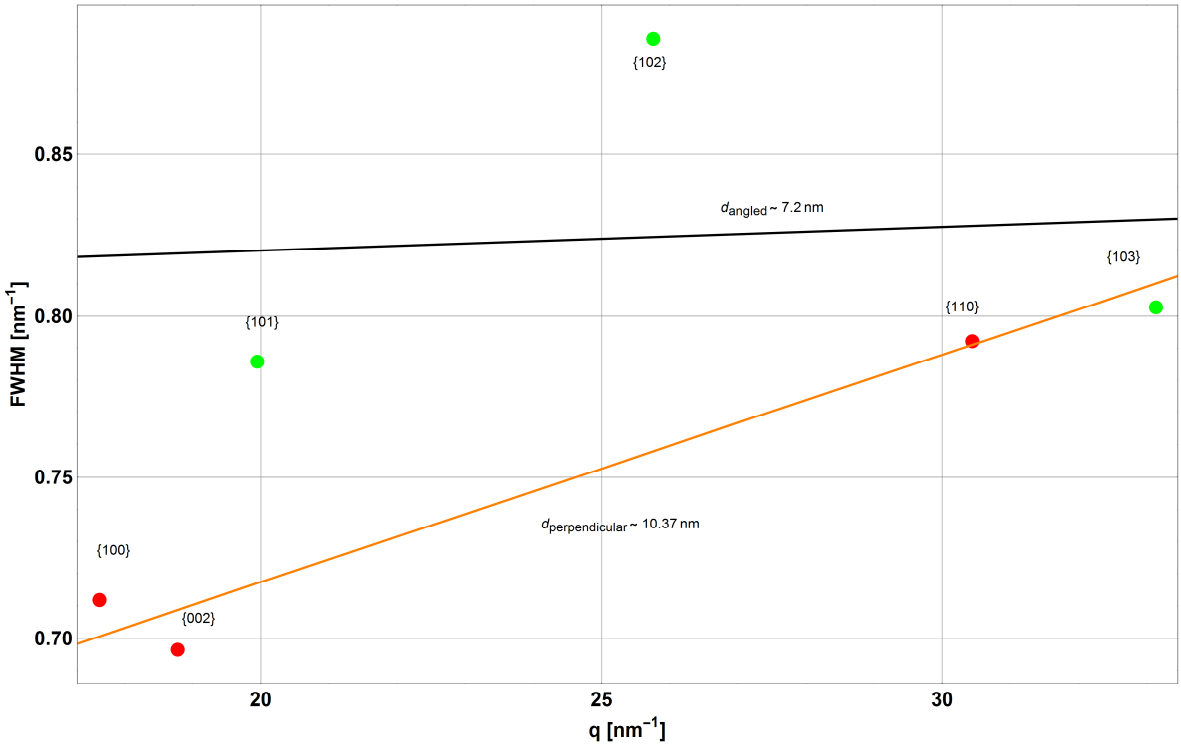

*Figure 41: The Williamson-Hall plot of the **sl** sample, hence the FWHMs versus the q-values of the Bragg reflections are shown. The perpendicular and angled planes are being evaluated separately, with the red dots belonging to the perpendicular and the green dots to the angled planes respectively.*

Fig. 41 clearly shows that some kind of peak broadening seems to be present, which, as discussed above on *page 66*, might be related to intrinsic stacking faults. The calculated diameter of 10.37 *nm* is very close to the SAXS value of ca. 10.4 *nm* for the **sl** sample if we disregard the angled planes. The result from angled planes deviates severely. This evaluation has been conducted on the **sl**, **sm** and **st** samples, dismissing the mixed **sa** sample. The results are summed up in table [5].

Table [5]: WAXS vs SAXS sizes, without the annealed particle and the core with no "angles" planes considered for analysis.

	WAXS size [nm]	SAXS size [nm]	WAXS/SAXS [%]
Thickest Shell	10.37	10.4	99.7
Medium Shell	8.45	9.013	93.8
Thinnest Shell	6.71	7.19	93.3

But as plane {103} doesn't seem to exhibit big broadening, also different mechanisms such as twin faulting should be investigated as this doesn't fully fit the prediction by *eq. 20*. Twinning is unfortunately

quite difficult to determine and usually needs high quality data of at least three orders of one broadened plane to separate strain, size and faulting broadening of the crystals under investigation without using too many assumptions [49]. The used work-around in the analysis so far only applies to broadening due to faulting. Additionally, the medium and largest core series don't allow for such an analysis due to the non-spherical shape and the resulting splitting of the widths into angled and perpendicular planes. A legitimate objection to the proposed analysis poses the possibility that the other series might too exhibit more extensive broadening due to twinning and stacking faults and therefor might not exhibit an elliptic shape at all. At least for the largest core series, the shapes obtained from the shape retrieval clearly show severely non-spherical and facetted particles, such as in Fig. 26 & 28. Hence, even though the aspect ratio of the medium core series in the WAXS regime is quite high at 1.3 and might be overestimated, not all of it should be related to broadening due to faulting. In the case of the largest core particles, it is quite unrealistic to have the big difference in peak widths solely due to broadening. The biggest difference between two widths in the **sc** series is roughly 0.2 nm^{-1} between the {002} and {102} plane for the annealed particle (Fig. 40). In contrast, the difference between the same planes for the **la** sample comes out at ca. 1.2 nm (Fig. 38). As these particles have around the same diameter, which can be readily seen in Fig. 37 the faulting should be similar. It is therefore highly unlikely that the broadening of the angled planes of the **lc** series is purely due to stacking faults.

Summary and Outlook

This work has revealed multiple interesting features of the CdSe/CdS core-shell nanocrystals produced via the hot injection method as described in [5]. These results include:

1. existence of a sharp interface between core and shell with no Selenium present in the Shell
2. increasing aspect ratio and faceting with increasing diameter
3. stacking faults and/or twinning within the particles
4. mixture of Wurtzite and Zincblende for particles with a core radius of at least 2.0 nm
5. a roughening of the surface and subsequent decrease of the crystalline domain through annealing of the particles

Interestingly, the core size seems to largely determine the phase fractions between CdS in Wurtzite and Zincblende configuration of the shell. Whether this is due to a larger amount of stacking faults in the core, hence a larger phase fraction of CdSe Zincblende present, or to the increasing elliptical symmetry of larger cores is not yet determined. It isn't even clear if the partial phase change of a particle is directly related to the shape of the particle, as the dynamics of growth of nanocrystals is yet not understood well enough to clearly distinguish between phase change while or after growth. Aside from the effects of the shape of the NCs, it is evident from the combined knowledge from the ASAXS and the WAXS data to conclude a pronounced roughening of the particle surface upon annealing. As this roughening is probably the cause of many trap states, it is highly questionable whether the quantum yield improves, through heat treatment.

To gain this information, several techniques were adapted to

- fit diffuse interfaces
- estimate the background of wide angle scattering data
- estimate the aspect ratio of particles without any needed previous information
- perform fits by a modified form factor for ellipsoids of revolution, based on an approximation via series expansion

There is not a lot work done on evaluating dislocation densities, stacking faults and their influence on performance and other qualities such as phase fractions. But these parameters might be key to design nanocrystals in the future with a broader range of tailored properties. For instance, by choosing or optimising synthesis parameters of materials to arrive at higher stacking fault energies, it could be possible to limit the amount of stacking faults and dislocations and therefore minimize trap states which decrease performance. Also, with the phase change mechanism proposed above, the chance of synthesising particles with fractions of two phases, one unwanted, could be limited to small and therefor negligible amounts from the perspective of performance. But it is still not really easy to gain information

on these parameters, which necessitates the development of faster and more reliable methods. This is why one could expand on the evaluation by Burian [32] and bridge the difference in parameters obtained from SAXS to WAXS. For example, as stated in the DAMMIN-analysis section of this work, the valleys of the graph from the linear evaluation could be related to the facets of a convex particle, which can be done if one also tracks the direction of the cylinder stuck through the centre of the crystal and relate it to the size measured from it. (Fig. 42)

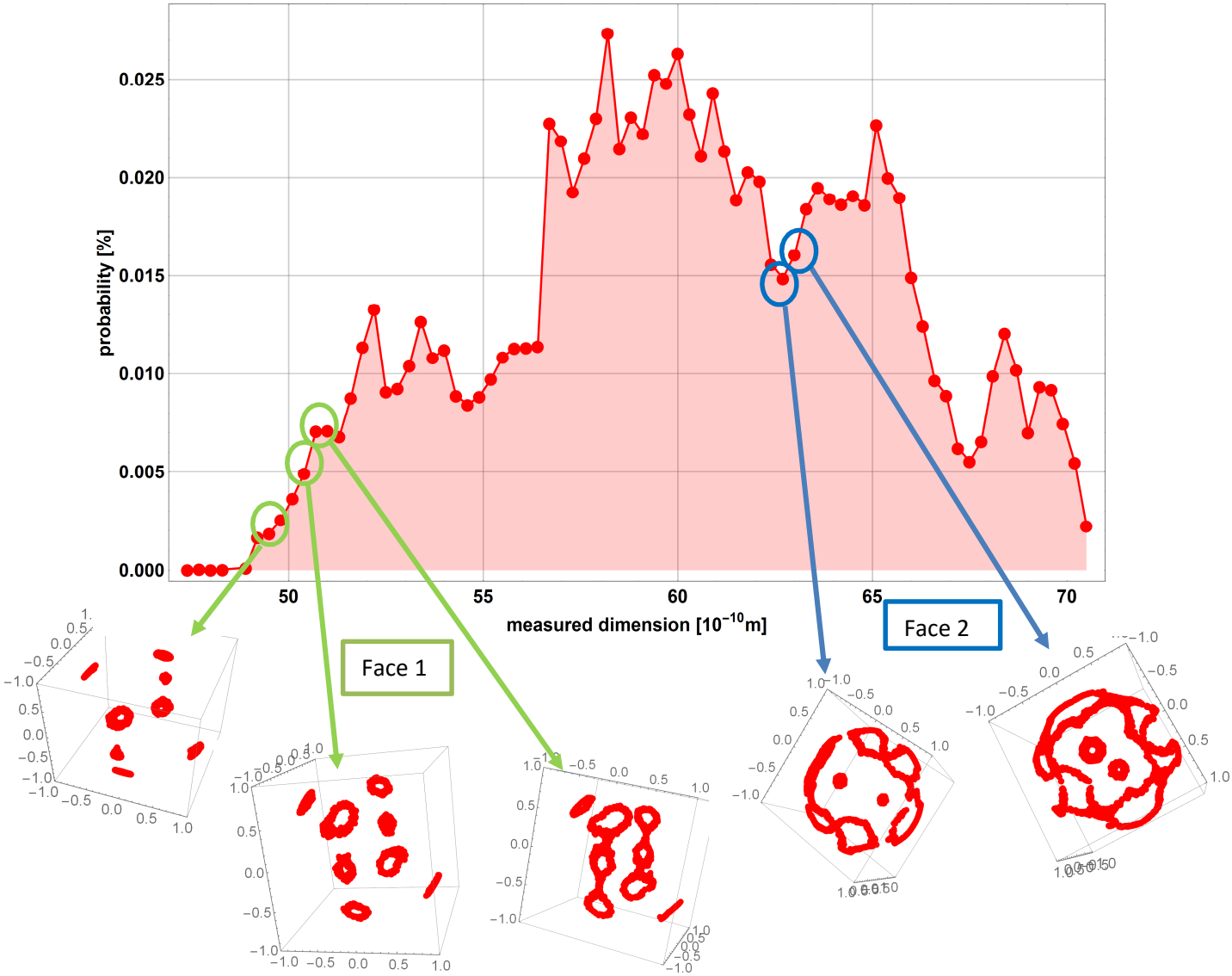

Figure 42: The probability of a distance between two diametrical atoms measured versus the measured dimension. Here we highlighted the corresponding possibilities of finding certain distances and correlated them with the directions the cylinder was stuck through by the red dots in the small boxes.

By tracking the positions at which the measuring bar was stuck through, additional information can be gained. For instance, the information gained allows to differentiate singular facets (of which 2 are shown in Fig. 42) and build a convex set out of this data, which then could be used to calculate and even fit the WAXS pattern [50]. Now, it should be possible to separate the broadening present in the peaks into size

effects and other parameters, such as strain, stacking faults, interstitials etc, thus using the information from ASAXS to evaluate the WAXS portion of the scattering. If the scattering contrast is big enough, one can even try to differentiate between core and shell by a cut-off criterion for the occupancy value for the linear evaluation. First promising hints that this is possible with our system, which exhibits a difference of contrast of 17% between core and shell for theoretical values, are still being worked on. Therefore, both techniques would be needed to gain a clear and full understanding of the crystalline and chemical structure of the sample und further the development of colloidal nanocrystals in the future.

An important side note to the whole analysis presents the possibility to decompose the three parts of the anomalous scattering in *eq. 41*. Obtaining data through increased measurement time that can be split this way, could make the data analysis a lot easier regarding the chemical profile of the NCs. Hence we highly advocate to estimate the needed time of measurement, at a given flux, necessary to perform such a decomposition successfully, if the samples allow it. [22]

Citations

[1] Kovalenko MV, Manna L, Cabot A, et al.” Prospects of nanoscience with nanocrystals”. ACS Nano. 2015; 9(2):1012-57.

[2] CHAPPY - 2007, SN - 978-3-540-68751-1T2 - “Nanocrystals: Synthesis, Properties and Applications”

[3] Reiss P, Protière M, Li L. “Core/Shell semiconductor nanocrystals.” *Small.* 2009; 5(2):154-68.

[4] Lechner RT, Fritz-Popovski G, Yarema M, et al.” Crystal Phase Transitions in the Shell of PbS/CdS Core/Shell Nanocrystals Influences Photoluminescence Intensity.” *Chem Mater.* 2014; 26(20):5914-5922.

[5] Chen O, Zhao J, Chauhan VP, et al. „Compact high-quality CdSe-CdS core-shell nanocrystals with narrow emission linewidths and suppressed blinking”. *Nat Mater.* 2013;12 (5):445-51.

[6] Zineb Saghi, Annu. *Rev. Mater. Re*s. 2012; 42:13.1–13.21

[7] Scardi P, Leoni M. “Whole powder pattern modelling”. *Acta Crystallogr, A, Found Crystallogr*. 2002; 58(Pt 2):190-200.

[8] Als-Nielsen J, McMorrow D. “Elements of Modern X-ray Physics.” Wiley; 2011.

[9] Anton Paar, SAXS Guide, Version 2

[10] Born, Max (1926). "Quantenmechanik der Stossvorgänge". *Zeitschrift für Physik* ***38***

[11] Glatter O, Kratky O. Small Angle X-ray Scattering. London; Academic Press, 1982.;

[12] Warren BE. X-ray Diffraction. Courier Corporation; 1969.

[13] D. Balzar*, Journal of Research of the National Institute of Standards and Technology*; v. 98(3; May-Jun 1993; p. 321-353

[14] T. Ungár, Á. Révész and A. Borbély, “Dislocations and Grain Size in Electrodeposited Nanocrystalline Ni Determined by the Modified Williamson–Hall and Warren–Averbach Procedures”, *J. Appl. Cryst.* (1998). 31, 554-558

[15] H. Blank, P. Delavignette, R. Gevers and S. Amelinckx,” Fault Structures in Wurtzite” *PSS Volume* 7, Issue 3, pages 747–764, 1964

[16] Jan Skov Pedersen, “Analysis of Small-Angle Scattering Data from Colloids and Polymer Solutions: Modeling and Least-squares Fitting” (1997). *Adv. Colloid Interface Sc*i., 70, 171-210.

[17] E. Urena-Benavides, “Static light scattering of triaxial nanoparticle suspensions in the Rayleigh-Gans-Debye regime: application to cellulose nanocrystals” *RSC Adv*., 2012,2, 1096-1105

[18] Guinier A. X-ray Diffraction in Crystals, Imperfect Crystals, and Amorphous Bodies. Courier Corporation; 1994.

[19] Tipler PA, Mosca G. Physik, für Wissenschaftler und Ingenieure. Springer Spektrum; 2014.

[20] M. Sztucki, E. Di Cola, and T. Narayanan, "Anomalous small-angle X-ray scattering from charged soft matter" *Eur. Phys. J. Special To*pics, 208, 319–331 (2012)

[21] G.J. Goerigk," The Solution of the Eigenvector Problem in Synchrotron Radiation Based Anomalous Small-Angle X-Ray Scattering" *Advances in linear algebra & matrix the*ory 3(4), 59-68 (2013)

[22] G. Goerigk, "The Impact of the Turing Number on Quantitative ASAXS Measurements of Ternary Alloys," JOM, Vol. 65, No. 1, 2013, pp. 44-53.

[23] D. I. Svergun," Mathematical methods in small-angle scattering data analysis" *J. Appl. Cryst*. (1991), 24, 485-492

[24] Petoukhov, M.V., Franke, D., Shkumatov, A.V., Tria, G., Kikhney, A.G., Gajda, M., Gorba, C., Mertens, H.D.T., Konarev, P.V. and Svergun, D.I. (2012)," New developments in the ATSAS program package for small-angle scattering data analysis" *J. Appl. Cryst.* 45, 342-350

[25] D. Marquardt, "An Algorithm for Least-Squares Estimation of Nonlinear Parameters" *Journal on Applied Mathematics 11 (2): 431–441(1963)*

[26] M. Frank and P. Wolfe, "An algorithm for quadratic programming"*Naval Research Logistics Quarterly* 3: 95(1956)

[27] Press WH. Numerical Recipes 3rd Edition, The Art of Scientific Computing. Cambridge University Press; 2007.

[28] H. Egger," Nonlinear regularization methods for ill-posed problems"*, Inverse Proble*ms, 25, (2009), 115014 (19pp)

[29] Tikhonov, A. N., & Arsenin, V. I. (1977). *Solutions of ill-posed problems*. Vh Winston.

[30] Qinian Jin, *Numerische Mathematik*, 04.2010, Volume 115, Issue 2, pp 229-259

[31] D. I. Svergun, „Restoring low resolution structure of biological macromolecules from solution scattering using simulated annealing. "(1999) *Biophys J.* 2879-2886

[32] M. Burian, G. Fritz-Popovski, M. He, M. V. Kovalenko, O. Paris and R. T. Lechner," Considerations on the model-free shape retrieval of inorganic nanocrystals from small-angle scattering data" *J. Appl. Cryst.* (2015). 48, 857-868

[33] J. Brunner-Popela & O.Glatter," Small-Angle Scattering of Interacting Particles. I. Basic Principles of a Global Evaluation Technique" *J. Appl. Cryst*. (1997) **30**, 431-442/

[34] Brian R. Pauw*,"* Everything SAXS: small-angle scattering pattern collection and correction*" J. Phys.: Condens. Matter* 25 (2013) 383201 (24pp)

[35] W. H. Beattie and R. M. Tisinger, "Light-Scattering Functions and Particle-Scattering Factors for Ellipsoids of Revolution" *Journal of the Optical Society of America* (1969) vol. 59 pp. 818

[36] Gong K, Kelley DF. "A predictive model of shell morphology in CdSe/CdS core/shell quantum dots*." J Chem Phys*. 2014;141(19):194704.

[37] Foster T. "Universal analytical scattering form factor for shell-, core-shell, or homogeneous particles with continuously variable density profile shape." *J Phys Chem B*. 2011;115(34):10207-17.

[38] O. Glatter," Convolution square root of band-limited symmetrical functions and its application to small-angle scattering data" *J. Appl. Cryst.* (1981). **14**, 101-108

[39] http://www.lookingatnothing.com/wp-content/uploads/2010/12/Guinier_short.pdf

[40] D. Franke, D. I. Svergun, „DAMMIF, a program for rapid ab-initio shape determination in small-angle scattering"*J Appl Cryst*. 42, 342-346. (2009)

[41] P. Klimanek, "X-ray diffraction line broadening due to dislocations in non-cubic materials. I. General considerations and the case of elastic isotropy applied to hexagonal crystals"*J. Appl. Cryst.* (1988). 21, 59-66

[42] R.L. Rothman, J.B. Cohen,"X-Ray Study Of Fulting in BCC Metals and Alloys" *J. Appl. Physics,*(1971), 42 (3), 979-979

[43] C. M. Teodorescu, J.M. Esteva," An approximation of the Voigt I profile for the fitting of experimental X-ray absorption data" *Nuclear Instruments and Methods in Physics Research* A 345 (1994) 141-147

[44] J.I. Langford," A rapid method for analysing the breadths of diffraction and spectral lines using the Voigt function" *J. Appl. Cryst.* (1978). 11, 10-14

[45] Xiaogang Peng, Michael C. Schlamp , Andreas V. Kadavanich , and A. P. Alivisatos , "Epitaxial Growth of Highly Luminescent CdSe/CdS Core/Shell Nanocrystals with Photostability and Electronic Accessibility"*J. Am. Chem. Soc*. 1997, 119, 7019-7029

[46] A. Gosh, S. Paul, R. Satyabrata, "Structural phase transformation from wurtzite to zinc-blende in uncapped CdS nanoparticles"*Solid State Communications* 154 (2013) 25–29

[47] A. *D. McNaught and A. Wilkinson (1997). IUPAC. Compendium of Chemical Terminology (2nd ed.). Oxford: Blackwell Scientific Publications. ISBN 0-9678550-9-8* [50] R. Riedel, Ceramics Science and Technology, Wiley (2011)

[48] A. W. Ruff Jr., L. K. Ives," The Stacking-Fault Energy in α -Silver-Tin", Canadian Journal of Physics, 1967, Vol. 45, No. 2: pp. 787-795

[49] L. Balogh, G. Tichy and T. Ungár," Twinning on pyramidal planes in hexagonal close packed crystals determined along with other defects by X-ray line profile analysis" *J. Appl. Cryst*. (2009). 42, 580–591

[50] A. Leonardi, M. Leoni, S. Siboni and P. Scardi," Common volume functions and diffraction line profiles of polyhedral domains", *J. Appl. Cryst.* (2012). 45, 1162-1172

[51] Vogel CR. Computational Methods for Inverse Problems. SIAM; 2002.